Society for Science and Education
United Kingdom

ISSN: 2055 - 1266
Volume 2 No 6
December 2015

JOURNAL OF BIOMEDICAL ENGINEERING AND MEDICAL IMAGING

TABLE OF CONTENTS

EDITORIAL ADVISORY BOARD

DISCLAIMER

SOCIETY FOR SCIENCE AND EDUCATION
UNITED KINGDOM

JBEMi JOURNAL OF BIOMEDICAL ENGINEERING AND MEDICAL IMAGING

ISSN: 2055-1266
VOLUME 2 ISSUE 6

Preliminary Detection and Analysis of Lung Cancer on CT images using MATLAB: A Cost-effective Alternative

[1]Md. Daud Hossain Khan, [2]Mansur Ahmed and [3]Christian Bach
Department of Biomedical Engineering, University of Bridgeport, USA
[1] daud.h.khan@gmail.com; [2]maahmed@my.bridgeport.edu; [3]cbach@bridgeport.edu

ABSTRACT

Cancer is the second leading cause of death worldwide. Lung cancer possesses the highest mortality, with non-small cell lung cancer (NSCLC) being its most prevalent subtype of lung cancer. Despite gradual reduction in incidence, approximately 585720 new cancer patients were diagnosed in 2014, with majority from low-and-middle income countries (LMICs). Limited availability of diagnostic equipment, poorly trained medical staff, late revelation of symptoms and classification of the exact lung cancer subtype and overall poor patient access to medical providers result in late or terminal stage diagnosis and delay of treatment. Therefore, the need for an economic, simple, fast computed image-processing system to aid decisions regarding staging and resection, especially for LMICs is clearly imminent. In this study, we developed a preliminary program using MATLAB that accurately detects cancer cells in CT images of lungs of affected patients, measures area of region of interest (ROI) or tumor mass and helps determine nodal spread. A preset value for nodal spread was used, which can be altered accordingly.

Keywords: Lung cancer, CT, MATLAB, Region-of-interest (ROI), area

1 Introduction

According to global reports, cancer is one of the most dominant causes of death worldwide, second only to cardiovascular disease.[1] Of the entire global cancer burden, majority of the incidences occur in low-and-middle-income countries.[2] Though there has been a gradual reduction in cancer incidence in the United States of America over the past decade, studies reveal that approximately 585720 new cancer patients were diagnosed in 2014.[3] Lung cancer will be responsible for 158040 total deaths in the United States alone by the end of 2015.[4] Lung cancer continues to be both the most dominant cause of incidence and death due to cancer, with non-small cell lung cancer (NSCLC) being the most prevalent subtype.[1, 2, 5] For quick, proper screening and diagnosis, the availability of radiotherapy or teletherapy centers equipped with efficient diagnostic or imaging equipment is absolutely necessary. Diagnostic procedures include regular imaging techniques such as X-rays, computed tomography (CT) and positron emission tomography (PET) scan.[6] Recent advancements in technology, both hardware and software, have allowed accurate detection, including precise measurement of tumorous masses inside the thoracic cavity. [7-9] However, there are drawbacks. Availability of advanced, diagnostic equipment for accurate detection of lung cancer, such as PET, Magnetic resonance imaging (MRI),

DOI: 10.14738/jbemi.26.1628
Publication Date: 16th November 2015
URL: http://dx.doi.org/10.14738/jbemi. 26.1628

fluorodeoxyglucose PET (FDG-PET), helical CT or 3D-CT are limited, due to the overbearing expenses associated with both purchase and maintenance of such equipment, especially in case of limited-income regions.[8, 10-15] Modern computer assisted diagnosis (CAD) systems, though significantly improve the efficiency of these machines, add to the expenses.[9, 15] Along with the complexity involved in staging and late revelation of the symptoms, patients are often diagnosed at late or advanced stages of the disease.[16, 17] This is more so in the case of low-and-middle-income countries (LMICs). Recent meta-analysis reveals that only 4 of the listed 139 LMICs, as according to the World Bank, have the requisite number of teletherapy centers and 39.5% do not possess a single radiotherapy center.[18] The median patient access to radiotherapy centers in the remaining 80 LMICs is only a deplorable 36.7% and projections indicate that by 2020, the patient demand will exceed the facilities at these LMICs by several folds.[18] African nations have the least number of active radiotherapy centers (60% in Egypt an South Africa alone) while almost negligible data is available regarding Eastern European nations.[19] The situation is made even worse by the fact that most of these centers in LMICs do not have properly trained personnel; a study in Ethiopia showed that 81% of all the healthcare providers had basic medical training and 44% lacked access to any form of diagnostic imaging equipment.[20] Therefore the need for a simple, fast and cost-effective computed image processing system enabling detection of cancer cells from PET/ CT or MRI scans is clearly imminent. MATLAB, a commonly used image-processing and graphics-interface program in academia and industry,[21, 22] can pose as an alternate and affordable means of diagnosis. In this independent, graduate study, we aim to develop a fast, reliable and cost-effective program using MATLAB, which would enable detection of cancerous or tumorous lesions in CT images of the lungs of affected patients. In addition, the program would be able to determine the area of any specific labelled region of interest (ROI) or tumor mass, approximate nodal class, thus, facilitating quick and calculated treatment decisions and diminishing the requirement of more advanced diagnostic equipment.

2 Method

The images used for testing the MATLAB program were obtained from “The Cancer Imaging Archive” (TCIA) portal, a joint project of the National Cancer Institute (NCI) and Washington University serving as a public, open-access image database of advanced medical images of several forms of cancer.[23] Since NSCLC is the most prevalent sub-type of lung cancer,[5] 50 thoracic CT images of NSCLC patients were randomly selected, irrespective of the stages of the disease and set in a directory. The program reads each of this images automatically and are subjected to 4 basic types of modifications; filtering, conversion, edge detection and labelling.[22, 24] A detailed schematic is illustrated below in Figure 1.

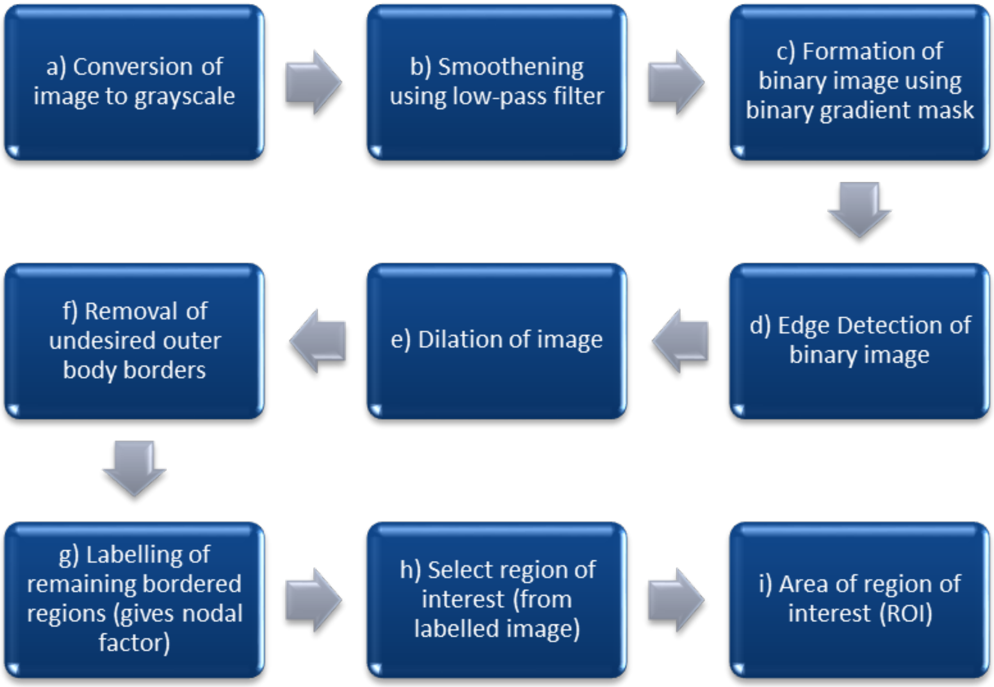

Figure 1: Schematic of program

Conventional image pre-processing techniques of conversion to grayscale, followed by smoothening of image using a customized low-pass filter which is defined by the following equation –

$$LPF\ (x,y) = \begin{cases} 1\ if\ \sqrt{X^2 + Y^2} < CF \\ 0\ if\ \sqrt{X^2 + Y^2} > CF \end{cases} \quad [25]$$

Where where (x, y), is the size of the image and cf is the cut-off value for the low pass filter. After this, thresholding and segmentation techniques were performed respectively.[24] The “smoothened” image was converted to a “black-and-white” image in order to improve contrast.[24] A sobel operator using a fudge factor of 0.8 was used for edge detection of the latter image and then tuned to obtain a binary mask that contains the new segmented image.[26] Sobel operator is shown as follows –

$$\nabla f\ (x,y) = [G_x\ \ G_y]^r = \begin{bmatrix} \frac{\delta f}{\delta x} & \frac{\delta f}{\delta x} \end{bmatrix} \quad [27]$$

$$mag(\nabla f) = \left|\nabla f_{(2)}\right| = [G_x\ \ G_y]^{1/2} \quad [27]$$

$$\emptyset\ (x,y) = arctan\left({}^{G_x}/_{G_y}\right) \quad [27]$$

The resultant edges in the image were then dilated, removed of undesired borders as much as possible and subsequently labelled.[26, 28, 29] Selection of any labelled ROI will yield area of that particular region. The “N” value or lymph node involvement, as according to the TNM staging of lung cancer,[17] was determined as a function of the number of labelled centroid objects. For example, if the number of labelled objects was less than 50, “N” is considered to be “0”, and if less than 150, the value of “N” is “1”. Distant metastasis and metastatic lymph node involvement cannot be determined since the images used are confined to the thoracic cavity. Therefore the nodal value is limited to “0-2”. Being a completely independent study, the co-authors were responsible for all the finances.

3 Results and Discussion

The program was successfully able to mark and label cancerous lesions or tumor masses in the CT images of the NSCLC patients (Fig. 2), indicate lymph node involvement and determine the cross-sectional area of any given or labelled lesion or tumor mass (ROI). The values of area obtained are all scalar values. These are the summation of the total number of pixels present in the particular ROI. Using the dimensions of the actual CT slices, the exact area of any tumor mass can be easily calculated, thus, facilitating selection of “T” value and type of resection. Figure 2(a) illustrates the step-wise image process modification conducted on a particular CT image of a NSCLC patient. Figure 2(b) illustrates the selection of ROI and cross-sectional area determination.

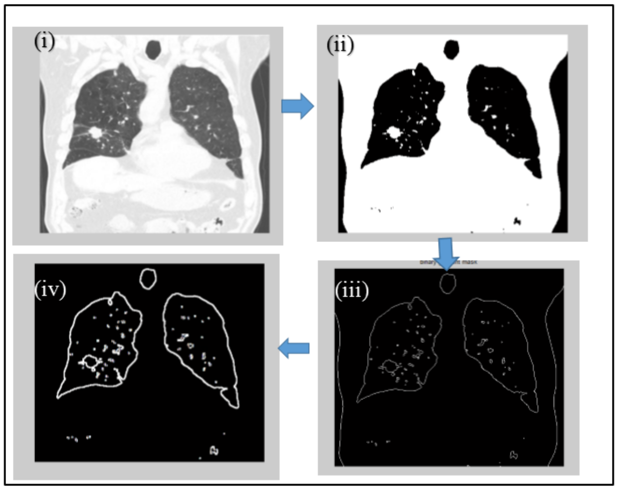

Figure 2(a): (i) Formation of filtered grayscale image; (ii) Conversion from grayscale to black-and-white binary image; (iii) Detection of borders or edges present in binary image; (iv) Dilation and labelling of the detected edges

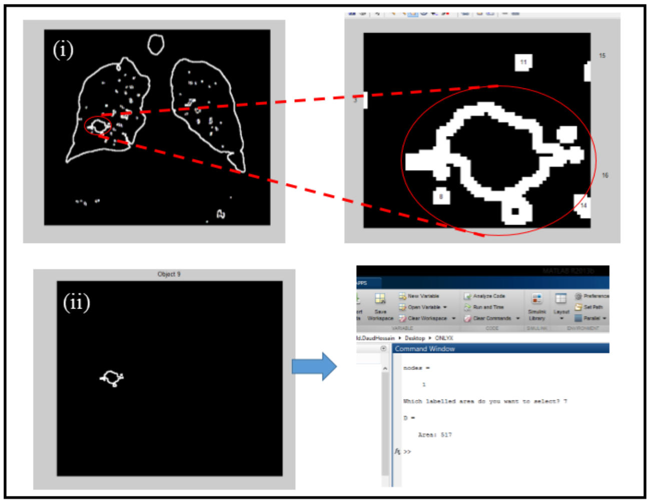

```
nodes =

     1

Which labelled area do you want to select? 7

D =

    Area: 517

>>
```

Figure 2(b): (i) Magnification of labelled ROI ‘7’; (ii) Selection of ROI labelled ‘7’ and window showing cross-sectional area of ROI ‘7’ and nodal-spread value

As mentioned earlier, an assumed criteria for lymph node involvement was used, using the principle that the degree of lymph node spread or involvement is directly proportional to the number of objects detected and labelled in the image. Since the values were assumed, they need rectification from licensed practitioners for validation. The values of cross-sectional areas of the respective ROIs obtained are scalar values. These are the summation of the total number of pixels present in the particular ROI. Using the dimensions of the actual CT slices, the exact cross-sectional area, as well as the volume, of any tumor mass detected in an image can be easily calculated. Summation of the volume of a particular tumor mass from consecutive slices will yield the actual volume of the original tumor mass, thus, facilitating an accurate and cost-effective determination of "T" since this program can be easily implemented in regular low-cost computers, making its clinical availability far superior than the current standards. Another advantage is that the program has the capability to process on all the images in succession, which the user has set in the library. One particular drawback is that this method will not be able to determine the subtype of lung cancer since histological examinations are required for that purpose.

4 Conclusion

Despite a few initial setbacks, the program is highly efficient in detecting tumorous lesions in CT images of lung cancer (NSCLC) patients and determining the cross-sectional areas of any particular lesion or tumor mass. It is adept in determining nodal spread within the thoracic cavity and, with a slight improvement, will be able to determine the volume of any tumor mass accurately. Only a facility with access to CT and a moderate configuration desktop computer is required to run the analysis. The usage is relatively straightforward and does not require highly-trained personnel, thus making it an ideal, cost-effective diagnostic alternative for LMICs. Further modifications are currently being made to incorporate histological data into program and automatically select images or CT slices of interest, though this will inevitably increase operating costs.

REFERENCES

[1] Jemal, A., et al., *Global cancer statistics.* CA: a cancer journal for clinicians, 2011. 61(2): p. 69-90.

[2] Ferlay, J., et al., *Cancer incidence and mortality worldwide: sources, methods and major patterns in GLOBOCAN 2012.* International Journal of Cancer, 2015. 136(5): p. E359-E386.

[3] Siegel, R., et al., *Cancer statistics, 2014.* CA: a cancer journal for clinicians, 2014. 64(1): p. 9-29.

[4] Siegel, R.L., K.D. Miller, and A. Jemal, *Cancer statistics, 2015.* CA: a cancer journal for clinicians, 2015. 65(1): p. 5-29.

[5] Ettinger, D.S., et al., *Non–small cell lung cancer.* Journal of the National Comprehensive Cancer Network, 2012. 10(10): p. 1236-1271.

[6] Smith, R.A., et al., *American Cancer Society guidelines for the early detection of cancer.* CA: a cancer journal for clinicians, 2002. 52(1): p. 8-22.

[7] Cerfolio, R.J., et al., *The accuracy of integrated PET-CT compared with dedicated pet alone for the staging of patients with nonsmall cell lung cancer.* The Annals of thoracic surgery, 2004. 78(3): p. 1017-1023.

[8] Mahadevia, P.J., et al., *Lung cancer screening with helical computed tomography in older adult smokers: a decision and cost-effectiveness analysis.* Jama, 2003. 289(3): p. 313-322.

[9] Sprindzuk, M.V., et al., *Lung cancer differential diagnosis based on the computer assisted radiology: The state of the art.* Polish Journal of Radiology, 2010. 75(1): p. 67-80.

[10] Humm, J.L., A. Rosenfeld, and A. Del Guerra, *From PET detectors to PET scanners.* European journal of nuclear medicine and molecular imaging, 2003. 30(11): p. 1574-1597.

[11] Wisnivesky, J.P., et al., *The cost-effectiveness of low-dose CT screening for lung cancer: preliminary results of baseline screening.* CHEST Journal, 2003. 124(2): p. 614-621.

[12] Yen, T.-C., et al., *Defining the priority of using 18F-FDG PET for recurrent cervical cancer.* Journal of Nuclear Medicine, 2004. 45(10): p. 1632-1639.

[13] Anderson, B.O., et al., *Breast Cancer in Limited-Resource Countries: An Overview of the Breast Health Global Initiative 2005 Guidelines.* The breast journal, 2006. 12(s1): p. S3-S15.

[14] Shyyan, R., et al., *Breast Cancer in Limited-Resource Countries: Diagnosis and Pathology.* The breast journal, 2006. 12(s1): p. S27-S37.

[15] Keppler, J.S. and P.S. Conti, *A cost analysis of positron emission tomography.* American Journal of Roentgenology, 2001. 177(1): p. 31-40.

[16] Corner, J., et al., *Is late diagnosis of lung cancer inevitable? Interview study of patients' recollections of symptoms before diagnosis.* Thorax, 2005. 60(4): p. 314-319.

[17] Rami-Porta, R., J.J. Crowley, and P. Goldstraw, *Review the revised TNM staging system for lung cancer.* Ann Thorac Cardiovasc Surg, 2009. 15(1): p. 5.

[18] Datta, N.R., M. Samiei, and S. Bodis, *Radiation therapy infrastructure and human resources in low-and middle-income countries: present status and projections for 2020.* International Journal of Radiation Oncology* Biology* Physics, 2014. 89(3): p. 448-457.

[19] Grover, S., et al., *A systematic review of radiotherapy capacity in low-and middle-income countries.* Frontiers in oncology, 2014. 4.

[20] Levine, A.C., et al., *Understanding Barriers to Emergency Care in Low-Income Countries: View from the Front Line.* Prehospital and Disaster Medicine, 2007. 22(05): p. 467-470.

[21] Goering, R., *Matlab edges closer to electronic design automation world.* Electronic Engineering Times, 2004(1341): p. 4-5.

[22] Guide, M.U.s., *The mathworks.* Inc., Natick, MA, 1998. 5: p. 333.

[23] Clark, K., et al., *The Cancer Imaging Archive (TCIA): maintaining and operating a public information repository.* Journal of digital imaging, 2013. 26(6): p. 1045-1057.

[24] Gonzalez, R.C., R.E. Woods, and S.L. Eddins, *Digital image processing using MATLAB*2004: Pearson Education India.

[25] Mustafa, W.A., H. Yazid, and S. Bin Yaacob. *Illumination correction of retinal images using superimpose low pass and Gaussian filtering*. in *Biomedical Engineering (ICoBE), 2015 2nd International Conference on*. 2015.

[26] Maini, R. and H. Aggarwal, *Study and comparison of various image edge detection techniques.* International journal of image processing (IJIP), 2009. 3(1): p. 1-11.

[27] Wenshuo, G., et al. *An improved Sobel edge detection*. in *Computer Science and Information Technology (ICCSIT), 2010 3rd IEEE International Conference on*. 2010.

[28] Anoraganingrum, D. *Cell segmentation with median filter and mathematical morphology operation*. in *Image Analysis and Processing, 1999. Proceedings. International Conference on*. 1999. IEEE.

[29] Shrivakshan, G. and C. Chandrasekar, *A comparison of various edge detection techniques used in image processing.* IJCSI International Journal of Computer Science Issues, 2012. 9(5): p. 272-276.

SOCIETY FOR SCIENCE AND EDUCATION
UNITED KINGDOM

JBEMI JOURNAL OF BIOMEDICAL ENGINEERING AND MEDICAL IMAGING

ISSN: 2055-1266
VOLUME 2 ISSUE 6

A Hilbert Transform Based Shear Wave Speed Estimation Method for Shear Wave Elasticity Imaging

Mohammed A Hassan[1], Nancy M Salem[1] and Mohamed I El-Adawy[2]
[1]*Dept of Biomedical Engineering, Faculty of Engineering, Helwan University, Egypt*
[2]*Dept of Electronics, Communications, and Computer Engineering, Faculty of Engineering, Helwan University, Egypt*
mohammed.ali@h-eng.helwan.edu.eg, nancy_salem@h-eng.helwan.edu.eg, 98adawy@gmail.com

ABSTRACT

In this paper, a Hilbert transform based method is used to estimate shear wave speed. Shear wave speed can be measured from the lateral propagation of particle displacements or velocities within the tissue, these particle displacements or velocities are generated by simulating radio frequency signals measured from ultrasound probe elements that image the displaced particles generated from a finite-element model (FEM) that simulates the dynamic response of tissues to acoustic radiation forces. The proposed shear wave speed estimation method is based on locating a zero-amplitude crossing in the Hilbert transform of the cross-correlation function between the particle displacement measured at first lateral location greater than the lateral width of shear wave and the displacement measured and subsequent lateral lines under examination at a certain depth. The results obtained from this method is compared to the lateral Time to Peak (TTP) method that finds the instance at which the maximum displacement is detected at each lateral location under examination at a certain depth. The proposed algorithm reveals a reconstruction of materials having shear modulus of 1.43±0.20, 2.92±0.39, 4.09±0.54, 8.13±1.06, 12.11±1.52, 16.16±2.08 kPa on particle displacement signals for 1.33, 2.835, 4, 8, 12, and 16 kPa shear moduli materials respectively and 1.34±0.40, 2.66±0.41, 3.77±0.58, 7.45±1.14, 11.34±1.51, and 14.90±2.08 kPa on particle velocity signals for 1.33, 2.835, 4, 8, 12, and 16 kPa shear moduli materials respectively. Finally, the proposed method is based on locating a zero-amplitude crossing in the Hilbert transform of the cross-correlation function appears to provide more accurate results than Lateral TTP method.

Keywords Shear wave elasticity imaging, acoustic radiation force, finite element method, shear wave speed estimation, lateral Time to Peak, Gaussian fitting

1 Introduction

Ancient Egyptians used tissue palpation as a fundamental medical diagnosis method, this method is used commonly and effectively in diagnosis until now. However, this qualitatively method can only be used for legions that are superficial, large, and that have a big stiffness difference compared to their surrounding tissues. Remote palpation techniques were developed to overcome these drawbacks and provide non-invasive means of estimating the biomechanical attributes of tissues especially the elastic

DOI: 10.14738/jbemi.26.1585
Publication Date: 26th November 2015
URL: http://dx.doi.org/10.14738/jbemi. 26.1585

(Young's) modulus even for deep and small tissues. These remote palpation techniques are called Elastography techniques[1-3].

Many researchers used Elastography techniques and proved that generated elastograms may not just differentiate effectively between benign and malignant lesions, but they are capable of differentiating between subtypes of malignancy[4, 5]. In some cases elastograms are better than conventional diagnostic B-mode ultrasound images[6], diagnosis of atherosclerosis[7], detection and grading of deep vein thrombosis[8], imaging of skin pathologies[9] and evaluation of myocardial stiffness[10]. Elastography methods are categorized according to different criteria such as excitation source, and/or being quantitative, or qualitative methods. Qualitative, i.e., quasi-static, free hand, and acoustic radiation force on-axis Imaging (ARFI) methods, produce displacement or strain images. On the other hand quantitative methods such as fibroscan, supersonic imaging (SSI), and shear wave elasticity imaging (SWEI) methods can be used to measure tissue stiffness (i.e. the elastic (Young's) modulus)[1, 11-13].

In this paper, a simulation model of the dynamic response of soft tissue to a transient acoustic radiation force impulse (ARFI) excitation using a commercially available, diagnostic, ultrasound transducer is introduced. Then a novel method to estimate the shear wave speed is proposed. This paper is organized as follows. Introduction about elastography, SWEI, and shear wave speed estimation methods are presented in shear wave elasticity imaging section. Methodology section demonstrates shear wave generation and imaging in our experiment and the proposed method. Finally, results, discussion, and conclusion sections is give at the end of the paper.

1.1 Shear Wave Elasticity Imaging

1.1.1 Acoustic Radiation Force

Acoustic radiation force (ARF) is a phenomenon associated with acoustic wave's propagation in attenuating media. Attenuation includes both the scattering and absorption of the acoustic wave. As shown by Nyborg[14], under plane wave assumptions and by neglecting scattering where the majority of the attenuation of ultrasound arises from absorption [15], acoustic radiation force (F) can be related to the acoustic absorption (α), speed of sound (c) of the tissue, and the temporal average intensity of the acoustic beam (I) by:

$$F = \frac{2\alpha I}{c} \tag{1}$$

where F *[kg/(s²cm²)]* is in the form of a body force per unit volume, c *[m/s]* is the sound speed, α *[Np/cm]* is the absorption coefficient of the tissue which is frequency dependent phenomenon, and I *[W/cm²]* is the temporal average intensity at that spatial location. This body forces can be induced in the tissue within the geometric shadow of the active aperture of the transducer having a peak value near the focal point.

The geometrical distribution of this force is dependent on the acoustic parameters of the transmitter along with the speed of sound, and the transducer focal configuration, which can be characterized by the f-number (F/#) of the system:

$$F/\# = \frac{z}{a} \quad (2)$$

Where *z* is the acoustic focal length, and *a* is the active aperture width.

1.1.2 Shear Wave Generation

Sarvazyan et al. have proved that a short-duration focused excitation of a commercially available ultrasound transducer can be used to generate acoustic radiation body forces, which induce tissue displacement centered on the focal region. These displacements propagate through the tissue in the form of shear waves perpendicular to the direction of excitation force (i.e. parallel to transducer surface). This wave can be detected, either by optical coherence tomography, magnetic resonance imaging (MRI), or ultrasound imaging techniques and displayed as an image, their speed is then used to estimate the elasticity of the tissue[16].

Shear wave speed velocity is related to tissue stiffness (i.e. shear modulus, and elastic modulus) using the following equations assuming a pure elastic, homogenous medium[17]:

$$\mathrm{cT} = \sqrt{\frac{\mu}{\rho}} \quad (3)$$

$$\mu = \frac{E}{2(1+v)} \quad (4)$$

where $cT[m/s]$ is shear wave speed velocity, $\mu[Pa]$ is the shear modulus, $E[Pa]$ is the elastic modulus, $\rho[kg/m^3]$ is the density, and υ is the Poisson's ratio.

1.1.3 Shear Wave Estimation

Shear wave is monitored outside the region of excitation (ROE) within focal zone[17-19]. Many researchers have quantified tissue stiffness from shear wave speed (SWS) estimation from dynamic displacement data. SWS estimation from the algebraic inversion of the second-order Helmholtz differential equation has been successfully applied to MRI data[20, 21] but with limited success to ultrasound[22-24] due to the noisy nature of ultrasound displacement estimates. Another technique involves estimation of either the spatial or temporal frequency of monochromatic shear waves, given a priori knowledge of its counter-part[25-27]. By assuming a fixed direction of shear wave propagation, and a given arrival time at multiple spatial locations, then SWS can be estimated using linear regression algorithms. This approach is called time-of-flight (TOF) approach, that has been successfully applied to ultrasound tracked shear wave displacement data[28-31].

2 Methodology

Finite element models (FEM) were developed to simulate the effect of the induction of a transient duration (<100 μs) and spatially localized impulsive acoustic radiation body forces in tissue. A FieldII[32] simulation software is used to calculate and calibrate the pressure field generated from a commercially available, diagnostic, ultrasound transducer and to image the induced displacements in the tissue at different spatial location at different times after excitation. The mechanical response of the tissue to ARF body forces is simulated using LS-DYNA3D[33] FEM solver software, and LS-PREPOST[34] program[17, 35].

2.1 FEM Mesh Generation

The FEM model presented in this paper is similar to FEM model described by Palmeri et al .[17] in which, a three dimensional, rectangular, uniform distributed solid mesh was assembled using linear, elastic, and eight nodded brick elements using HyperMesh[36] program. This mesh represents a soft tissue extends to 7.5 mm, 25 mm, and 35 mm in elevation, axial, and lateral directions respectively with node spacing of 0.2 mm. There are 842688 elements and 876681 nodes within the model. The bottom surface of the model opposing the transducer was fully constrained; the top surface (transducer surface) was allowed to move only within the plane perpendicular to axial direction. All other surfaces of the model have full degrees of freedom. This model has a density of 1.060 g/cm3, poisons ratio of 0.499, and an attenuation of 0.7 dB/cm/MHz.

2.2 Pushing Beam Intensity Generation and Calibration

In our experiments, a model of Siemens SONOLINE ElegraTM ultrasound scanner VF10-5 linear array transducer with center frequency of 6.67 MHz was built using FieldII program. The transducer is laterally focused at 20 mm with F/1.3 focal configuration, and focused at 20 mm in elevation with F/3.8 focal configuration. This transducer is used to excite the tissue with a high intensity low duration pushing beam and generate a displacement within tissue. The aperture (using 96 element) was unapodized with longer pulse duration 43 μs (e.g. 300 cycles at 6.67 MHz). The excitation voltage of the transducer elements were calibrated to generate a spatial peak temporal average intensity (Ispta) of 1000 W/cm^2 using FieldII program, Table 1 summarize excitation parameters. The spatial location of maximum intensity is located proximal than focal point due to acoustic attenuation of the tissue. Only nodes that have intensity greater than 1% of its maximum generated intensity value is used to generate ARF to reduce the computational time of the model.

2.3 FEM Implementation and Post-processing

ARF forces is then calculated from Eq. 1 and directed to the axial direction and converted to nodal point loads by concentrating the body force contributions over an element volume. The response of the tissue model to transient acoustic radiation body forces as dynamic displacements was obtained using the commercially available FEM package LS-DYNA3D software. FEM generated displacements are obtained at each pulse repetition time (PRT = 0.1ms) instances for with a total simulation time equals 5 ms using an explicit, time-domain, and integration method.

Single-point quadrature was performed with hourglassing control to avoid element locking and to reduce numerical artefacts[17, 35, 37], in addition to LS-PREPOST program and custom-written MATLAB code. Six types of tissues have been examined in this experiment having a shear moduli of 1.33, 2.835, 4, 8, 12 and 16 kPa in six different implementations.

Figure 1 illustrates shear wave propagation in the central elevation plane at 0.6 ms, 1 ms, and 2.2 ms in 8 kPa shear modulus simulated tissue, as normalized displacement profiles. Normalized displacement profiles are illustrated as gray levels (i.e. the brightest pixels represent the maximum displacement and vise versa.

Figure 2 shows shear wave propagation at different lateral locations located at focal distance distal from the transducer in the central elevation plane of untracked FEM generated displacements of simulated tissue having shear modulus of 1.33 kPa, and 8 kPa.

2.4 Tracking and Displacement calculations

After FEM post-processing and dynamic displacement field data generation. A uniform scattering phantom having a randomly positioned scatterer points of equal echogenicity, the locations of these scatterer point are taken as initial reference undisplaced scatterer positions. A reference RF tracking lines at lateral lines spacing 0.2 mm starting from 0 mm were generated from these initial undispaced scatterer locations, Using FieldII ultrasound field simulation program[32] Table 1 summarize tracking parameters.

At each PRT instance repetition, the initial undispaced scatterers locations were then linearly interpolated from the displacement field vectors at each mesh point to generate displacement field vector displacement of scatterers at this instance. These interpolated displacement field vectors were used to reposition the scatterers. Tracking RF lines were generated at the same lateral locations as reference RF lines[38]. Induced tissue displacements due to ARFs are measured along each RF tracking lines by Loupas' phase shift method on corresponding IQ data[39].

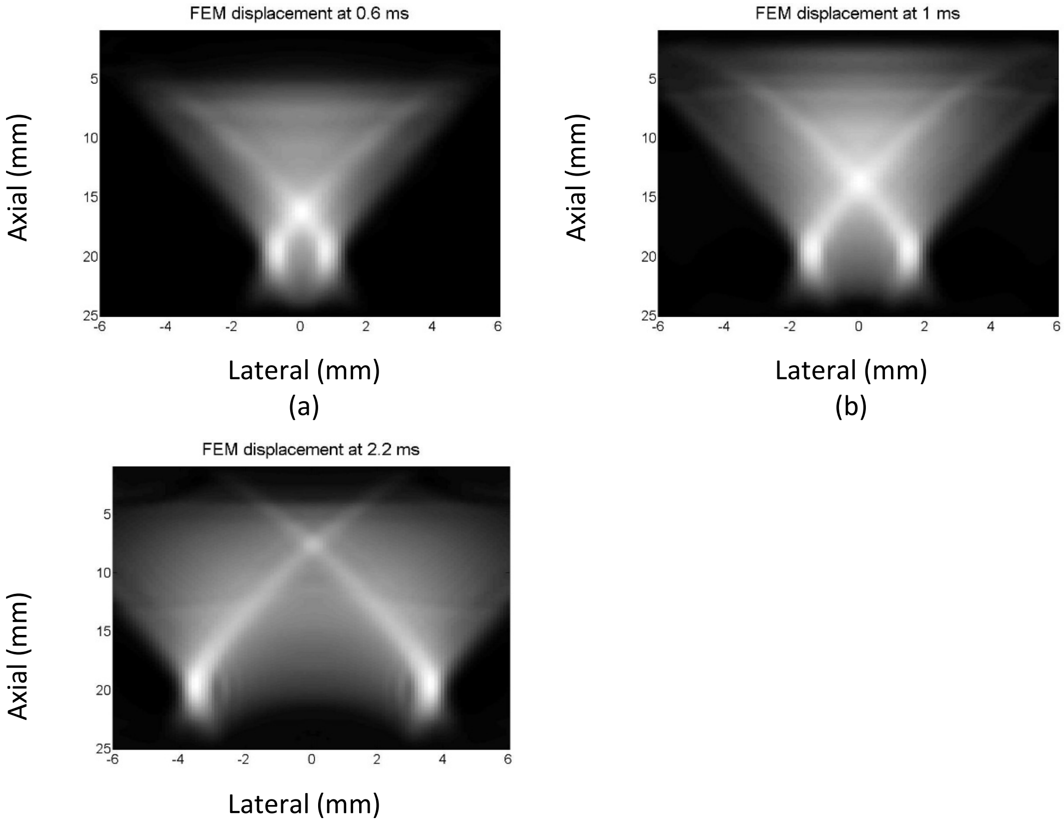

(a)

(b)

(c)

Figure 1. Shear wave location in central elevation plane at A) 0.6 ms, B) 1 ms, and (C) 2.2 ms in 8 kPa shear modulus of untracked FEM generated displacements of simulated tissue. Shear wave location at any instance is displayed as normalized displacement profiles. Normalized displacement profiles is illustrated as gray levels (i.e. the brightest pixels represent the maximum displacement and vise versa.

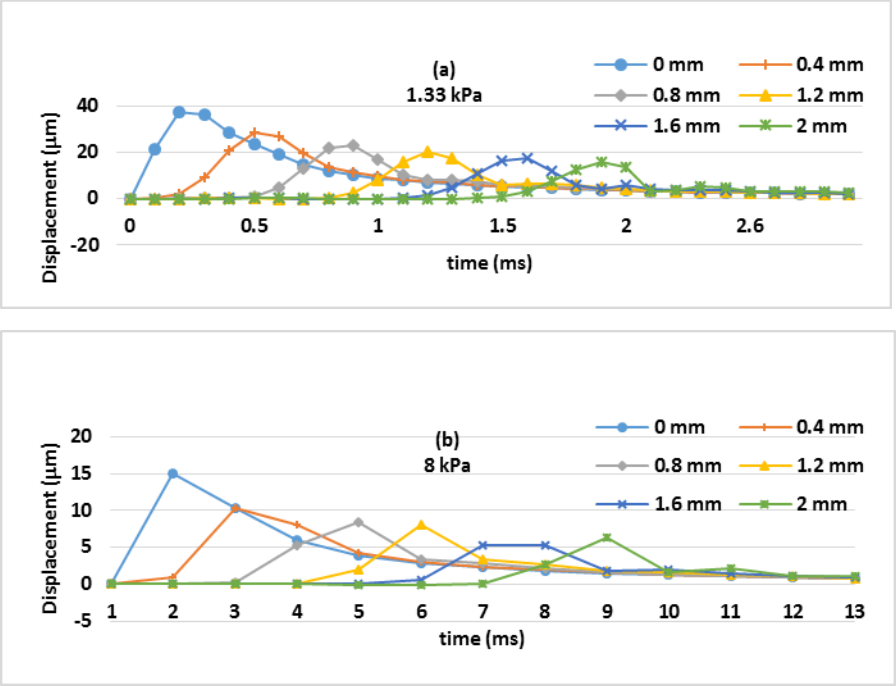

Figure 2. Shear wave propagation at different lateral lines located at focal distance distal from the transducer at central elevation plane of untracked FEM generated displacements of simulated tissue having shear modulus of (A) 1.33 kPa, and (B) 8 kPa.

Table 1: Transducer configurations for the VF10-5 array

Excitation frequency (MHz)	6.7
Excitation duration (µs)	45
Excitation F/#	1.3
Excitation focal depth (mm)	20
Lateral beam spacing (mm)	0.2
Tracking frequency (MHz)	6.7
Tracking transmit F/#	1
Tracking receive F/#	0.5
Elevation focus (mm)	~20
PRF of track lines (kHz)	10
Duration of tracking (ms)	5

2.5 Proposed Shear Wave Speed Estimation Method

The proposed method is based on the property of Hilbert transform in which, The Hilbert transform of a cross-correlation coefficient of a two temporal signals can be used to generate a new time signal, in which zero crossings of the function indicates peak locations in the cross-correlation coefficient function[40]. This peak location can be used a subsample delay estimator between these two temporal signals. This algorithm is applied to both particle displacements or velocities measured within the analyzed region that locates laterally outside the region of excitation (ROE) within the depth of field (DOF) that was defined by $8(F/\#)2\lambda$, where F/# and λ represent the beam f-number, and wavelength of the pushing beam, respectively. The dimensionless excitation beam f-number (F/#) was defined in Eq. 2.

Displacement data from simulated ultrasonic tracking of the FEM generated displacements were rearranged in three-dimensional array in which the axial position, lateral position, and time are they main dimension in order[41]. Then displacements at the focal depth are extracted to finally obtain a 2D array of lateral position, and time.

This method is based on the same assumptions of the TTP algorithm in which tissue is homogenous, wave propagates exclusively in the plane perpendicular to axial direction, and there is no dispersion in the analysed region.

In the proposed method, The Hilbert transform of a cross-correlation coefficient between the axial displacement or velocity reference and track signals. Reference signal is the estimated axial displacement or velocity at the first lateral locations outside ROE i.e. one excitation beam width defined by (F/#)* λ from excitation center and the each of the estimated axial displacement or elocity at the following lateral lines within 2.5mm from excitation center. then zero crossing of the resultant signal indicates propagation delay between reference and track line signals[40].

Zero-crossing can be located between two samples so an interpolation method must be used[42]. Fig. 3a shows an example of reference particle displacement signal at lateral location 0.44 mm and an example of track particle displacement signal at lateral location 0.66 mm measured from 8 KPa phantom. The cross-correlation signal between both signals and the corresponding Hilbert transform are illustrated in Fig3b as Rxy and HRxy respectively, the area around zero-crossing in Fig3B which bounded by two vertical lines is expanded in Fig3c. Although, there are two locations of peat particle displacements in the cross-correlation (Rxy) function in Fig3c Hilbert transform determine the subsample delay more efficient.

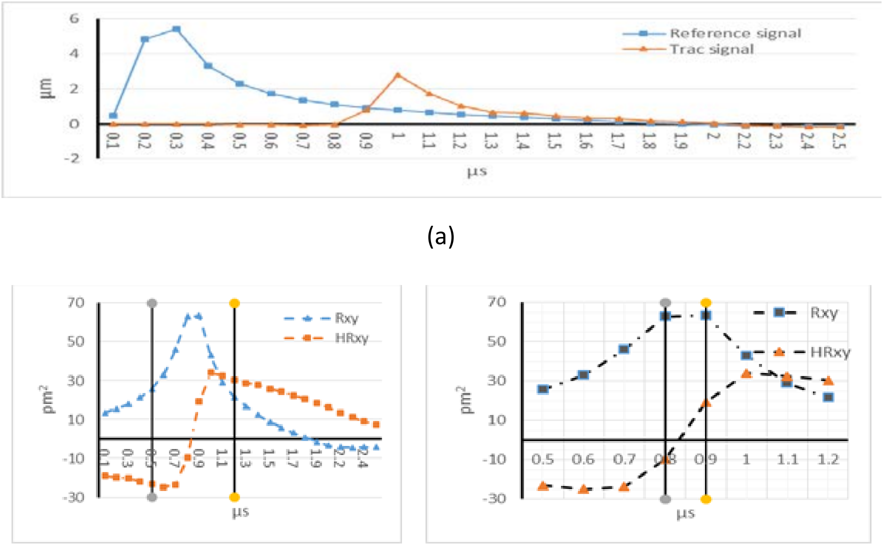

(a)

(b)

(c)

Figure 3. a) An example of reference particle displacement signal at lateral location 0.44 mm and an example of track particle displacement signal at lateral location 0.66 mm measured from 8 KPa phantom. b) The cross-correlation signal between both signals and the corresponding Hilbert transform are illustrated as Rxy and HRxy respectively. c) The area around zero-crossing in (b) which bounded by two vertical lines is expanded.

No modifications are happened to linear regression implementation performed in the Lateral TTP algorithm. The inverse slopes of these regression lines, with goodness-of-fit metrics exceeding a threshold (R2 >0.8, 95% CI <0.2), represent the material’s local shear wave speeds. These specific goodness-of-fit metrics is applied to all of the datasets presented throughout this manuscript. The material’s shear modulus is then estimated using Eq. 3 [31]. In this paper, the proposed algorithm will be tested on both particle displacement and velocity signals. Particle velocity signals are estimated from particle displacement signals by applying first order differentiation.

3 Results and Discussion

Theoretical values of shear wave speeds are 1.153, 1.683, 2, 2.828, 3.46, and 4 m/s propagating in 1.33, 2.835, 4, 8, 12, and 16 kPa shear moduli materials respectively. The proposed algorithm reveals estimation of SWS of same materials as 1.19±0.08, 1.71±0.11, 2.01±0.13, 2.84±0.18, 3.47±0.21, and 4.01±0.25 m/s on particle displacement signals and 1.14±0.15, 1.62±0.12, 1.93±0.15, 2.72±0.21, 3.36±0.22, and 3.85±0.26 m/s on particle velocity signals. The results represented with the mean ± one standard deviation shear wave speed estimates for 20 independent, simulated speckle realizations from FEM displacement data. The corresponding shear modulus estimates are 1.43±0.20, 2.92±0.39, 4.09±0.54, 8.13±1.06, 12.11±1.52, 16.16±2.08 kPa on particle displacement signals for 1.33, 2.835, 4, 8, 12, and 16 kPa shear moduli materials respectively and 1.34±0.40, 2.66±0.41, 3.77±0.58, 7.45±1.14, 11.34±1.51, and 14.90±2.08 kPa on particle velocity signals for 1.33, 2.835, 4, 8, 12, and 16 kPa shear moduli materials respectively. However, TTP method revealed results of 1.30±0.27, 2.66±0.47, 3.86±0.86, 7.39±1.06, 11.22±1.10, and 14.75±3.24 kPa on particle displacement signals for 1.33, 2.835, 4, 8, 12, and 16 kPa shear moduli materials respectively 20 independent, simulated speckle realizations from FEM displacement data[31, 33][31, 33][15, 28]. Table 2, and table 3 summarizes results obtained by the proposed method and the lateral TTP method. It is clear that the proposed algorithm provides better results for 8 kPa shear modulus materials, and less accurate results for 1.33 shear modulus materials. The results obtained for 8 kPa shear modulus simulated materials using lateral TTP algorithm are not available.

The variance increases in stiffer materials because of the fixed pulse repetition time that equals the temporal sampling of displacement dataset. A fixed temporal sampling with increasing the propagation speed of shear waves that is proportional to the square root of shear modulus will cause subsampling of displacement temporal data of shear wave propagation in stiffer materials[31].

Using Hilbert transform as a subsample delay detector to calculate the lateral TTP algorithm can provide better results especially for stiffer materials using both particle displacement and particle velocity signals see table 2 and table 3. The mean value of the reconstructed shear modulus using the proposed method on particle displacement signals is closer to test simulated phantom reference value than results revealed from particle velocity signals except from the more compliant phantom i.e. 1.33 KPa phantom. For the 2.83 KPa phantom, the lateral TTP provides a better results superior to all results revealed from the proposed algorithm.

Table 2: Comparison between shear wave speed estimation results obtained from Lateral TTP and proposed algorithms

Shear modulus (kPa)	Theoretical SWS (m/s)	Estimated SWS (m/s) using		
		Lateral TTP	Proposed method on particle displacement signals	Proposed method on particle velocity signals
1.33	1.15	1.44±0.01	1.19±0.08	1.14±0.15
2.835	1.68	1.66±0.03	1.71±0.11	1.62±0.12
4	2	1.96±0.20	2.01±0.13	1.93±0.15
8	2.82	2.71±0.19	2.84±0.18	2.72±0.21
12	3.46	3.34±0.16	3.47±0.21	3.36±0.22
16	4	3.81±0.48	4.01±0.25	3.85±0.26

Table 3: Comparison between results obtained from Lateral TTP and proposed algorithms

Shear modulus (kPa)	Estimated shear modulus (kPa) using		
	Lateral TTP	Proposed method on particle displacement signals	Proposed method on particle velocity signals
1.33	1.31±0.03	1.43±0.20	1.34±0.40
2.835	2.77±0.08	2.92±0.39	2.66±0.41
4	3.86±0.86	4.09±0.54	3.77±0.58
8	7.39±1.06	8.13±1.06	7.45±1.14
12	11.22±1.10	12.11±1.52	11.34±1.51
16	14.75±3.24	16.16±2.08	14.90±2.08

4 Conclusion

A new method to estimate shear wave speed is proposed. Hilbert transform can be used to provide a more accurate estimation of Lateral TTP value that leads to a more accurate reconstruction of materials shear modulus. Although the proposed algorithm reveales more accurate reconstruction of shear modulus, it revealed less accurate reconstruction of 2.83 kPa materials' shear modulus.

REFERENCES

[1] Wells, P.N.T. And H.-D. Liang, medical ultrasound: imaging of soft tissue strain and elasticity. Journal of the royal society interface, 2011. 8(64): p. 1521-1549.

[2] Sarvazyan, A., Et Al., Elasticity Imaging-An Emerging Branch of Medical Imaging. An Overview. Curr. Med. Imaging Rev, 2011. 7(4): P. 255-282.

[3] Greenleaf, J.F., M. Fatemi, and M. Insana, Selected Methods for Imaging Elastic Properties of Biological Tissues. Annual Review of Biomedical Engineering, 2003. 5(1): P. 57-78.

[4] Garra, B.S., Et Al., Elastography of Breast Lesions: Initial Clinical Results. Radiology, 1997. 202(1): P. 79-86.

[5] Burnside, E.S., Et Al., Differentiating Benign From Malignant Solid Breast Masses with Us Strain Imaging1. Radiology, 2007. 245(2): P. 401-410.

[6] Miyanaga, N., Et Al., Tissue Elasticity Imaging For Diagnosis of Prostate Cancer: A Preliminary Report. International Journal of Urology, 2006. 13(12): P. 1514-1518.

[7] De Korte, C.L., Et Al., Characterization of Plaque Components with Intravascular Ultrasound Elastography in Human Femoral and Coronary Arteries in Vitro. Circulation, 2000. 102(6): P. 617-623.

[8] Emelianov, S., Et Al., Triplex Ultrasound: Elasticity Imaging To Age Deep Venous Thrombosis. Ultrasound in Medicine & Biology, 2002. 28(6): P. 757-767.

[9] Vogt, M. And H. Ermert, Development And Evaluation Of A High-Frequency Ultrasound-Based System For In Vivo Strain Imaging Of The Skin. Ultrasonics, Ferroelectrics and Frequency Control, IEEE Transactions On, 2005. 52(3): P. 375-385.

[10] Kaluzynski, K., Et Al., Strain Rate Imaging Using Two-Dimensional Speckle Tracking. Ultrasonics, Ferroelectrics and Frequency Control, IEE Transactions On, 2001. 48(4): P. 1111-1123.

[11] Treece, G., Et Al., Real-Time Quasi-Static Ultrasound Elastography. Interface Focus, 2011. 1(4): P. 540-552.

[12] Rosenzweig, S., M. Palmeri, And K. Nightingale, Analysis of Rapid Multi-Focal-Zone Arfi Imaging. Ultrasonics, Ferroelectrics, and Frequency Control, IEEE Transactions On, 2015. 62(2): P. 280-289.

[13] Foucher, J., Et Al., Diagnosis of Cirrhosis by Transient Elastography (Fibroscan): A Prospective Study. Gut, 2006. 55(3): P. 403-408.

[14] Nyborg, W., Acoustic Streaming. Physical Acoustics, 1965. 2(Pt B): P. 265.

[15] Anderson, P.G., N.C. Rouze, And M.L. Palmeri, Effect Of Graphite Concentration On Shear-Wave Speed In Gelatin-Based Tissue-Mimicking Phantoms. Ultrasonic Imaging, 2011. 33(2): P. 134-142.

[16] Sarvazyan, A.P., Et Al., Shear Wave Elasticity Imaging: A New Ultrasonic Technology Of Medical Diagnostics. Ultrasound In Medicine & Biology, 1998. 24(9): P. 1419-1435.

[17] Palmeri, M.L., Et Al., A Finite-Element Method Model of Soft Tissue Response to Impulsive Acoustic Radiation Force. Ultrasonics, Ferroelectrics and Frequency Control, IEEE Transactions On, 2005. 52(10): P. 1699-1712.

[18] Nightingale, K., R. Bentley, and G. Trahey, Observations of Tissue Response To Acoustic Radiation Force: Opportunities For Imaging. Ultrasonic Imaging, 2002. 24(3): P. 129-138.

[19] Palmeri, M., Et Al., Evaluating The Feasibility Of Acoustic Radiation Force Impulse Shear Wave Elasticity Imaging Of The Uterine Cervix With An Intracavity Array: A Simulation Study. Ultrasonics, Ferroelectrics and Frequency Control, IEEE Transactions On, 2013. 60(10).

[20] Sinkus, R., Et Al., Viscoelastic Shear Properties Of In Vivo Breast Lesions Measured By Mr Elastography. Magnetic Resonance Imaging, 2005. 23(2): P. 159-165.

[21] Oliphant, T.E., Et Al., Complex‐Valued Stiffness Reconstruction for Magnetic Resonance Elastography by Algebraic Inversion of the Differential Equation. Magnetic Resonance in Medicine, 2001. 45(2): P. 299-310.

[22] Bercoff, J., M. Tanter, and M. Fink, Supersonic Shear Imaging: A New Technique for Soft Tissue Elasticity Mapping. Ultrasonics, Ferroelectrics and Frequency Control, IEEE Transactions On, 2004. 51(4): P. 396-409.

[23] Sandrin, L., Et Al., Shear Modulus Imaging With 2-D Transient Elastography. Ultrasonics, Ferroelectrics and Frequency Control, Ieee Transactions On, 2002. 49(4): P. 426-435.

[24] Nightingale, K., S. Mcaleavey, and G. Trahey, Shear-Wave Generation Using Acoustic Radiation Force: In Vivo and Ex Vivo Results. Ultrasound in Medicine & Biology, 2003. 29(12): P. 1715-1723.

[25] Yin, M., Et Al., Assessment of Hepatic Fibrosis with Magnetic Resonance Elastography. Clinical Gastroenterology and Hepatology, 2007. 5(10): P. 1207-1213. E2.

[26] Chen, S., M. Fatemi, And J.F. Greenleaf, Quantifying Elasticity And Viscosity From Measurement Of Shear Wave Speed Dispersion. The Journal of the Acoustical Society of America, 2004. 115: P. 2781.

[27] Mcaleavey, S.A., M. Menon, And J. Orszulak, Shear-Modulus Estimation By Application Of Spatially-Modulated Impulsive Acoustic Radiation Force. Ultrasonic Imaging, 2007. 29(2): P. 87-104.

[28] Sandrin, L., Et Al., Transient Elastography: A New Noninvasive Method for Assessment of Hepatic Fibrosis. Ultrasound in Medicine & Biology, 2003. 29(12): P. 1705-1713.

[29] Mclaughlin, J. And D. Renzi, Using Level Set Based Inversion Of Arrival Times To Recover Shear Wave Speed In Transient Elastography And Supersonic Imaging. Inverse Problems, 2006. 22(2): P. 707.

[30] Tanter, M., Et Al., Quantitative Assessment Of Breast Lesion Viscoelasticity: Initial Clinical Results Using Supersonic Shear Imaging. Ultrasound in Medicine & Biology, 2008. 34(9): P. 1373-1386.

[31] Palmeri, M.L., Et Al., Quantifying Hepatic Shear Modulus In Vivo Using Acoustic Radiation Force. Ultrasound In Medicine And Biology, 2008. 34(4): P. 546-558.

[32] Jensen, J.A. And N.B. Svendsen, Calculation of Pressure Fields from Arbitrarily Shaped, Apodized, and Excited Ultrasound Transducers. Ultrasonics, Ferroelectrics and Frequency Control, IEEE Transactions On, 1992. 39(2): P. 262-267.

[33] Ls-Dyna3d 3.1. [Computer Program].]. Available From: Http://Www.Lstc.Com.

[34] Ls-Prepost. [Computer Program].]. Available From: Http://Www.Lstc.Com.

[35] Fahey, B.J., Et Al., Acoustic Radiation Force Impulse Imaging of the Abdomen: Demonstration of Feasibility and Utility. Ultrasound in Medicine and Biology, 2005. 31(9): P. 1185-1198.

[36] Altair Hypermesh. [Computer Program]]. Available From: Http://Www.Altairhyperworks.Com.

[37] Hughes, T.J., The Finite Element Method: Linear Static And Dynamic Finite Element Analysis. Prentiss-Hall, Englewood Cliffs, Nj, 1987.

[38] Palmeri, M.L., Et Al., Ultrasonic Tracking Of Acoustic Radiation Force-Induced Displacements In Homogeneous Media. IEEE Transactions on Ultrasonic Ferroelectrics and Frequency Control, 2006. 53(7): P. 1300-1313.

[39] Pinton, G.F., J.J. Dahl, and G.E. Trahey, Rapid Tracking of Small Displacements with Ultrasound. Ultrasonics, Ferroelectrics, and Frequency Control, Ieee Transactions On, 2006. 53(6): P. 1103-1117.

[40] Saad, Z.S., E.A. Deyoe, and K.M. Ropella, Estimation of Fmri Response Delays. Neuroimage, 2003. 18(2): P. 494-504.

[41] Rouze, N.C., Et Al., Parameters Affecting the Resolution and Accuracy of 2-D Quantitative Shear Wave Images. Ultrasonics, Ferroelectrics, and Frequency Control, IEEE Transactions On, 2012. 59(8): P. 1729-1740.

[42] Modamio, V., Et Al., Digital Pulse-Timing Technique for The Neutron Detector Array Neda. Nuclear Instruments and Methods in Physics Research Section A: Accelerators, Spectrometers, Detectors and Associated Equipment, 2015. 775: P. 71-76.

SOCIETY FOR SCIENCE AND EDUCATION
UNITED KINGDOM

JBEMi JOURNAL OF BIOMEDICAL
ENGINEERING AND MEDICAL IMAGING

ISSN: 2055-1266
VOLUME 2 ISSUE 6

Robust Hashing Algorithm for Data Verification

Rushdi A. Hamamreh
Computer Engineering Department, Faculty of Engineering, Al-Quds University
rhamamreh@eng.alquds.edu

ABSTRACT

This paper presents a method for data authentication. Data authentication is the process of being able to verify the source of data. With data authentication, one can distinguish messages originating from the intended sender and an attacker. Data authenticity verification procedure uses cryptographic hash functions as the core algorithm. This algorithm based on linear combination of matrices to find non-invertible matrix, DILH takes advantage about of the compact representation of a set of numbers in a matrix, we design a robust method by employing strong collision resistance and reduces the hashing time.

Key Words— Hash function, Data authentication, Collisions, one-way cryptography, Data integrity DILH, non-invertable matrix.

1 Introduction

Data security is going to be a more and more important issue since various industries use information technology infrastructure for the great benefits. There is a huge number of data in different sectors (Cloud system, Health information system, Internet protocols, Information Retrieval Systems, Transport information network, and etc) . The information is very sensitive, requires high level and long-term preservation, and demands of data sharing. How to effectively ensure the authenticity of documents is a vital technology related to data security, information integrity and the interests of target groups (patients, students, and etc) [18].

Hash functions are important security primitives used for authentication and data integrity. The data integrity as a service based on the principles of security mechanism, that releases the data received are the same as send by an authorized entity using hash functions[1].

Hash functions H are one-way functions with as input a string of arbitrary length of the message m and as output a fixed length string of the hash value v. One-way functions work in one direction, meaning that it is easy to compute the hash value from a given message and hard to compute a message that hashes to a given hash value [1]. Hash algorithm is considered as the foundation algorithm of message security, identity, authentication, and message integrity [2].

The security of these applications depends on the cryptographic strength of the underlying hash function. Therefore some security properties are required to make a hash function suitable for such cryptographic uses: Pre-image resistance: Given a hash value v it should be hard to find any message m

DOI: 10.14738/jbemi.26.1644
Publication Date: 5th December 2015
URL: http://dx.doi.org/10.14738/jbemi. 26.1644

such that $= H(m)$, and a message $m1$ it should be hard to find another message $m2 \neq m1$ such that $H(m1) \neq H(m2)$ and Collision resistance: It should be hard to find different messages $m1, m2$ such that $H(m1) = H(m2)$ [2][8].

A hash collision is a pair of different messages $m1 \neq m2$ having the same hash value $H(m1) = H(m2)$. Therefore pre-image resistance and collision resistance are also known as weak and strong collision resistance, respectively. Since the domain of a hash function is much larger (can even be infinite) than its range, it follows from the pigeonhole principle that many collisions must exist. A brute force attack can find a pre-image for a general hash function with n-bit hashes in approximately 2^n hash operations. Because of the birthday

A brute force approach to generate collisions will succeed in approximately $\mathbf{2^{n/2}}$ hash operations. Any attack that requires less hash operations than the brute force attack is formally considered a break of a crypto graphical hash function[3][10].

2 Hash function properties

Hash functions $H(M)$ are mathematical computations that take in a relatively arbitrary amount of data as input and produce an output of fixed size. The output is always the same when given the same input. The inputs to a hash function are typically called messages *M* , and the outputs are often referred to as message digest v. Hash function H has next security properties:

1. H should accept a block of data of any size as input.
2. H should produce a fixed-length output no matter what the length of the input data is.
3. H should behave like random function while being deterministic and efficiently reproducible. H should accept an input of any length, and outputs a random string of fixed length. H should be deterministic and efficiently reproducible in that whenever the same input is given, H should always produce the same output.
4. Given a message H, it is easy to compute its corresponding digest v; meaning that v can be computed in polynomial time $O(n)$ where n is the length of the input message, this makes hardware and software implementations cheap and practical.
5. Given a message digest v, it is computationally difficult to find M such that $H(M) = v$. This is called the one-way or pre-image resistance property. It simply means that one should not be capable of recovering the original message from its hash value.
6. Given a message $m1$, it is computationally infeasible to find another message $m2 \neq m1$ with $H(M1) = H(M2)$. This is called the weak collision resistance or pre-image resistance property.
7. It is computationally infeasible to find any pair of distinct messages $(m1, m2)$ such that $H(m1) = H(m2)$. This is referred to as the strong collision resistance property[1].

3 Matrix Hash Algorithm

Matrix K is a square matrix, the inverse is written K^{-1}. When K is multiplied by K^{-1} the result is the identity matrix I. Non-square matrices do not have inverses.

Not all square matrices have inverses. K square matrix which has an inverse is called invertible or nonsingular, and a square matrix without an inverse is called non-invertible or singular [12].

$$KK^{-1} = K^{-1}K = I$$

We call I here identity matrix. As we previously mentioned, not all matrices have Inverses but most of them have [12], so here we proposed an algorithm that converts any invertible matrix non-invertible one.

3.1 Hill Cipher

The core of Hill-cipher is matrix manipulations. It is a multi-letter cipher, is a type of monoalphabetic polygraphic substitution cipher. Hill cipher requires inverse of the key matrix while decryption. In fact that not all the matrices have an inverse and, therefore they will not be eligible as key matrices in the Hill cipher scheme [6][9]. Moreover, Hill cipher has several advantages such as disguising letter frequencies of the plaintext (M), its simplicity because of using matrix multiplication and inversion for enciphering and deciphering, its high speed, and high throughput [11].

3.1.1 Hill Cipher (Encryption, Decryption)

To Encrypt Plaintext Block size of m [9], we need key matrix **(**$K_{n\times n}$**)** with entries are between $(0, q - 1)$ included, but the determinant must be relatively prime to p, each entry in the plaintext block is between $(0, q - 1)$, included each block of plaintext is then an n-dimensional vector m .We encrypt vector m simply to produce the cipher text vector $\boldsymbol{c}$ using the following linear algebra equation:

$$c = m \times k \, mod \; N$$

To Decrypt cipher text vector $\boldsymbol{c}$ [9], we need first to find the inverse matrix k^{-1} to k , where that matrix must be invertible . Then can calculate m from the mathematical model

$$m = c \times k^{-1} \, mod \, N$$

In [5][9] they proposed new technique to convert any non-invertible matrix's to invertible ones. As a result, Hill cipher being a efficient algorithm because any encrypted text will decrypted using the key matrix [5][10].

3.1.2 Hill Cipher (Hashing algorithm)

The main point of one-way hash algorithm is that any encrypted text cannot be decrypted [11]. From this point, we need to choose the non-invertible matrix from the hill cipher to use it inside the practical one- way hash algorithm.

$$H(m) = m \times k \, mod \, N$$

$$H(m_i) = v_i$$

Where k is the non-invertible matrix. In [11] author works on an algorithm that generate non-invertible matrix and multiply it by plaintext as column vector with modular value N to generate the hash value V.

4 Proposed Algorithm (DILH)

Data integrity using linear combination for Hash algorithm (DILH) uses non-invertible matrix to produce hash value V. This algorithm selects and generates non-invertible matrixes using linear combination of rows or columns of a matrix to ensure that the hash values are collision-free and one-way properties [1].

In this section, we plot the diagram for our proposed algorithm which showing each step inside it and how it works , It is also showing the mathematical proof of our work. Besides that, we have the DILH algorithm analysis and result and its comparison with other hashing algorithms including SHA-1 ,MD5 [17].

4.1 Programmable Hash algorithm

According to figure 2, the step of DILH algorithm structured as the followings:

Step1 (Input): input M.

Step2 (Padding): Pad (P) , $P(M)$.

Step3 (Splitting): M is split into.q is the number of blocks. blocks $(\mathrm{m}_1 , \mathrm{m}_2 ,.., \mathrm{m}_\mathrm{i})$,each of length $n \times n$ suitable for the hashing block.

Step4 (Key generation): Key matrix generation k_i :

4.1: Generate a random matrix (R) with size $(\mathrm{n}-1, \mathrm{n})$ and value in a interval (0,1).

4.2. Casting (R)

4.3. Introduce a new row in the matrix R so as the size of the resulting matrix k_i is $n \times n$. The added row is obtained by ***linear combination*** of row i and row j of matrix R according to:

$$\boldsymbol{K(N,:) = c_1 \times R(i,:) + c_2 \times R(j,:)}$$

where c_1, c_2 are arbitrary integer constants. This ensure that the inverse of K denoted by K^{-1} does not exist.

Step5 (GenerationV_i): Hash value V_i generation using this formula:

$$\boldsymbol{H_{xi} = m_i \times k_i = v_i}$$

Step6 (Digest): Digest V_i.

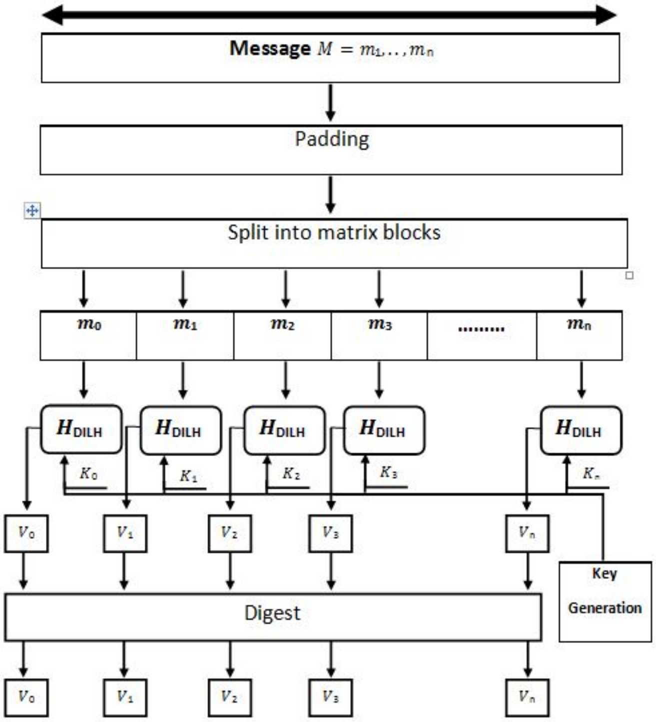

Figure.1 DILH diagram

4.2 Mathematical Model Proof

The first step is to define *linear independence*. Given a set of vectors[12]:

$$v_1, v_2, \dots., v_k$$

we look at their linear combinations:

$$c_1v_1 + c_2v_2 + \dots\dots + c_kv_k$$

Where $c_1, c_2, \dots, c_k$ are arbitrary constant weights. The trivial combination, with all weights $c_i = 0$, obviously produces the zero vector $0v_1 + \cdots + 0v_k = 0$. The question is whether this is the only way to produce zero. If so, the vectors are independent. If any other combination of the vectors gives zero, they are dependent [12].

It is well known that a matrix A is invertible if and only if its rows and columns are linearly independent [12]. This mean that if rows and columns of a matrix are linearly independent then the matrix is invertible, otherwise it's not invertible.

5 Simulation and Results

A different file sizes is randomly selected and is fed into the algorithm to generate different hash Values with three modular values N=64,128,256 to analyze the time delay and to find if there is any collisions.

Table 1: Optimal time in seconds required for the proposed DILH Algorithm with number of collisions found

File size KB	Optimal matrix size n × n			Time/Second			Number of Collisions found		
	mv =64	*mv* =128	*mv* =256	*mv* =64	*mv* =128	*mv* =256	*mv* =64	*mv* =128	*mv* =256
8	11X11	10X10	11X11	6.5678	4.7815	4.9725	0	0	0
16	11X11	11X11	11X11	13.6609	10.0950	10.7546	0	0	0
32	11X11	11X11	11X11	18.7210	21.8399	20.3674	0	0	0
64	11X11	11X11	11X11	37.3445	44.8996	38.6646	0	0	0
128	11X11	11X11	11X11	73.5361	88.1278	80.8281	0	0	0
256	11X11	8X8	12X12	146.6388	177.9706	174.073	0	0	0

From table 1, we can observe that there are no collisions found over all file sizes with its hash values. DILH shows that hash value 968 bit is repeated more than one time compared to other hash values, beside that there is no collisions found over it .So we can consider the hash value 968 bit as a good option to deal with it DILH algorithm.

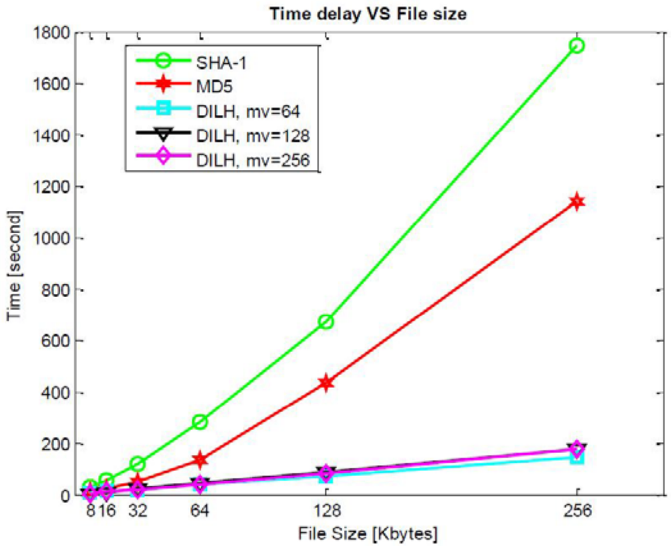

Figure 2: Hash algorithms comparison (SHA-1, MD5, and DILH) in term of time delay versus file size

In this simulation we examine different hash values length started from 2x2 which also equal 32 bits to 12x12 which equal 1152 bits. DILH algorithm find collisions only in 32 bit hash value length.

Fortunately MD5 and other common hash functions have substantially larger key lengths than 64-bits. For MD5 the key length is 128 bits, for SHA-1 the key length is 160 bits, SHA-256 the key length is 256 bits.[17]

The MD5 algorithm breaks a file into 512 bit input blocks. Each block is run through a series of functions to produce a unique128 bit hash value for the file.

Wang,Yu find two 128 byte messages with same MD5 hash value[10].

In SHA-1 Collisions found in 2^{80} operations of reduced version of SHA-1--53 out of 80 rounds[16].

We implement our hash scheme in a Dell vostro 1015 laptop, 2.10GHz 2 core(s), 2GB RAM/ Microsoft windows7/MATLAB 7.9.0 simulator.

6 Analysis and Conclusion

Based on the analysis of the data in Table 1, our algorithm shows its strength in dealing with the collisions. As shown DILH algorithm didn't find any collisions in hash values with different file sizes from

8KB to 1024KB after 3X3 matrix size. DILH shows collisions just in 2X2 with all file sizes, as shown the algorithm find 474 collisions in 2X2 matrix with size 64KB and $N = 128$ but this number of collisions is just 2.921% of overall hash values generated that's where number of hash values generated is 16223 hash values. Also in the same case when $N = 256$ number of collisions is just 0.5178 % where number of hash values generated is 16223. From our analysis when you increase N the number of collisions is decreased in an Inverse relationship.

We check collisions in the new one-way data integrity hash algorithm DILH that based on special kinds of non-invertible metrics. Particularly, DILH shows its strength in dealing with collisions, as shown in table 1 DILH didn't find any collision after 72 bit hash value length. In our experiment $\mathrm{N} = 64, 128,256$.

In our proposed algorithm DILH [2] , the time delay have been tested , DILH shows that the best time for calculating hash value in 8KB is 800bit when $\mathrm{N} = 128$ and 968 bit when $\mathrm{N} = 256$.

REFERENCES

[1] William Stallings. Cryptography and Network Security Principles and Practices, 5th Edition, January 24, 2010.

[2] Rushdi Hamamreh, Mohammed A. Jamoos, Raid Zagha.l DILH: Data Integrity using Linear Combination for Hash Algorithm, ICITeS-Edas-1569740315-18.

[3] Shangping Wang, Yaling Zhang, Youjiao Zou, Jin Sun. A New Hash Algorithm Based on MQ Problem and Polymorphic, International Conference on Information Science and Technology,March 26-28, 2011 Nanjing, Jiangsu, China.

[4] Schneir, Bruce. Applied Cryptography Protocols, Algorithms and Source code in C. s.l. : John Wiley & Sons, 1996. 0471128457.

[5] Songsheng Tang, Fuqiang Liu. A one-time pad encryption algorithm based on one way hash and conventional block cipher, Qingdao, P.R.China, Consumer Electronics, Communications and Networks (CECNet), 2012 2nd International Conference on , 21-23 April 2012 .

[6] Sarat Kumar Patra, Invertible. Involutory and Permutation Matrix Generation Methods for Hill Cipher System, International Conference on Advanced Computer Control, National Institute of Technology Rourkela, Orissa-769008, India.

[7] Artan Berisha, Behar Baxhaku. A Class of Non Invertible Matrices in GF (2) for Practical One Way Hash Algorithm. International Journal of Computer Applications (0975 – 8887), VOL. 54– No. 18, September 2012, China.

[8] ZHOU Tian-shu, LI Jing-song. Development of Data Authenticity Verification System in Regional Health, IEEE International conference ITIME, August 2009.

[9] James H. Burrows. Secure hash standard, federal information processing standards publication (Supersedes FIPS PUB 180 – 1995 May 11).

[10] Wang X Y, Yu H B, Yin Y Q. Efficient collision search attacks on SHA-0,2005, Lecture Notes in Computer Science 3621 1.

[11] Rushdi A. Hamamreh, Mousa Farajallah. Design of a Robust Cryptosystem Algorithm for Non-Invertible Matrices Based on Hill Cipher, International Journal of Computer Science and Network Security; pp 11-16, 2009.

[12] Jianqiu Ji, Jianmin Li, Shuicheng Yan. Min-Max Hash for Jaccard Similarity. 13th International Conference on Data Mining, Dallas, Texas, December 7-10, 2013.

[13] Gilbert strang. Linear Algebra and Its Applications, 4th Edition, May 9, 2011.

[14] Ahmed Y. Mahmoud and Alexander G. Secure Hill Cipher Modifications and Key Exchange Protocol, Chefranov. IEEE International Conference on Automation Quality and Testing Robotics (AQTR), 28-30 May 2010, VOL. 2 .

[15] Danilo Gligoroski, Smile Markovski and Svein J. Knapskog. A Secure Hash Algorithm with only 8 Folded SHA-1 Steps”, IJCSNS International Journal of 194 Computer Science and Network Security, 2006, VOL.6 No.10.

[16] X. Wang, Y. Lisa Yin, H. Yu. Finding Collisions in the Full SHA-1, Crypto 2005, LNCS ,3621 , pp. 17-36, 2005.

[17] X. Wang, H. Yu. How to break MD5 and Other Hash Functions, Advances in EUROCRYPT2005, LNCS 3494, pp. 19–35, 2005.

[18] Jingkuan Song, Yi Yang. Robust Hashing with Local Models for Approximat Similarity Search. IEEE Transaction on Cybernetics VOL. 44, NO. 7, July 2014.

SOCIETY FOR SCIENCE AND EDUCATION
UNITED KINGDOM

JBEMi JOURNAL OF BIOMEDICAL
ENGINEERING AND MEDICAL IMAGING

ISSN: 2055-1266
VOLUME 2 ISSUE 6

Rician Noise Removal and Straightening of Blood Vessel in MR Images

[1]Jayabal Papitha and [2]Damodaran Nedumaran
Central Instrumentation and Service Laboratory, University of Madras, Guindy Campus,
Guindy, Chennai, Tamilnadu, INDIA
[1]papitha_jaya@yahoo.com; [2]dnmaran@gmail.com

ABSTRACT

Purpose: To improve the visualization of severities in blood vessels combined Smoothing and straightening of a blood vessel was attempted for effective diagnosis of tumors and platelet formation in blood vessels.

Method: Fast gradient projection method was used for removing the Rician noise present in MR images. The smoothed image was extracted using the binarization technique and the extracted blood vessels are straightened using a tangent function.

Result: These techniques were tested in a variety of MR images and the results of this study reveal that the proposed method removed the Rician noise without affecting the diagnostic details and compared with existing methods quantitatively, extracted and straightened the blood vessels for making a clear decision about the severity of the disease.

Conclusion: The smoothed, extracted and straightened images are very much useful for the diagnosis of tissue characterization and tumor detection.

Keywords: Rician noise, Fast gradient projection, Extracting, Centerline, Straightening

1 Introduction

Magnetic resonance imaging (MRI) is an outstanding imaging modality but suffers from low contrast and noise during image acquisition and transmission. The noise in magnitude MR images is accurately modeled by a Rician distribution and becomes tough to diagnose accurately for Image analysis and tissue charactrization.

Vessel extraction is employed as a potential tool for automatic clinical diagnosis, treatment planning, computer-integrated surgery, quantification of tissue volume, localization of pathology, and registration using imaging modalities like Magnetic Resonance Imaging (MRI), Computed Tomography (CT), X-ray Angiography (XRA), Magnetic Resonance Angiography (MRA), etc. With the developments in computer technology and imaging technology, the automation of imaging diagnostic has been implemented to handle the volume of data involved in the imaging modalities and to reduce the cost of diagnosis. Blood vessel extraction is the most important automation technique due to its effective and frequent

---

DOI: 10.14738/jbemi.26.1665
Publication Date: 14th December 2015
URL: http://dx.doi.org/10.14738/jbemi. 26.1665

applications, viz., vascular diseases diagnosis, surgery planning, and post-therapeutic monitoring. Various approaches are reported in the in the literature for the extraction of the vessel structures from MR images, which have their own limitations. Some images cannot provide an entire vessel in one slice. In that case, a smooth curved surface can be used to fit into the winding vessel and cut open the volume along the centerline of a vessel instead of using a straight cut plane. This allows bends in a vessel to be straightened, so that the entire length can be visualized in one image. The vessel interior is of great importance for evaluating the degree and distribution of diseases. Visualization techniques re-sample a longitudinal cross-section along the medial axis in one image plane for simultaneous and accurate visualization of diagnostic features. Different strategies have been integrated to achieve different visualization techniques. Most advanced medical workstations are able to semi-automatically find a centerline between two points specified by the user. On the visualization side, some of the aspects of interest are: Variation of seeding structures, Integration length, Type of primitive for an integration-based visualization, Different time steps of the flow, Variation of other visualization parameters. Several vessel visualization techniques have been used in CT images, whereas for magnetic resonance (MR) images the application of these techniques is limited due to the presence of inherent Rician noise. As a result, we implemented the fast gradient projection algorithm for the removal of Rician noise present in MR images and extracted and straightened the blood vessel using binarization and visualization techniques, respectively. MATLAB is used for algorithm development due to its versatility in implementing the complex operations very easily using the built-in signal and image processing toolkits.

The rest of this paper is organized as follows: In Section 2, we discuss the functionality and applications of vessel straightening in various imaging modalities. Section 3 presents the basics of Fast Gradient Projection Method and related algorithms. Section 4 briefly reviews the centerline computation and straightening techniques. The results and the concluding remarks of this study are given in Sections 5 and 6, respectively.

1.1 Related Work

O’Donnel et al. [1] proposed a piecewise polynomial functions connected at knot points for a simple spine model based on cubic B-splines. The tangent of the spine at each knot point was calculated and aligned with the tangent of the succeeding knot point with a minimal rotation in order to construct a discrete frame at each knot point. Then the frames were joined together by interpolation based on the EGC model. Barrett and Carvalho developed a software tool for straightening curved chromosomes [2]. Zhang et al. generated a curved multiplanar reformation (MPR) images for vessel segmentation and tracking for the gradation of the calcified coronary artery plaque [3]. Chuang and Chen developed a straightening tool for a coronary artery that provides slices of the straightened artery at any cross-sectional angle, and more information about the coronary artery and the surrounding tissues [4]. Kanitsar et al. proposed a helical curved planar reformation (CPR) technique to visualize the interior of a vessel and an untangled CPR technique for displaying the unobscured display of a vascular tree that was independent of the viewing direction [5, 6]. Wang analyzed the extraction of the 3D centreline of the vessel of interest through a vessel tracking algorithm and created four longitude vascular volumes at 45º intervals for the visualization of the curved arteries using a multiplanar reformation (MPR) method [7, 8]. Zhang addressed the coronary vessel tracking problem by extracting the vessel centerlines as intensity ridges from CTA images using a ridge traversal algorithm [9]. Wink et al. presented several techniques for the extraction and display of coronary center line for the development of automatic diagnostic cath for the early and accurate detection of coronary artery disease [10]. Saran et al. developed a novel method to remove the Rician noise and RF inhomogeneity in MR images during segmentation using the Goldfeld, Quant, and Trotter (GQT) subtraction method [11]. Lawler demonstrated a combined tool to find the center of the vessel (centerline tools) and vessel-straightening of tortuous curves in coronary arteries [12]. Kanitsar proposed four different segmentation techniques for vessel straightening, viz., projected CPR, stretched CPR, straightened CPR, and helical CPR and three different methods for vessel tree visualization such as multi-path projected CPR, multipath stretched CPR, and untangled CPR with their pros and cons [13]. Kim developed 3-D volume extraction algorithm for segmentation of cerebrovascular structures on brain MRA that provided better results than other traditional methods [14]. Olabarriga et al. developed a Hessian-based filter to analyze the second-order variation in CT image intensity for determining the axis and type of local structure [15]. Zenteno et al. applied a distal-to-proximal technique for the segmentation of tortuous cervical segment in internal carotid artery for the management of complex interacranial aneurysms [16]. Dupej studied the shortfalls of the Straightened Curved Planar Reformation (SCPR) method and improved it by choosing equidistant samples on the vessel center line for calculating the local coordinate system and the square-shaped area (slices) of the volume centered at the center line was calculated, instead of short line segments in the case of SCPR. These slices were stacked to obtain a block of volume data using the maximum intensity projection (MIP) that provides more spatial context for more intuitive orientation in the resulting image [17]. Ropinski integrated a specialized multipath curved planar reformation and multimodal vessel flattening technique for the visualization of multiple data sets for achieving the undistorted diameter of the vessel as well as the positions of the arteries [18]. Rivest-Henault et al. developed a 2D/3D nonrigid registration algorithm based on the global affine transformation and local nonrigid registration methods for the automatic extraction of vessel centerlines of the coronary arteries and aligning with the bi-plane fluoroscopic angiograms [19]. Koocsis et al. developed an algorithm for filamentous particles straightening using a non-uniform cubic spline [20]. Wassermann et al. developed a Diffusion Tensor method to recover the bundles of fibers in the spinal cord and applied the Gaussian framework to recover the most representative fiber, which was used to interpolate and straighten the spinal cord fibers [21]. Angelelli and Hauser demonstrated the straightening and the visualization of tubular flow by aligning the center line of the bounding tubular structure with one axis of the screen defined as vector fields on a Cartesian grid [22]. Mistelbauer et al. proposed Curvicircular Feature Aggregation (CFA), which aggregates the rotated images into a single view by eliminating the rotation around the centerline of the vessel as in the case of the CPR method in order to view the vessels in one image [23]. Lee and Rasch developed an algorithm based on topological and orientation invariant visualization techniques for the visualization of vascular trees [24].

2 Methods

2.1 Fast Gradient Projection Method

Bound constrained optimization problems are solved using Gradient Projection (GP) methods which allow large changes in the data set in each iteration. Linear GP methods are applied in non-linear constrained programming functions. Goldstein [25] and Lewtin & Polyak [26] introduced a GP method for resolving convexly constrained minimization problems as an extension of the steepest descent or a Cauchy algorithm for solving unconstrained optimization problems. The resulting curve obtained from the boundary region projected the negative gradient that can be used in conjunction with other methods with faster rates of convergence that reduces the steepest-descent on the subspace of free variables [27]. The GP method identifies the optimal active set in a finite number of iterations for bound constrained problem proposed by Bertsekas [28]. Later in 1982, Bertsekas derived some results for a projected Newton Method [29] and Gafini & Bertsekas for a 2-metric projection method [30]. Dunn proved that the GP identifies the optimal active constraints in a finite number of iterations in a strict complementary condition [31]. The above statement was extended by Burke and More, and proved that under Dunn's non-degeneracy assumption the optimal active constraints are eventually identified if the projected gradient converges to zero [32]. Calamai and More studied the converging properties of GP and the results were applied for linearly constrained problems [33]. Xu provided an operator oriented mapping approach for providing strong convergence for GPA [34]. Based on the penalty function approach and GPA, Luenberger proposed a new programming algorithm for non-linear constrained optimization [35].

2.2 Algorithm for Fast Gradient Projection

The discrete version of the TV (Total Variance) based de-blurring consists of solving an unconstrained convex minimization problem of the form given in Eq. (1).

$$\min_{x} \|x-a\|_F^2 + 2\lambda |x|_{TV}, \tag{1}$$

where x is the desired unknown image, a is the observed noisy data and λ is the regularization parameter with $\lambda > 0$.

Let us consider $C = B_{l,u}$, then $P_c = P_{Bl,u}$. Thus the GP algorithm can be described in the matrix form shown in Eq. (2).

$$P_{B_{l,u}}(x)_{i,j} = \begin{cases} l & x_{i,j} < l \\ x_{i,j} & l \le x_{i,j} \le u \\ u & x_{i,j} > u \end{cases} \tag{2}$$

where, l is the vector of lower bounds, u is the vector of upper bounds. If $(p,q) \in P$, then the optimal solution of the dual problem with TV based de-noising is described as Eq. (3).

$$\min_{(p,q)\in P} \{h(p,q) \equiv -\|H_c(a-\lambda \mathcal{L}(p,q))\|_F^2 + \|a-\lambda \mathcal{L}(p,q)\|_F^2\} \tag{3}$$

$$\text{Here, } H_c = x - P_c(x) \text{ for every } x \tag{4}$$

When TV=TV$_1$, Eq. (3) is given by

$$x = P_c(a-\lambda \mathcal{L}(p,q)) \tag{5}$$

where P_p is the projection operator which maps a matrix pair (p,q) with another matrix pair $(r,s) = P_p(p,q)$ and can be readily implemented [36].

For a better rate of convergence, the Fast Gradient Projection (FGP) method is used on the dual problem stated in Eq. (3). Considering, $(r_1, s_1) = (p_0, q_0)$ at step 0, and $k = 1, 2, \ldots N$, at step k, α_{k+1} is a sequence of step sizes, Eq. (3) can be denoted as Eqs. (6) and (7).

$$(p_{k+1}, q_{k+1}) = P_p[(r_{k+1}, s_{k+1}) + \frac{1}{8\lambda}\mathcal{L}^T(P_c[a - \lambda\mathcal{L}(r_{k+1}, s_{k+1})])] \tag{6}$$

$$\alpha_{k+2} = \frac{1 + \sqrt{1 + 4\alpha_{k+1}^2}}{2} \tag{7}$$

$$(r_{k+2}, s_{k+2}) = (p_{k+1}, q_{k+1}) + \{(\alpha_{k+1} - 1)/(\alpha_{k+2})\}(p_{k+1} - p_k, q_{k+1} - q_k) \tag{8}$$

2.3 Method for Centerline Straightening

Figure 1 shows the schematic representations of the steps involved in Centreline straightening and are summarized below:

Step 1 The locus of the centerline of the vessel is determined by a routine move along the vessel in few pixels at a time. At each point, the intensities of neighboring pixels are measured to determine the local width of the vessel and the position of the next point of the estimated centerline.

Step 2 The locus of the centerline is smoothed using a customized smoothing function.

Step 3 Intensity profiles of the vessel are taken at each point, with the direction of the profile set perpendicular to the local tangent of the locus.

Step 4 Each point on the locus is moved by a small displacement to make the profile more symmetrical.

Step 5 When the locus has been optimized, an interpolation between the points generates a new locus in which the points are separated by one pixel. Intensity profiles are calculated as described in Step 3 and used to generate the straightened image.

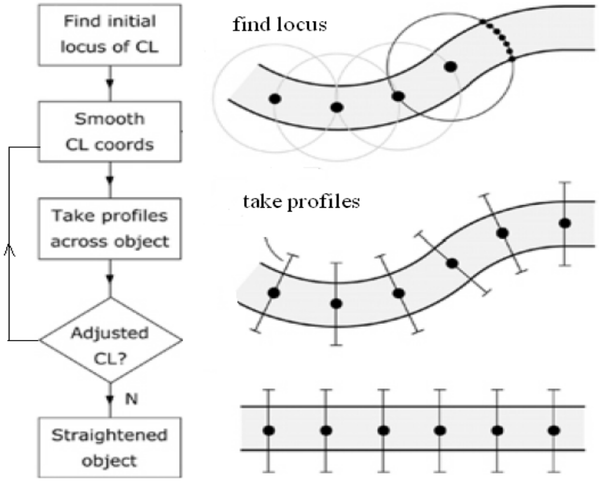

Figure 1. Schematic representation of straighten the blood vessel. The flow diagram on the left side shows how the algorithm loops until a satisfactory result has been achieved (CL refers to the centerline of the vessel). Steps are illustrated on the right side, where the large points are in (or close to) the centerline of the vessel.

Integration of line primitives is performed in the original vector space. To straighten them, a parameterization of the points is created using the local bases from the moving frame. This algorithm performs a piecewise reformation of a line by using the planes defined by the tangent of the moving frame. These planes are defined in a discrete number of equidistant points along the centerline. To create a straightening of a line, integrated from a seed point lying in the tangent plane, we computed all the intersection points of the line with the planes it intersects during the integration, and then transform these intersections from the vector space into the straightening space. This alignment also allows the combination of visualization of the actual data (such as standard flow visualization techniques) with more abstract visualization techniques like the line graph plot of certain quantities along the centerline.

3 Tools and Data

The Straightening algorithms were developed in MATLAB 2011b installed in Pentium-IV 3 GHz processor PC with Window XP operating system. The algorithms developed are tested on various MR images obtained in the DICOM file format. The MR images used in this study were taken from Siemens Esaote ARTOSCAN C MRI Machine with a magnetic field intensity of 0.15 T and sample per pixel value 1 attained with 63.677701 Hz imaging frequency.

4 Results

The algorithm was tested on more than 100 MR images. Here we showed two Noisy (MRBvessel and BRTBvessel) MR images and Smoothing the image using the FGP filtering method that replaces each pixel with the average of its neighborhood. It reduces the Rician noise and increases the contrast of the MR image. A comparative study was attempted for calculating the performance of the developed filters, with existing filtering techniques such as Median filter (MF), Wiener filter (WF), Hybrid median filter (HMF) using the quality metrics such as Peak Signal to Noise Ratio (PSNR), Mean Structure Similarity Index Matrix (MSSIM) and Contrast to Noise Ratio (CNR).

Then, the blood vessels are extracted using the Binarization method for easy visual inspection of vessels from the background tissue images. Individual vessels are selected for straightening by assigning the pixel values. Flattening can be considered of as cutting one side of the vessel wall along the main axis and folding it open to reveal the interior. Centerline can be detected using the tangent function and then the standard visualization techniques can be applied for straightening the vessel along the centerline of the object. The smoothed,

The two Noisy (MRBvessel and BRTBvessel) MR images and their corresponding filtered images, binarized and straightened blood vessel MR images are shown in Figs. 2 and 3. The quality metrics, estimated for these images are given in Tables 1 and 2 respectively.

5 Discussions

From the visual inspection of the smoothed, binarized and straightened blood vessels in MR images by trained radiologists, the following inferences are arrived at:

1. An FGP filtered image exhibits better smoothing, more homogeneity, and contrast improvements over the other filtering methods quantitaively.
2. Extracted RGB Blood vessels are viewed clearly and it is easy to count the vessels within the MR image.
3. Separately detected the infected blood vessel in Tumor and Cancer cells in extracted RGB blood vessels
4. A cropped grayscale image of the vessel is used to select the particular blood vessel and radiologists can view more conveniently the structure of the vessel and problems developed in this vessel.
5. The straightened blood vessel is used to calculate the length and width of the individual vessel and also to compute the tumor affected vessel area.

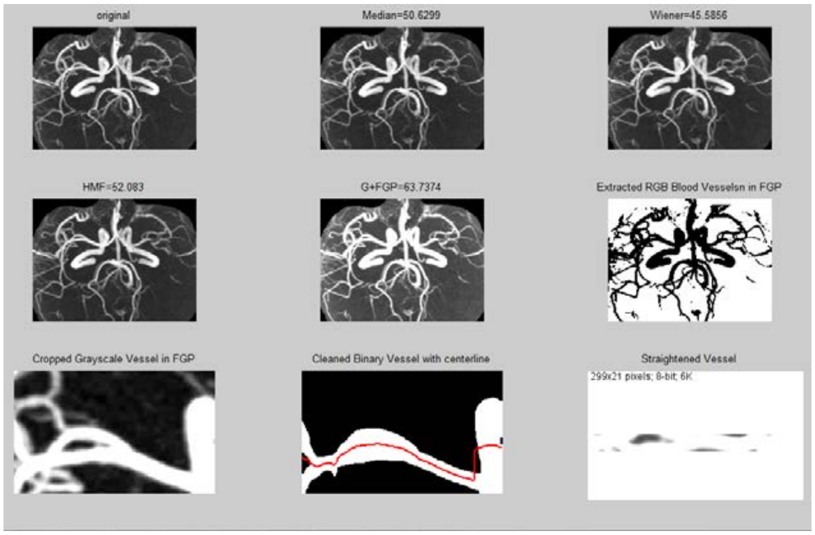

Figure 2. Raw, Smoothed, Extracted and Straightened blood vessels of MRBvessel MR Image.

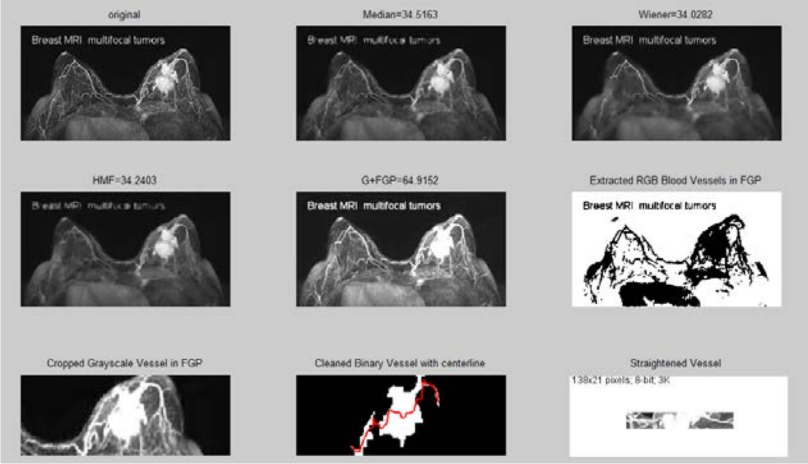

Figure 3. Raw, Smoothed, Extracted and Straightened blood vessels of BRTBvessel MR Image.

Table 1. Estimated Quality Metrics for MR image of MRBvessel

Filters / Parameters	FGP	Median	Wiener	HMF
PSNR	63.7374	50.6299	45.5856	52.0830
MSSIM	0.9962	0.9935	0.9806	0.9954
CNR	1.2293	2.6397e-006	2.5898e-006	4.2911e-006

Table 2. Estimated Quality Metrics for MR image of BRTBvessel

Filters / Parameters	FGP	Median	Wiener	HMF
PSNR	64.9152	34.5163	34.0282	34.2403
MSSIM	0.9969	0.8343	0.8109	0.8056
CNR	1.3533	2.5935e-004	3.2640e-005	4.6144e-004

6 Conclusion

In this work, we implemented the Fast Gradient Projection (FGP) Filter Technique for removing the Rician noise present in MRI images and extracted the vessels using binarization techniques. Further, the blood vessels are cropped and straightened using centerline straightening techniques. The algorithm was tested in typical MR images and the results showed that the FGP removes the signal dependent bias effectively and improved the contrast of the image. The performance of the extracted and straightened blood vessels is more convenient to the radiologist for visual analysis. The results of this study reveal that the smoothed, extracted and straightened images are very much useful for the diagnosis of tissue characterization and tumor detection. In the future scope of this study, the aforementioned techniques will be implemented in the DSPs environment for real time applications.

REFERENCES

[1] Donnell TO, Gupta A, Boult T. A new model for the recovery of cylindrical structures from medical image data. CVRMed-MRCAS 1997;1205:223-32.

[2] Barrett SD, Carvalho CRD. A software tool to straighten curved chromosome images. Chromosome Research Kluwer Academic Publishers 2003;11:83-8.

[3] Zhang S, Levin DC, Halpern EJ, Fischman D, Savage M, Walinsky P. Accuracy of MDCT in Assessing the Degree of Stenosis Caused by Calcified Coronary Artery Plaques. AJR Am J Roentgenol 2008;191(6):1676-83.

[4] Chuang CL, Chen CM. Accurately and Practical Image Segmentation Algorithm in Coronary Artery. IFMBE Proceedings;14:2483-7.

[5] Kanitsar A, Wegenkittl R, Fleischmann D, Groller ME. Advanced Curved Planar Reformation: Flattening of Vascular Structures. IEEE Transaction on Visualization 2003, VIS 2003;43-50.

[6] Kanitsar A, Fleischmann D, Wegenkittl R, Felkel P. CPR – curved planar reformation. IEEE Transaction on Visualization, USA 2002;37-44.

[7] Wang Y. Blood Vessel Segmentation and shape analysis for quantification of Coronary Artery Stenosis in CT Angiography. School of Engineering & Mathematical Sciences Dissertations, City University London 2011.

[8] Wang C. Computer-Assisted Coronary CT Angiography Analysis Curved MPR. Linköping University Medical Dissertations, Sweden 2011;1237.

[9] Zhang DP. Coronary Artery Segmentation and Motion Modelling. Department of Computing Dissertations, Imperial College London 2010.

[10] Wink O, Hecht HS, Ruijters D. Coronary Computed Tomographic Angiography in the Cardiac Catheterization Laboratory: Current Applications and Future Developments. Advances in Coronary Angiography, Cardiology Clinics 2009;27(3):513-29.

[11] Saran A. N., Nar F., and Saran M., Vessel segmentation in MRI using a variational image subtraction approach, Turkish Journal of Electrical Engineering & Comp Sciences, 2014, 22: 499-516.

[12] Lawler LP. CT scanning of the coronary arteries: How to do it and how to interpret it. Appl Radiol 2005;34(10):8-16.

[13] Kanitsar AM. Curved Planar Reformation for Vessel Visualization. Institute for Computer Graphics and Algorithms Dissertation, Vienna University of Technology 2004.

[14] Kim Do-Yeon, 3D volume extraction of cerebrovascular structure on brain magnetic resonance angiography data sets, J. Biomedical Science and Engineering, 2012, 5: 574-9.

[15] Olabarriaga SD, Breeuwer M, Niessen WJ. Evaluation of Hessian-based filters to enhance the axis of coronary arteries in CT images. International Congress Series 2003;1256:1191-6.

[16] Marco Antonio Zenteno M A., Santos-Franco J A., Moscote-Salazar L R., Lee A., Endovascular remodeling of tortuous cervical segments of the internal carotid artery that hinder the

management of complex intracranial aneurysms, Romanian Neurosurgery, 2013, XX(3): 247-57.

[17] Dupej J., Blood Vessel Visualization on CT Data, WDS'12 Proceedings of Contributed Papers, 2012, Part I, 88-93.

[18] Ropinski T, Hermann S, Reich R, Schafers M, Hinrichs K. Multimodal Vessel Visualization of Mouse Aorta PET/CT Scans. IEEE Trans Vis Comput Graph 2009;15(6):1515-22.

[19] Hénault DR, Sundar H, Cheriet M. Nonrigid 2D/3D Registration of Coronary Artery Models With Live Fluoroscopy for Guidance of Cardiac Interventions. IEEE Transactions on Medical Imaging 2012;31(8):1557-72.

[20] Kocsis E, Trus BL, Steer CJ, Bisher ME, Steven AC. Straighten Curved Objects. J. Struct. Biol 1991;107:6-14.

[21] Wassermann D, Adad JC, Lehericy S, Benali H, Rossignol S, Deriche R, Straightening the Spinal Cord using Fiber Tractography. IEEE International Symposium on Biomedical Imaging: From Nano to Macro 2010;1377-80.

[22] Angelelli P, Hauser H. Straightening Tubular Flow for Side-by-Side Visualization. IEEE Transactions on Visualization and Computer Graphics 2011;17(12):2063-70.

[23] Mistelbauer G, Morar A, Varchola A, Schernthaner R, Baclija I, Kochl A, Kanitsar A, Bruckner S, Groller E. Vessel Visualization using Curvicircular Feature Aggregation Existing. Eurographics Conference on Visualization (EuroVis), Computer Graphics Forum 2013;32(3):231-40.

[24] Lee N, Rasch M. Tangential curved planar reformation for topological and orientation invariant visualization of vascular trees. Conf Proc on IEEE Engg Med Biol Soc 2006;1:1073-76.

[25] Goldstein AA. Convex programming in Hilbert space. Bull. Amer. Math. Soc 1964;70:709-10.

[26] Levitin ES, Polyak BT. Constrained minimization problems. U.S.S.R. Comput. Math. Phys. 1966;6(5):1-50.

[27] Bertsekas DP. Nonlinear programming. Athenas Scientific 1995;22-75 and 223-72.

[28] Bertsekas DP. On the Goldstein - Levitin - Polyak Gradient Projection Method. IEEE Transactions on Automatic Control 1976;21(2):174-84.

[29] Bertsekas DP. Projected Newton methods for optimization problems with simple constraints. SIAM J. Control and Optimization 1982;20(2):221-46.

[30] Gafni EM, Bertsekas DP. Convergence of a Gradient Projection Method. Massachusetts Institute of Technology. Laboratory for Information and Decision Systems 1982;1-12.

[31] Dunn JC. On the convergence of projected gradient processes to singular critical points. J. Optim. Theory. Appl 1987;55(2):203-16.

[32] Burke JV, More JJ. On the identification of active constraints. SIAM J. Numer. Anal 1988;25(5):1197-211.

[33] Calamai PH, More JJ. Projected Gradient Methods for linearly constrained problems. Mathematical Programming. Springer-Verlag, New York 1987;39(1):93-116.

[34] Xu HK. Averaged Mappings and the Gradient-Projection Algorithm. J. Optim. Theory. Appl. Springer 2011;150:360-78.

[35] Luenberger DG. A Combined penalty function and gradient projection method for nonlinear programming. J. Optim. Theory. App 1974;14(5):477-95.

[36] Soman KP, Ramanathan R. Digital Signal and Image processing- The Sparse Way. Isa Publishers. Elsevier, New Delhi, 2012;408-16.

SOCIETY FOR SCIENCE AND EDUCATION
UNITED KINGDOM

JBEMi JOURNAL OF BIOMEDICAL ENGINEERING AND MEDICAL IMAGING

ISSN: 2055-1266
VOLUME 2 ISSUE 6

Increasing of Edges Recognition in Cardiac Scintography for Ischemic Patients

Yousif. M. Y. Abdallah
Radiological Science and Medical Imaging, College of Applied Medical Sciences, Majmaah University,
Prince Mogreen Bin Abdelaziz Street, Majmaah, 66, Riyadh (Saudia Arabia);
y.yousif@mu.edu.sa

ABSTRACT

The detection of ischemia heart disease was usually scored by a trained nuclear medicine Physician by determining the ischemia location and size subjectively (by eyes). This subjective method will add to the 5% tolerance error, which might compromise the whole process of treatment especially in patients with severe conditions. The aim of this study is to increase the edge recognition in cardiac scintography images in patients with ischemic heart disease using L*a*b* color space and K-means clustering. First, we read the nuclear cardiac images. We then to convert the images form RGB color space to L*a*b* color space. Then we classify the colors in 'a*b*' space using K-means clustering. Then we label every pixel in the Image using the results from K-means. We then create images that segment the cardiac image by colour. Finally, we segment the cardiac image into a separate image. The sample of this study was (146 cases) and they showed increase enhancement. This segmentation technique (automatic scoring) and segmented images was adjudicated by three nuclear medicine physician as being comparable to other segmentation techniques created with manual editing (subjective scoring). This technique showed potentials increasing of detection of the myocardial ischemia rather than conventional one.

Keywords: Cardiac, Segmentation, MatLab, Ischemic patients.

1 Introduction

The heart is the pump responsible for maintaining adequate circulation of oxygenated blood around the vascular network of the body. It is a four-chamber pump, with the right side receiving deoxygenated blood from the body at low pressure and pumping it to the lungs (the pulmonary circulation) and the left side receiving oxygenated blood from the lungs and pumping it at high pressure around the body (the systemic circulation) [1-4]. The myocardium (cardiac muscle) is a specialized form of muscle, consisting of individual cells joined by electrical connections[5][6]. The contraction of each cell is produced by a rise in intracellular calcium concentration leading to spontaneous depolarization, and as each cell is electrically connected to its neighbor, contraction of one cell leads to a wave of depolarization and contraction across the myocardium. This depolarization and contraction of the heart is controlled by a specialized group of cells localized in the sino-atrial node in the right atrium- the

DOI: 10.14738/jbemi.26.1697
Publication Date: 19th December 2015
URL: http://dx.doi.org/10.14738/jbemi. 26.1697

pacemaker cells [7-9]. These cells generate a rhythmical depolarization, which then spreads out over the atria to the atrio-ventricular node, the atria then contract to push the blood into the ventricles (Tarig Hakim, 2006). The electrical conduction passes via the Atrio-ventricular node to the bundle of His, which divides into right and left branches and then spreads out from the base of the ventricles across the myocardium. This leads to a 'bottom-up' contraction of the ventricles, forcing blood up and out into the pulmonary artery (right) and aorta (left). The atria then re-fill as the myocardium relaxes [10][11].

The 'squeeze' is called systole and normally lasts for about 250 ms (mill second). The relaxation period, when the atria and ventricles re-fill, is called diastole; the time given for diastole depends on the heart rate. The heart needs its own reliable blood supply in order to keep beating; hence it receives the blood via the coronary circulation. There are two main coronary arteries, the left and right coronary arteries, and this branch further to form several major branches (see appendix). The coronary arteries lie in grooves (sulci) running over the surface of the myocardium, covered over by the epicardium, and have many branches which terminate in arterioles supplying the vast capillary network of the myocardium. However these CA frequently susceptible to many disorders and diseases; of either acquired or congenital one [12], such as: (septum patency as congenital and Ischemic and Infarction diseases as acquired), and the focus of this research is to characterize the CA Obstruction and Related Findings in Ischemic Heart Patients Using Cardiac Scintigraphy. Indeed such obstruction could accompany with fatal consequences or morbidities. Radionuclide Scintigraphy during exercise permits accurate assessment of the presence and functional severity of ischemic heart disease. Worldwide the CAO has been as an endemic disease in some countries, such as USA (American Heart Association) [13]. In Sudan, the CAO has been observed increases in some patients with vague etiology, although the main causes mentioned by American Heart Association, was Fats or Embolus in contrast to these causative factors, the CAO patients may have other causes rather than that mention in literature. Therefore the researcher could highlight the co-factors that induce such CAO and further the related consequences [14][15].

2 Materials and Methods

This was experimental study conducted to study segmentation of colour ischemic heart image using colors segmentation filters of MatLab image processing program. The study included all adults patients referred for suspected CAO or Ischemic heart disease in Nuclear medicine department of Elnileen Medical center of Khartoum and Fadil Specialist Hospital.

2.1 Patient’s preparations

When the patients referred for heart scintigraphy, the patients asked to stop the medication for 24 hours before the study, as well as Caffeine containing foods or drinks, because it reduced the radiotracer uptake. Also asked for fasting after night till the intravenous injection of the radiopharmaceutical, after the injection time about 15 to 20 minutes the patient asked to eat a fatty meal and chocolate for the good excretion of the gall bladder (it has normal high uptake of the radiotracer).

2.2 Imaging scanning technique:

After 45 min to 1 hour after the injection the patient entered to the gamma camera for imaging, and asked to pick out his/her upper clothes and lie supine in the imaging table to fix the ECG electrodes on his upper right side near Rt. Clavicle, Lt. Clavicle and Lt. lower thoracic vertebrae. Then the computer already set on the gated SPECT for the rest hear study, and the machine started the acquisition form the RAO (-45 degree) to LPO (135 degree), step and shoot technique till the acquisition finished. Then the processing of the acquired study by SPECT protocol for obtaining the serial images of sliced heart (Coronal, Sagittal and Transverse cuts), as well as bollar map and Ejection fraction of the heart and any available information if interested on A4 paper with a colored scale. For the Stress heart Scintigraphy used the same process that of Rest study in addition to using treadmill as exercise for elevating the heart rate or Pharmacological agent (Persantin) as stress action after the heart reaches his maximum effort then the radiopharmaceutical should be injected, then all process as same as the Rest study.

For nuclear cardiology images, each image scanned using digitizer scanner then treated by using image processing technique (MatLab), where the segmentation was studied. The scanned images were saved in PNG and 600 dpi file format to preserve the quality of the image. We used Color-Based Segmentation Using K-Means Clustering Algorithm to enhance the cardiac images. The steps of segmentation were shown in the Fig. 1 as below:

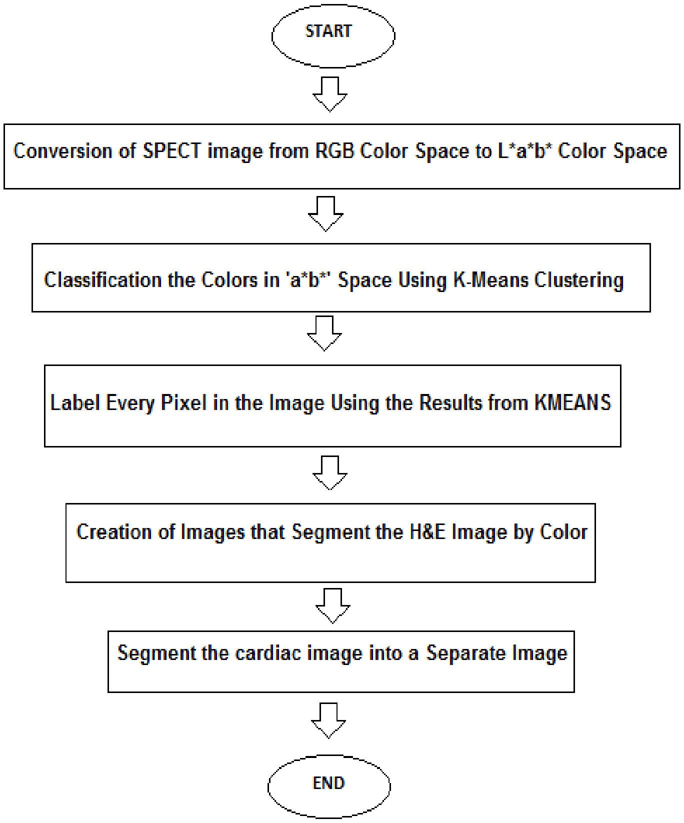

Figure 1. Steps of Colour-Based Segmentation Using K-Means Clustering

3 The results

This was experimental study conducted to study segmentation of colour ischemic heart image using colours segmentation filters of MatLab image processing program. The sample of this study was 146 patients with different age distribution and body mass index. For the group of patients where age distribution was measured, 1.2 % of patients were within the 20-29 years age range, 5 % of patients were within the 30-39 years age range, 16 % of patients were within the 40-49 years age range, 35 % of patients were within the 50-59 years age range, 34.6 % of patients were within the 60-69years age range, 7 % of patients were within the 60-69 years age range and 1.2 % of patients were within the 80-89 years age range Figure 2 and Figure 3.

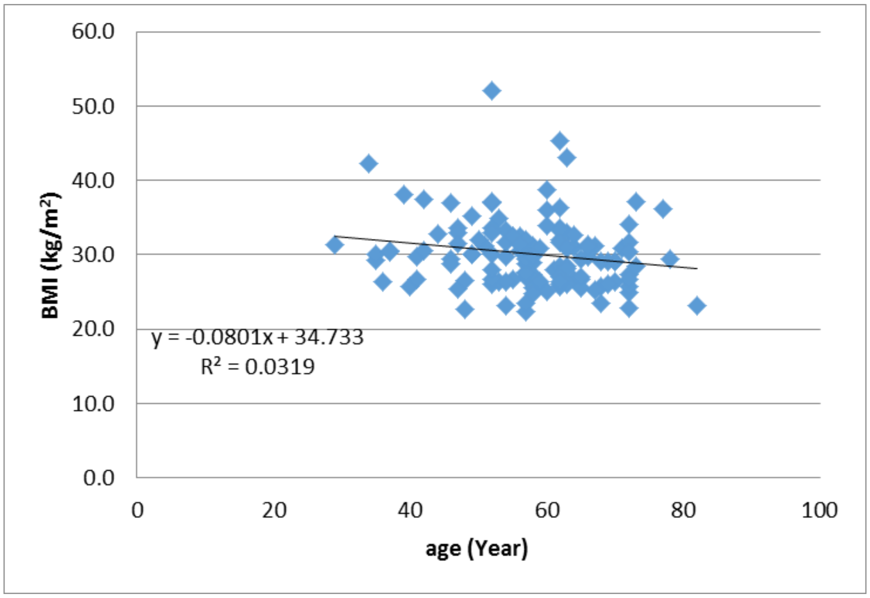

Figure 2. Correlation between age of patient and BMI

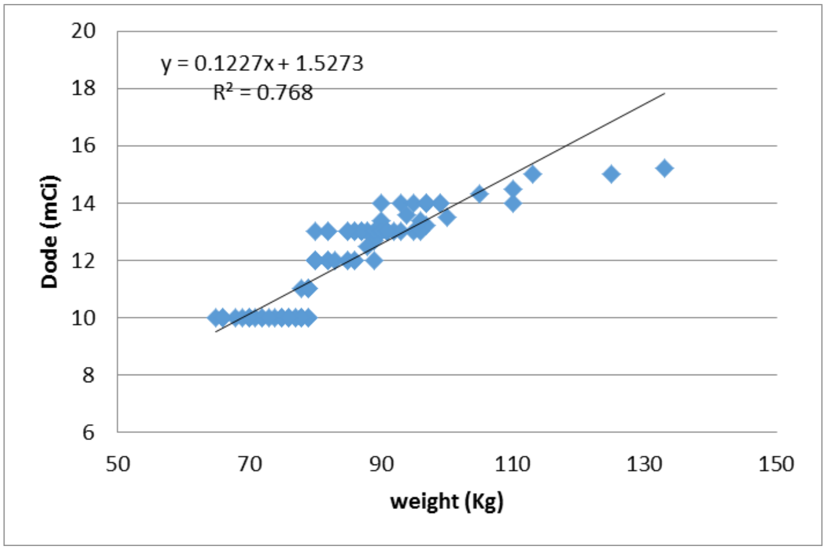

Figure 3. Correlation between the body weight (Kg.) and radiation dose (mCi) of study

In this study firstly, I read in SPECT image with extension PNG, which is a colour ischemic heart image. This colour method helps nuclear medicine physician or cardiologist distinguish different heart tissue types Figure 4.

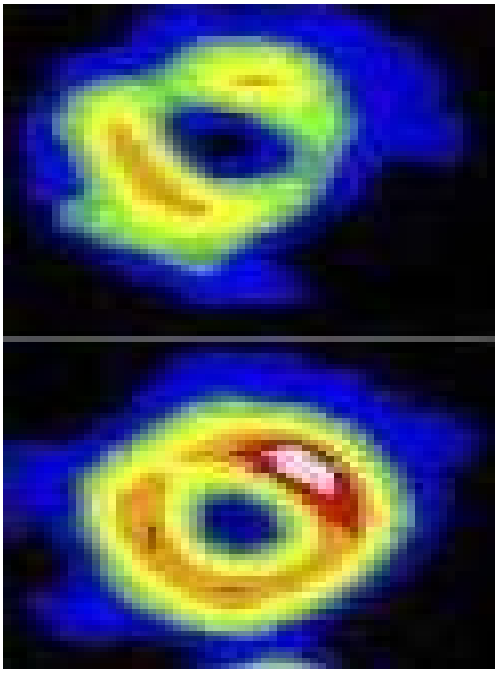

Figure 4. Original cardiac images

Many colours can notice in the cardiac image if one ignore variations in brightness. There are three colors: white, blue, and pink. It is easily to distinguish these colors from one another easily. The L*a*b* color space (also known as CIELAB or CIE L*a*b*) enables us to quantify these visual differences. The L*a*b* color space is derived from the CIE XYZ tristimulus values. The L*a*b* space consists of a luminosity layer 'L*', chromaticity-layer 'a*' indicating where color falls along the red-green axis, and chromaticity-layer 'b*' indicating where the color falls along the blue-yellow axis. All of the color information is in the 'a*' and 'b*' layers. We measured the difference between two colors using the Euclidean distance metric. In this study we converted the image to L*a*b* color space using makecform and applycform (forward transformation). The RGB or CMYK values first need to be transformed to a specific absolute color space, such as sRGB or Adobe RGB. This adjustment will be device dependent, but the resulting data from the transform will be device independent, allowing data to be transformed to the CIE 1931 color space and then transformed intoL*a*b*.The L* coordinate ranges from 0 to 100. The possible range of a* and b* coordinates is independent of the colour space that one is converting from, since the conversion below uses X and Y which come from RGB.

The forward transformation

$$L^* = 116\left({}^{Y}/_{Y_n}\right) - 16 \tag{1}$$

$$a^* = 500\left[f\left({}^{X}/_{X_n}\right) - f\left({}^{Y}/_{Y_n}\right)\right] \tag{2}$$

$$b^* = 200\left[f\left({}^{Y}/_{Y_n}\right) - f\left({}^{Z}/_{Z_n}\right)\right] \tag{3}$$

Where,

$$f(t) = \begin{cases} t^{1/3} & if t > \left(\frac{6}{29}\right)^3 \\ \frac{1}{3}\left(\frac{29}{6}\right)^2 t + \frac{4}{29} & otherwise \end{cases} \tag{4}$$

Where X_n ,Y_n and Zn are the CIE XYZ tristiulus values of the reference white point. The devision of the f function into two domains was done to prevent an infinite slope at t=0. was assumed to be linear below some t = t0, and was assumed to match the $t^{1/3}$ part of the function at t0 in both value and slope as shown in Fig.5.

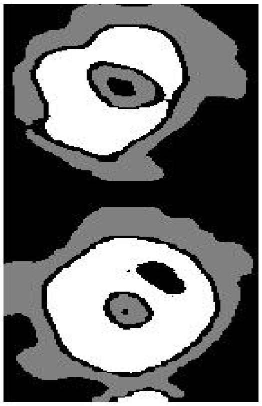

Figure 5. Image labelled by cluster index

We used K-means clustering in order to treat each object as having a location in space. It found partitions such that objects within each cluster are as close to each other as possible, and as far from objects in other clusters as possible. We specified the number of clusters to be partitioned to 3 and a distance metric to quantify how close two tissues in cardiac scintography to each other. Since the color information exists in the 'a*b*' space,the objects are pixels with 'a*' and 'b*' values. Use kmeans to cluster the objects into three clusters using the Euclidean distance metric as shown in Fig.6.

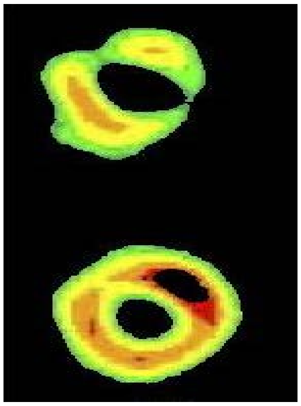

Figure 6. Cardiac image in cluster 1 Kmeans algorithm

For every structure in our input (cardiac images), kmeans returned an index corresponding to a cluster. The cluster_center output from kmeans would be used later in the demo. Every pixel was label in the image with its cluster_index Fig.7.

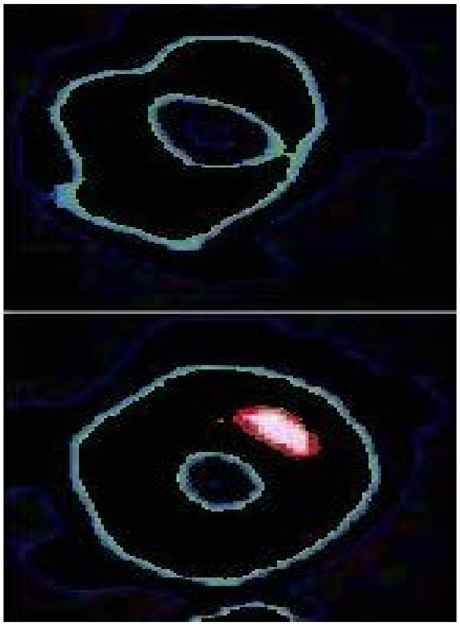

Figure 7. Cardiac image in cluster 2 Kmeans algorithm

Using pixel_labels, I separate stuctures in cardiac images by color, which would result in three images Fig.8.

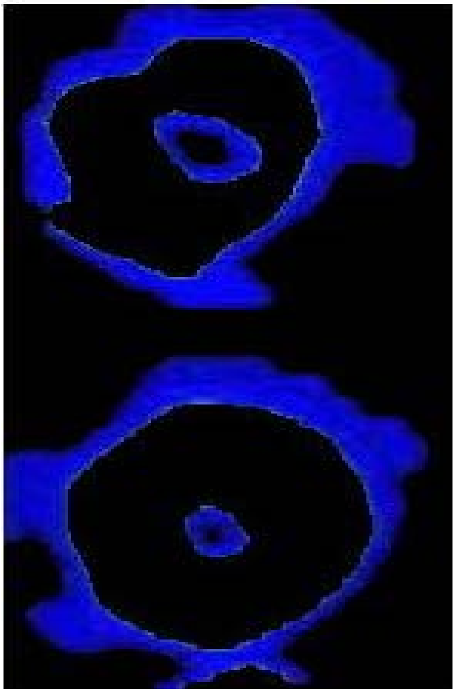

Figure 8. Cardiac image in cluster 3 Kmeans algorithm

There were dark and light color strutures in one of the clusters. I separated dark blue from light blue using the 'L*' layer in the L*a*b* color space. We recalled that the 'L*' layer contains the brightness values of each color. Then I found the cluster that contained the blue objects. We extracted the brightness values of the pixels in this cluster and threshold them using im2bw. I programmatically determined the index of the cluster containing the blue objects because kmeans would return the same cluster_idx value every time. I could do this using the cluster_center value, which contains the mean 'a*' and 'b*' value for each cluster. The blue cluster has the smallest cluster_center value (determined experimentally). Finally, I used the mask is_light_blue to label which pixels belong to the cardiac structure. Then I displayed the blue color in a separate image Fig.9.

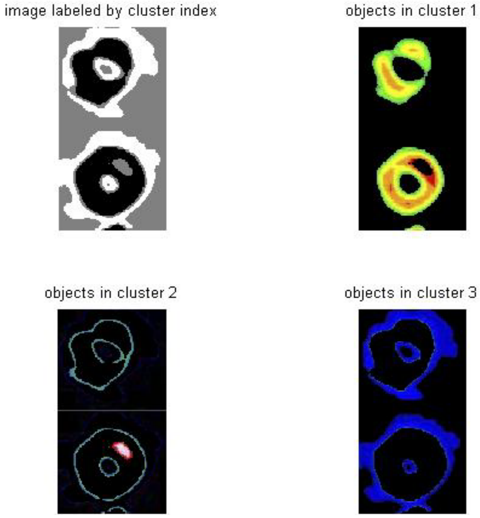

Figure 9. Segmentation of the cardiac images into a Separate Image

4 Conclusion

The common co-factors associated with the CAO include: Wight, Height, Instant Foods (Jungle meals), Smoking, which contribute in occurrence or severity of the Ischemic disease. Concerning the Age there was strong relation with Myocardial Ischemia in a relation with CAO, which is more manifested in oldest Age group found to be most severe than the descending other Age groups representing as mild or moderate. Concerning the BMI there was very strong inverse relation in having the Ischemia in association with CAO with a description of severe, moderate and mild. Segmentation used to identify the object of image that we are interested. The nuclear cardiology has become a common way to study myocardial disorders. Most images that created cardiac images were not completely clear and some had high signal noise ratio, which affected myocardial borders detection. The main objective of this research was to increase of edges recognition in cardiac scintigraphy for ischemic patients. In addition to detect the border of entire heart using segmentation, filter technique. These techniques help in preservation of the image's overall look, detected of small and low contrast details in the diagnostic content of the image, and highlighted the role of using image-processing technique in nuclear medicine. The result of edge detection now closely matches the original in-memory result comparing with others studies using different segmentation techniques. So conclusion of this paper that colour segmentation using K-means tools are best tools to detect heart and it structure which is very beneficial special in patients with ischemic heart disease. The detection of the noise is a complex procedure, which is difficult to detect by naked eye so that image analysis should perform by using powerful image processing. A colour K-means segmentation Algorithm of heart is proposed in myocardial heart study. Proposed method is able to determine the heart boundaries accurately. It is able to segment heart and improves radiological analysis and diagnosis.

REFERENCES

[1] Kim KI, Bae J, Kang HJ, Koo BK, Youn TJ, Kim SH, Chae IH, Kim HS, Sohn DW, Oh BH, Lee MM, Park YB, Choi YS, Lee DS. Three-year clinical follow-up results of intracoronary radiation therapy using a rhenium-188-diethylene-tri-amine-penta-acetic-acid-filled balloon system. Circ J. 2004.68:532 -537.

[2] Abdallah, Y., and Wagiallah, E., Segmentation of Thyroid Scintography Using Edge Detection and Morphology Filters. International Journal of Science and Research (IJSR), 2014.3(11): 2768-2772.

[3] Abdallah, Y., and Hassan, A., Segmentation of Brain in MRI Images Using Watershed-based Technique. International Journal of Science and Research (IJSR), 2015. 4(1): 683-688.

[4] Abdallah, Y., and Yousef R., Augmentation of X-rays Images using Pixel Intensity Values Adjustments. International Journal of Science and Research (IJSR), 2015. 4(2): 2425-2430.

[5] Koo B-K, Lee M-M, Oh S, Chae I-H, Kim H-S, Sohn D-W, Oh B-H, Park Y-B, Choi Y-S, Lee DS.. Effects of q-radiation with a 188rhenium-filled balloon catheter system on non-stented adjacent coronary artery segments. Int J Cardiol. 2004.96:73 -77

[6] Delbeke, D.; Coleman, R.E.; Guiberteau M.J.; Brown, M.L.; Royal, H.D.; Siegel, B.A.; Gonzalez, R.; Woods, R., & Eddins, S. Digital Image Processing using MATLAB, (second edition), Gatesmark Publishing, 2011.

[7] Lehmann, T.M.; Gönner, C. & Spitzer, K. Survey: Interpolation Methods in Medical Image Processing. IEEE Transactions on Medical Imaging, 2009.(18)11:1049-1075

[8] Li, G. & Miller, R.W. Volumetric Image Registration of Multi-modality Images of CT,MRI and PET, Biomedical Imaging, Youxin Mao (Ed.) InTech. 2010.

[9] Lyra, M.; Sotiropoulos, M.; Lagopati, N. & Gavrilleli, M. Quantification of Myocardial Perfusion in 3D SPECT images – Stress/Rest volume differences, Imaging Systems and Techniques (IST), 2010 IEEE International Conference on 2010. 31-35,

[10] Lyra, M.; Striligas, J.; Gavrilleli, M. & Lagopati, N. Volume Quantification of I-123 DaTSCAN Imaging by MatLab for the Differentiation and Grading of Parkinsonism and Essential Tremor, International Conference on Science and Social Research, Kuala Lumpur, Malaysia2010. 5-7.

[11] MathWorks Inc. MATLAB User’s Guide. The MathWorks Inc., United States of America.2012.

[12] Nailon, W.H. Texture Analysis Methods for Medical Image Characterisation, Biomedical Imaging, Youxin Mao (Ed.), InTech. 2010.

[13] O’ Gorman, L.; Sammon, M. & Seul M. Practicals Algorithms for image analysis, (second edition), Cambridge University Press, United States of America. 2008. 115-129.

[14] Perutka K. Tips and Tricks for Programming in Matlab, Matlab - Modelling, Programming and Simulations, Emilson Pereira Leite (Ed.), InTech.2010. 234-245

[15] Toprak, A. & Guler, I.. Suppression of Impulse Noise in Medical Images with the Use of Fuzzy Adaptive Median Filter. Journal of Medical Systems, 2006.(30):465-471

[16] Abdallah, Y., Application of Analysis Approach in Noise Estimation, Using Image Processing Program. Lambert Publishing Press GmbH & Co. KG. 2011. 123-125

SOCIETY FOR SCIENCE AND EDUCATION
UNITED KINGDOM

JBEMi JOURNAL OF BIOMEDICAL ENGINEERING AND MEDICAL IMAGING

ISSN: 2055-1266
VOLUME 2 ISSUE 6

Surface Energetics of Mycobacterium Tuberculosis – Macrophage Interactions

[1]Chukwuneke J. L., [1]Achebe C. H., [2]Ejiofor O. S. and [3]Sinebe J. E.
[1]*Department of Mechanical Engineering, Nnamdi Azikiwe University, Awka, Nigeria*
[2]*Department of Paediatrics, Anambra State University Teaching Hospital, Awka, Nigeria*
[3]*Department of Mechanical Engineering, Delta State University, Oleh, Nigeria*
jl.chukwuneke@unizik.edu.ng

ABSTRACT

The surface thermodynamics of M-Tb/HIV-macrophage interactions were studied using the Hamaker coefficient concept as a surface energetics tool in determining the interaction processes. The surface interfacial energies were explained using van der Waals concept of particle - particle interactions. The method involved sputum sample collection, mycobacterium and macrophages structural studies, and the study of the mechanism of interaction of the bacterium and the macrophage. Twenty samples each of infected, uninfected and M-Tb/HIV co-infected sputum were collected. Each specimen was screened to determine the infection status using GeneXpert and Ziehl-Neelsen staining methods. The absorbance, ā, values of each specimen, for wavelength range of 230 – 950nm were measured using digital Ultraviolet Visible Spectrophotometer. From the absorbance data the variables (e.g. dielectric constant, etc.) required for computations were derived. MatLab software tools were employed in the mathematical analysis. The Hamaker constants, combined Hamaker coefficients and absolute combined Hamaker coefficients were obtained. The values of $A_{132abs} = 0.21631x10^{-21}$Joule and $\tilde{A}_{132abs} = 0.18825x10^{-21}$Joule were obtained for M-Tb and M-Tb/HIV infected sputum respectively. The implication of this result is the positive value of the absolute combined Hamaker coefficient which entails net positive van der waals forces demonstrating an attraction between M-Tb and the macrophage. This however, implies that infection is very likely to occur. It was also shown that in the presence of HIV, the interaction energy is reduced by 13% confirming adverse effects observed in HIV patients suffering from tuberculosis. The lower value for the combined Hamaker coefficient $A_{131abs} = 10165\ x10^{-21}$Joule for the uninfected sputum samples is an indicator that a negative Hamaker coefficient is realistic. The desired outcome is that the bacteria do not adhere to the macrophage to avoid penetration, in which case a condition for rendering combined Hamaker coefficient negative is required. Thus, condition was sought for repulsion to occur and that condition was based on the value of A_{33} that would render the absolute combined Hamaker coefficient negative. To achieve the condition of A_{33} above, possible additive(s) in form of drugs to the sputum should be required.

Keywords: Absorbance, Dielectric Constant, Energetics, Hamaker Coefficient, Lifshitz Formula, Macrophage, Mycobacterium Tuberculosis, Surface Interfacial, van der Waals Forces, Wavelength

DOI: 10.14738/jbemi.26.1662
Publication Date: 20th December 2015
URL: http://dx.doi.org/10.14738/jbemi. 26.1662

1 Introduction

Tuberculosis (Tb) is an airborne disease caused by the bacterium Mycobacterium Tb (M-Tb). This causative agent of Tb, is one of the world's most devastating human pathogens. The contagious disease is transmitted through air and most commonly affects the lungs, which is responsible for more than 75% of cases (De Souza, 2006). The initial infection usually occurs in the lungs and in most cases is controlled by the immune system. Even after successful control of primary Tb infection, some bacilli remain in a non- or slowing replicating state, termed latent Tb infection (LTbI). Latently infected individuals have a 10% risk of developing the disease in their lifetime (WHO, 2012), which constitutes a huge global reservoir of infection and a continuous threat of disease transmission.

Tuberculosis (Tb) is the leading infectious killer worldwide; it is estimated that one-third of the world's population is currently infected with Tb, and it results in 3 million deaths every year (WHO, 2005). Human Immunodeficiency Virus (HIV) is a strong risk factor for developing active Tb, and Tb is the leading cause of death among HIV-positive individuals. Out of 4.1 million AIDS deaths in 2004, 13% can be attributed to Tb (WHO, 2005).

The highest incidence of disease is in Sub-Saharan Africa, in part due to association with Human Immunodeficiency Virus (HIV) (Nunn et al, 2005; Maartens and Wilkinson, 2007), which has fuelled dramatic rises in incidence of the disease in many countries. [Globally, Tb is the proximate cause of many HIV-related deaths, particularly in Africa (Corbett et al, 2006)]. Even in many countries where its overall incidence is low, Tb remains a problem.

A review of the Tb cases reported by 134 countries between 1998 and 2007 found that only 35 had per capita rates of decline exceeding 5% per year (Adeeb et al, 2013). Surveillance and mathematical modeling suggests that the total Tb incidence per capita is falling at an estimated 1% per year, a finding that indicates that the global incidence rate will decrease by 2015. The world's population is growing at about 2% per year, and thus the total number of new TB cases remains on the rise (WHO, 2009). This finding reveals the relative failure of the existing management strategies for Tb and the inadequate effectiveness of public health systems, mainly in underdeveloped countries.

In spite of the availability of some effective treatment, the steady emergence of multi-drug resistant (MDR), extremely drug-resistant (XDR) and totally drug-resistant strains (TDR) forms of TB is a cause of concern. Globally MDR-Tb accounts for roughly 3.6% of all Tb cases, but accounts for up to 28% of Tb cases in some regions (De Souza, 2006; Gonzalez-Juarrero et al, 2001). The emergence of MDR, XDR and TDR Tb is very worrying due to the increasing difficulty of treating these forms of Tb and rendering even the frontline drugs inactive.

In addition, drugs such as Rifampicin have high levels of adverse effects making them prone to patient incompliance. Another important problem with most of the anti-mycobacterials is their inability to act upon latent forms of the bacillus. To compound the problems further, the deadly associations between the HIV and TB makes the treatment of co-infected patients even more challenging (Nunes et al, 2011; Gonzalez-Juarrero et al, 2001). Much research has been and is still on, on the subject with a cure not yet in view. The choice to approach this issue via the vehicle of surface thermodynamics energetics against the conventional clinical methods is a novel one. The role of surface properties in this biological process will be established.

In this study, it is of interest to understand how the mycobacterium tuberculosis (M-TB) interacts with the macrophage. The process involves the bacterium (modeled as a particle) in a liquid medium (sputum) attaching itself on the surface of the macrophage (another particle), penetrating and probably destroying it. The condition under which bacterium attachment on the surface of the macrophage does not take place will be sought, even in the presence of HIV with its destructive effect.

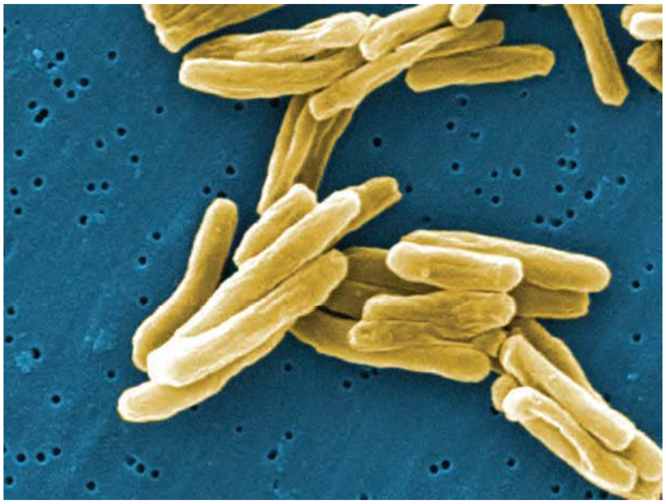

Figure.1: Mycobacterium Tuberculosis

The Lifshiftz derivation for van der Waals forces is used to model the interaction to predict the nature of interaction between two solid particles suspended in a liquid medium (Sputum). Hamaker Coefficient is a significant thermodynamic energetics tool used in determining the interaction processes and will be used in these M-Tb – Macrophage interactions. It is a well-known fact that surface property determination of interacting particles leads to the further understanding of the mechanism of interactions. A common area of contact is established once two solid particles meet each other. In such process, a certain portion of each particle gets displaced through work. Work responsible for the displacement of a unit area is known as surface free energy. The consecutive impact on the surface is known as surface thermodynamic energetics effects. In this particular study similar concepts have been implemented to characterize the M-Tb – macrophage interactions with the sputum as the intervening medium.

2 Methodology

2.1 Sample Collection, Preparation and Measurement

The methodology involved sputum sample collection, mycobacterium and macrophages structural studies, mycobacterium tuberculosis screening, and the study of the mechanism of interactions of the bacterium and the macrophage. Twenty samples each of infected, uninfected and M-Tb/HIV co-infected sputum were collected from Anambra State University Teaching Hospital (ANSUTH) Awka. Each specimen was screened to determine the infection status using GeneXpert and Ziehl-Neelsen staining method thus giving a total of sixty sputum samples from different individuals.

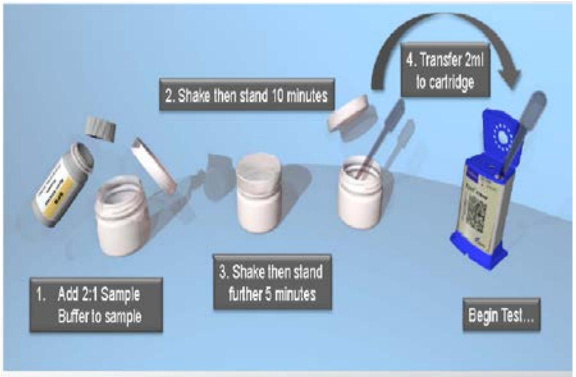

Figure. 2: Sample Preparation: direct sputum

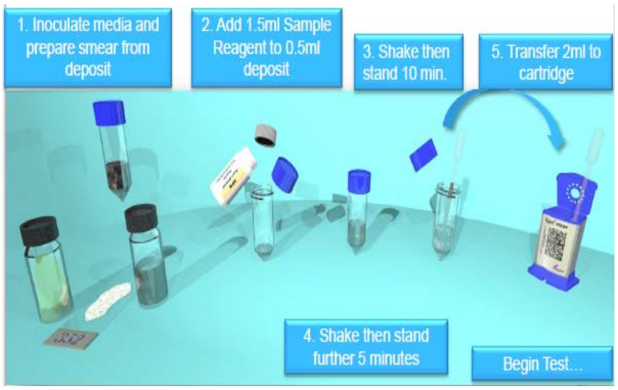

Figure. 3: Sample Processed Sputum Sediment

The glass slides of 25.4mm x 76.2mm x 1.2mm were prepared for test surfaces. A dropper was used to draw each of the Sputum samples from the container and smeared carefully on a slide to ensure even distribution of the sputum samples on the slides. The slide preparations and sample smearing were done at the same laboratory (Chest Clinic/Laboratory, Anambra State University Teaching Hospital, Awka). The samples were allowed to dry naturally at room temperature because exposing the prepared slides to the sun is likely to cause oxidation and the surface energy might be increased unconditionally. All the well prepared and dried surfaces were covered with microscopic cover slip and the absorbance, ā, values of each specimen, for wavelength range of 230 – 950nm were measured using digital Ultraviolet Visible Spectrophotometer (UV/VIS MetaSpecAE1405031Pro). The data generated and the various equations governing the relationship among the variables were used in calculating values for the reflectance, R, transmittance, T, refractive index, n, and the dielectric constant, ε. MatLab software tools were employed in the mathematical analysis of the data generated from the absorbance values.

2.2 Mathematical Applications to the System

To be able to use the absorbance data to calculate the Hamaker coefficients using the Lifshitz theorem, there is a need to evaluate the dielectric constant ε of the equation. Some relevant equations are required. From the information of light absorbance, reflection and transmittance, it could be seen that;

$$\bar{a} + T + R = 1 \tag{1}$$

Where; ā is absorbance, T is transmittance, and R is reflectance. Also, from the information of light absorbance and transmittance;

$$T = \exp^{-\bar{a}} \tag{2}$$

With the values of ā determined from absorbance experimental results, and substituting the values of ā into Eq. (2) to obtain T; R could easily be derived by substituting the values of ā and T into Eq.(1).

The value for the refractive index, *n* employing the mathematical relation (Robinson, 1952);

$$n = \left[\frac{1 - R^{1/2}}{1 + R^{1/2}}\right] \tag{3}$$

Value for the extinction coefficient, *k* is obtained from the equation;

$$k = \left[\frac{\alpha\lambda \times 10^{-9}}{4\pi}\right] \tag{4}$$

Where; α is the absorption coefficient defined as follows;

$$\alpha = \left[\frac{\bar{a}}{\lambda \times 10^{-9}}\right] \tag{5}$$

Substituting the value, α of Eq. (5) into Eq. (4);

$$k = \left[\frac{\bar{a}}{4\pi}\right] \tag{6}$$

The dielectric constant, ε could thus be given by the formula (Charles, 1996);

For the real part;

$$\varepsilon_1 = n_1^2 - k^2 \tag{7}$$

For the imaginary part;

$$\varepsilon_2 = 2n_2k \tag{8}$$

With these values, it is possible to determine A_{ij} using the relevant equations to determine A_{11}.

$$A_{11} = 2.5\left[\frac{\varepsilon_{10} - 1}{\varepsilon_{10} + 1}\right]^2 = 2.5\left[\frac{n_1{}^2 - 1}{n_1{}^2 + 1}\right]^2 \tag{9}$$

This gives a value to the Hamaker constant $A_{11,}$ and by extension to other Hamaker constants A_{22} and $A_{33.}$

For a combination of two disimilar materials (i.e. macrophage, 1 and the bacteria, 2) with the gap between 1 and 2 filled with sputum as the medium 3 (see Fig. 4).

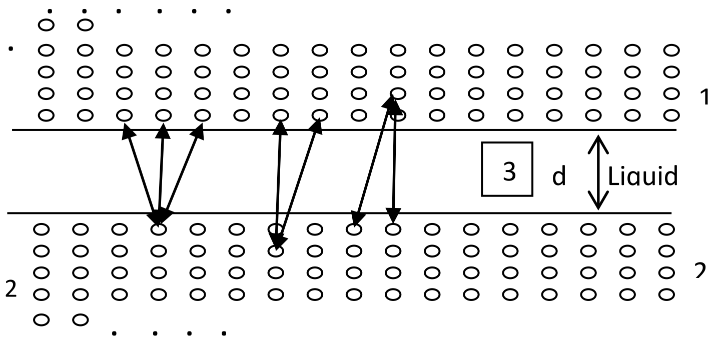

Figure. 4: Schematic representation of interaction of two solid bodies, depicted by 1 and 2 which are eventually isolated by d, in liquid 3.

Thus, the combined Hamaker coefficient, A_{131}, A_{232} and A_{132} could be gotten from the relations [Hamaker, 1937; Visser, 1981; Chukwuneke et al, 2015];

$$A_{131} = A_{11} + A_{33} - 2A_{13} \tag{10a}$$

Alternatively;
$$A_{131} = \left(\sqrt{A_{11}} - \sqrt{A_{33}}\right)^2 \tag{10b}$$

$$A_{232} = A_{22} + A_{33} - 2A_{23} \tag{11a}$$

Alternatively;
$$A_{232} = \left(\sqrt{A_{22}} - \sqrt{A_{33}}\right)^2 \tag{11b}$$

$$A_{132} = A_{12} + A_{33} - A_{13} - A_{23} \tag{12a}$$

Alternatively;
$$A_{132} = \left(\sqrt{A_{11}} - \sqrt{A_{33}}\right)\left(\sqrt{A_{22}} - \sqrt{A_{33}}\right) \tag{12b}$$

Equation (12b) shows that, for a three-component system involving three different materials, 1, 2 and 3, A_{132} can become negative;

$$A_{132} \prec 0 \tag{13}$$

When;
$$\sqrt{A_{11}} \succ \sqrt{A_{33}} \, and \sqrt{A_{22}} \prec \sqrt{A_{33}} \tag{14}$$

$$\sqrt{A_{11}} \prec \sqrt{A_{33}} \prec \sqrt{A_{22}} \tag{15}$$

Hamaker's approach to the interaction between condensed bodies from molecular properties called microscopic approach has limitations. This is true against the backdrop of its neglect of the screening effect of the molecules which are on the surface of two interacting bodies as regards the underlying molecules. Therefore, Hamaker's approach is regarded as an over simplification.

A system containing two planes could be considered for computing the free energy of interaction. This can be done for semi-infinite, parallel bodies belonging to material 1 and 2 isolated by material 3, bearing thickness d (refer fig.4) provided in the following section (Hamaker, 1937; Lifshitz et al, 1961).This is calculated by the following equation:

$$\Delta F_{132}(d) = \left[-\frac{A_{132}}{12\pi d^2}\right] \tag{16}$$

In this, A_{132} refers to the Hamaker coefficient for a respective system.

Considering nominal isolation distance d_0, and Eq (16) as valid for such a small distance, the Hamaker coefficient should be expressed as (Chukwuneke et al, 2015; Hamaker, 1937; Lifshitz et al, 1961):

$$A_{132} = -12\pi d_o^2 \Delta F^{adh}(d_o) \tag{17}$$

The Hamaker coefficient A_{132} for the interactions between two different bodies in a liquid can be calculated from Eq.(17) once the free energy of adhesion between the two bodies is known or through the pair-wise additivity approach as originally proposed by (Hamaker, 1937) or by the macroscopic approach of (Lifshitz et al, 1961). Influence of neighbouring atoms remains major hurdle during the pair-wise summation computing between various molecular interactions. In case of highly disperse media such influence is insignificant, for instance, gases whereas for condensed media it is important (Visser, 1981).

As the actual material atomic structures are overlooked, the Lifshitz method is suitable in certain cases. In this method, bulk material properties are considered for calculation of interactions between the macroscopic bodies. Properties like refractive indices and dielectric permittivity $\varepsilon(i\zeta)$ are considered for such calculations.Dielectric permittivity represents the microscopic polarizability as a manifested macroscopic property for the constant atoms belonging to certain materials. The Hamaker coefficient represents the macroscopic resultant for the interactions happened due to the atom polarizations in a material (Hough and White, 1987).

Following Lifshitz theory, the Hamaker coefficient is represented as follows:

$$A_{ikj} = \frac{3}{4}\pi\hbar\int_0^\infty \left[\frac{\varepsilon_i(i\zeta)-\varepsilon_k(i\zeta)}{\varepsilon_i(i\zeta)+\varepsilon_k(i\zeta)}\right]\left[\frac{\varepsilon_j(i\zeta)-\varepsilon_k(i\zeta)}{\varepsilon_j(i\zeta)+\varepsilon_k(i\zeta)}\right]d\zeta \tag{18}$$

Where, $\varepsilon_j(i\zeta)$ refers to the dielectric constant of a specific material j, this is considered through the imaginary i, frequency axis ($i\zeta$), ђ is planck's constant. In this context, the evaluation of Eqn. (6) should result in equivalent value with the thermodynamic free energy of adhesion, provided in Eqn. (19):

$$\Delta F_{132}^{adh}(d_o) = \gamma_{ps} - \gamma_{pl} - \gamma_{sl} \tag{19}$$

The molecular contact was maintained at (d=0). Interestingly, constituent molecule numbers are of finite size and for that it is not possible to attain d=0 for two macroscopic surface. Therefore, whenever the surfaces attain a distance d_o, molecular contacts are considered. The divergences according to Lifshitz theory are eliminated by the parameter d_o.

Thus, the Hamaker coefficient or the Lifshitz-van der Waals constant A_{132} may result in negative. In certain condition, the contact between the interacting particles will be hampered due to the repulsive (electrostatic) force originated. The resultant effect in certain cases remains as repulsion instead of attraction for the considered particles. The Hamaker coefficient and the interfacial free energies are connected through the following equation:

$$A_{132} = -12\pi d_o^2(\gamma_{12} - \gamma_{13} - \gamma_{23}) \tag{20}$$

This equation has been derived through combining Eqn. (17) with Eqn. (19).

For the issue of self-interaction of a particle Eqn. (8) should be considered;

$$A_{ij} = \frac{3}{4}\pi\hbar\int_0^\infty \left[\frac{\varepsilon_i(i\zeta)-\varepsilon_j(i\zeta)}{\varepsilon_i(i\zeta)+\varepsilon_j(i\zeta)}\right]^2 d\zeta \tag{21}$$

3 Results and Discussion

The raw data obtained for both M-Tb and M-Tb/HIV positive and negative sputum samples were collated. This paved the way for the data analysis. However, since extinction coefficient "*k*", absorption coefficient "α" and dielectric constant "ε" are obtained as functions of wavelength λ, an integration of

Eq. (18) will give a more accurate value. The data on absorbance obtained as a function of wavelength are plotted on figs 5, 6, 7, 8, and 9.

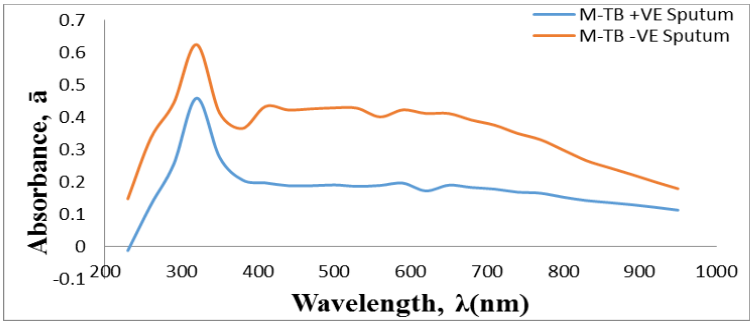

Figure.5: Variation of Average Absorbance, $\bar{a}$ with Wavelength, λ for Twenty Samples of M-Tb Infected and Uninfected Sputum

Figure 5 shows a peak absorbance value of greater than 0.60 and 0.45 for M-Tb negative and positive sputum respectively were recorded at wavelength of 320nm. This peak value falls within the visible range of ultraviolet radiation which is between 300 – 600nm. This is important as a reference point in the study of the infection mechanism and may be of importance in determining the critical Hamaker coefficient that favours repulsion between the bacterium and the macrophage. It could be well-known that the infected M-Tb sputum has lower absorbance values than the uninfected ones.

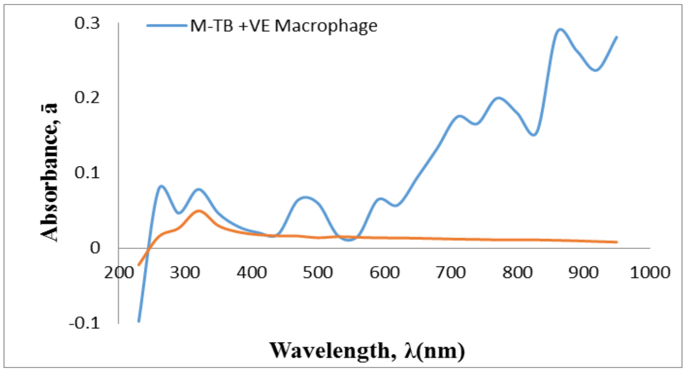

Figure.6: Variation of Average Absorbance, $\bar{a}$ with Wavelength, λ for Twenty Samples of M-Tb Infected and Uninfected Macrophage

Figure 6 shows a peak absorbance value of greater than 0.07 and 0.04 for M-Tb positive and negative macrophages respectively were recorded at wavelength of 320nm which corresponds exactly with that of the figure 5. It is interesting though, that at the lower wavelength of 230nm some negative absorbance values were recorded. The absorbance values of both the M-Tb positive and negative Macrophages were increasing with increase in wavelength. This is the opposite of the result obtained with the M-Tb sputum samples. This may be explained away by the fact of a higher energy level of these cells. The M-Tb infected macrophages gave higher absorbance values than the M-Tb uninfected macrophages. This is a clear indication that infection had occurred and shows the alteration in absorbance values due to M-Tb infection.

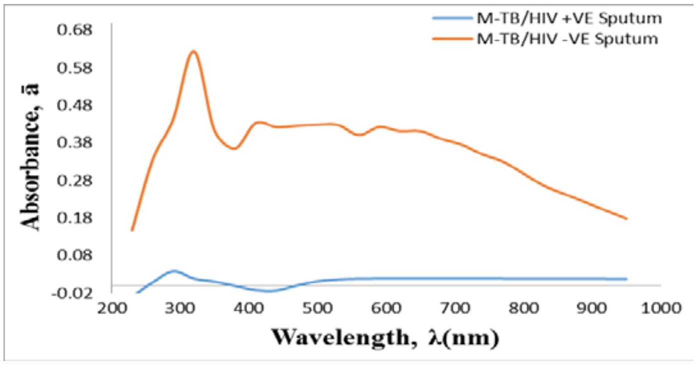

Figure.7: Variation of Average Absorbance, $\bar{a}$ with Wavelength, λ for Twenty Samples of M-Tb/HIV Co-infected and M-Tb/HIV Uninfected Sputum

Figure 7 reveals an interesting pattern for both M-Tb/HIV positive and negative sputum. The absorbance of the M-Tb/HIV co-infected sputum samples systematically increased as the wavelength increased until a critical wavelength of 290nm, where peak absorbance values of greater than 0.60 and 0.06 for M-Tb/HIV negative and positive sputum respectively were accomplished. The trend here shows that the uninfected sputum reveals higher absorbance values at all wavelengths. This indicates that a shift in the energy equation of the system is tenable by some alteration to the sputum as an intervening medium in the M-Tb/HIV – Macrophage interaction. It then suggests a possibility of attaining repulsion between the M-Tb/HIV and the Macrophage cells by some additives to the sputum.

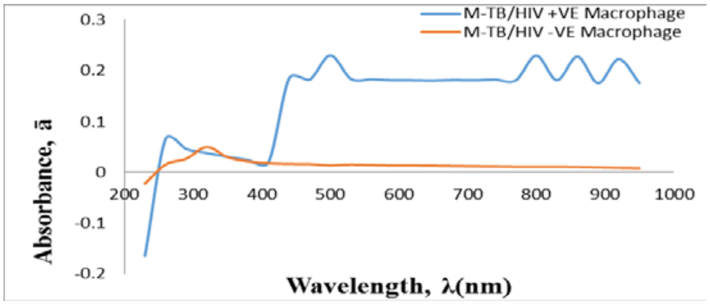

Figure.8: Variation of Average Absorbance, $\bar{a}$ with Wavelength, λ for Twenty Samples of M-Tb/HIV Co-infected and Uninfected Macrophage

Figure 8 followed similar pattern as that of Fig.6 for uninfected macrophage with the peak values occurring at the wavelength of 320nm. The absorbance values of the M-Tb/HIV positive Macrophages were increasing with increase in wavelength. This is the opposite of the result obtained with the sputum. The M-Tb/HIV coinfected macrophages also gave higher absorbance values than the uninfected ones at wavelengths greater than 400nm. This may be explained away by the fact of a higher energy level of these cells. This is a clear indicator that bacteria ingestion had occurred and shows the alteration in absorbance values due to M-Tb/HIV infection.

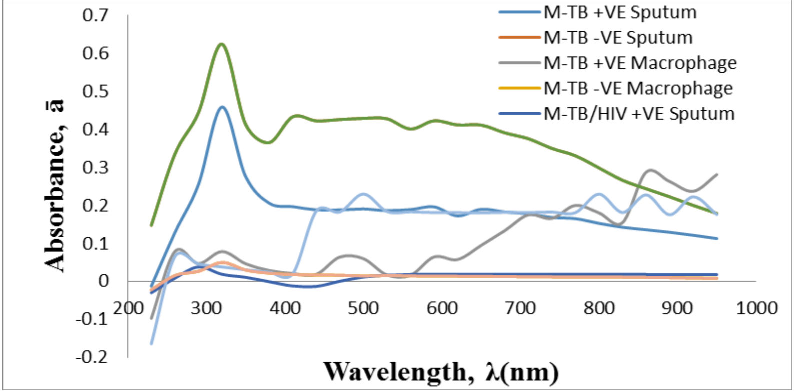

Figure 9: Variation of Average Absorbance, $\bar{a}$ with Wavelength, λ for M-Tb, M-Tb/HIV Sputum and M-Tb, M-Tb/HIV Macrophages

Figure 9 reveals the disparity between the peak absorbance values of M-Tb/HIV positive and negative sputum samples respectively, and this shows an indication of how the bacteria affect the properties of sputum.

Eq.(21) was used to obtain for each interacting system, $A_{ij}\ (A_{11}, A_{22}, A_{33}, A_{12}, A_{13}, A_{23})$ by approximate change of variables. MatLab computation tools were used. This involved the numerical integration of Eq.(21) for each wavelength from 230 to 950 for all the twenty samples in each category. Applying Lifshitz derivation for van der Waals forces as in Eq.(18), The absolute value for the Hamaker coefficient could be derived by obtaining the mean of all the A_{132}, A_{131}, and A_{232} values got from the Lifshitz relation.

Table 1: Values of the Hamaker Constants and Hamaker Coefficients for the Infected and Uninfected M-TB Sputum Samples

Variable ($\times10^{-21}$ Joule)	Infected Sputum		Uninfected Sputum	
	Peak Value	Absolute Value	Peak Value	Absolute Value
A_{11}	---	---	1.1328	0.94188
A_{22}	1.2134	0.96068	---	---
A_{33}	0.4205	0.23067	0.6701	0.42470
A_{132}	0.5187	0.21631	---	---
A_{131}	---	---	0.2241	0.10165
A_{232}	0.6298	0.24986	---	---

Table 1 shows the comparison of the Hamaker constants and coefficients for the positive and negative sputum samples. A_{11} is Hamaker constant for the uninfected sputum samples. A_{22} is the Hamaker constant for the M-Tb, here represented by the infected macrophage. This is as a result of no known process of isolation of the M-Tb at the moment. This is a very close approximation for the bacteria owing to the manner of the infection mechanism. The Hamaker constants A_{33} for the sputum show greater values for the uninfected samples which regularly indicate a higher surface energy than the infected samples. The higher absolute values of A_{132} and A_{232} as against that of A_{131}, as well as the lower value of the absolute combined Hamaker coefficient A_{131abs} for the uninfected samples is a clear suggestion of the relevance of the concept of Hamaker coefficient in the M-Tb infection process. The surface energy A_{131} of the macrophages is less than the surface energy A_{232} of the bacteria (M-Tb).

Table 2: Values of the Hamaker Constants and Hamaker Coefficients for the Infected and Uninfected M-TB/HIV Sputum Samples

Variable ($\times10^{-21}$ Joule)	Infected Sputum		Uninfected Sputum	
	Peak Value	Absolute Value	Peak Value	Absolute Value
$\tilde{A}_{11}$	---	---	1.1328	0.94188
$\tilde{A}_{22}$	1.0267	0.97862	---	---
$\tilde{A}_{33}$	0.5962	0.28812	0.6701	0.42470
$\tilde{A}_{132}$	0.4253	0.18825	---	---
$\tilde{A}_{131}$	---	---	0.2241	0.10165
$\tilde{A}_{232}$	0.5014	0.20474	---	---

Comparing tables 1 and 2; A_{33}, which serves as the energy of sputum as an intervening medium, is seen in M-Tb data to be reduced by infection from 0.4247 $\times10^{-21}$J to 0.23067 $\times10^{-21}$J by a factor of about 45.7% (see table 1). In M-Tb/HIV co-infection, the reduction is from 0.4247 $\times10^{-21}$J to 0.28812 $\times10^{-21}$J, a factor of about 32.2% (see table 2). The reduction is lower in M-Tb/HIV co-infection probably because of the interaction between HIV and Tb. For the combined Hamaker coefficient, the value is 0.21631 $\times10^{-21}$J for M-Tb and 0.18825 $\times10^{-21}$J for M-Tb/HIV. This result is as expected. HIV has the tendency to reduce the energy on the surface of a given material, in this case by about 13%, conforming adverse effects observed in HIV patients with tuberculosis. Note that the values of A_{132} are all positive showing that attraction exists between the macrophage and the M-Tb particles. The effect of the infection can only be abated if a drug, in the form of additive is added that can change the value of A_{132} to negative under that condition, mutual repulsion will occur and it will be expected that, in principle, the Tb bacteria will not attack the macrophage.

4 Conclusion

This research predicts the interaction that occurs between M-Tb/HIV co-infections and macrophages. This prediction was based on the concept of van der waals attractive forces and absolute Hmaker coefficient whose positive values indicate attraction. The positive values of the absolute combined Hamaker coefficients $A_{132}=0.21631\times10^{-21}$Joule and $\tilde{A}_{132} = 0.18825\times10^{-21}$Joule obtained for both the M-Tb and M-Tb/HIV positive samples respectively, are a confirmation that the sputum samples were actually infected. The absolute Hamaker coefficient $A_{131}=0.10165\times10^{-21}$Joule gives the interaction energy among the macrophage cells in the sputum while A_{232} is the interaction energy among the Tb particles in the sputum. A_{232} for M-Tb/HIV co-infection is less than that for M-Tb alone. Reduction in energy in the presence of HIV confirms the adverse effect when Tb and HIV occur simultaneously in a patient. Reduction in energy leads to reduction in macrophage cells in M-Tb/HIV patient and hence greater prospect for death. This is so since a positive Hamaker value for any interacting system implies an attraction between the interacting bodies or particles.

This work concludes that there is a prospect of finding remedy for the M-Tb/HIV pandemic since the desired outcome is that the bacteria do not adhere to the macrophage to avoid penetration, in which case a condition for rendering combined Hamaker coefficient negative is required. Thus, a condition was sought for repulsion to occur and that condition will be based on the value of A_{33} that would render the absolute combined Hamaker coefficient A_{132abs} negative. To achieve the condition of A_{33} above, possible additive(s) to the system (in form of drugs) to the sputum as intervening medium should be required. That, as expected, may be the much desired way out for drug resistant strains of the M-Tb bacteria.

REFERENCES

[1] Adeeb S., Gauhar R., Mazhar U., Waleed AK, Young SL., (2013). Challenges in the development of drugs for the treatment of tuberculosis. *The Brazilian journal of infectious diseases,* 17(1): 74 – 81.

[2] Charles, Kittel, (1996): Introduction to Solid state Physics, 7th Ed., John Willey and sons Inc. New York. 308.

[3] Chukwuneke J.L., Achebe C.H., Omenyi S.N. (2015). Mycobacterium Tuberculosis (M-TB)-Human Sputum Interaction Mechanisms Energetics. International Journal of Biological Engineering, 5(2): 23 – 30.

[4] Corbett El, Marston B. et al., (2006). Tuberculosis in Sub-Sahara Africa: opportunities, challenges and changes in the era of antiretroviral treatment. *Lancert,* 367: 926 – 937.

[5] De Souza M. V. N., (2006). Recent patents on Anti-infective. *Drug Discovery*, 1: 33 – 34.

[6] Gonzalez-Juarrero M., Turner O. C., Turner J., Marietta P., Brooks J. V., Orme I. M., (2001). Temporal and Spatial arrangement of lymphocytes within lung granulomas induced by aerosol infection with mycobacterium tuberculosis. *Infect. Immun.* 69: 1722 – 1728.

[7] Hamaker, H.C., (1937). The London – Van der Waals attraction between spherical Particles. *Physica,* 4: 1058.

[8] Hough D. H and White L. R., (1987). Adv Colloid Interface. *Sci*ence, 28: 35.

[9] Lifshitz E. M., (1961). The Theory of Molecular Attractive Forces between Solids. *Advanced Physics.* 10: 165 – 209.

[10] Maartens G., Wilkinson R. J., (2007). Tuberculosis. *Lancert,* 370: 2030 – 2043.

[11] Nunes J. E. S., Ducati R. G., Breda A., Rosado L. A., De Souza B. M., Palma M. S., Santos D. S., Basso L. A., (2011). Molecular, kinetic Thermodynamic and Structural analysis of mycobacterium tuberculosis hisD-encoded metal-dependent dimeric histidinol dehydrogenase (EC1.1.1.23). *Archives Biochemistry and Biophysics,* 512: 143 – 153.

[12] Nunn P., Willianms B. et al., (2005). Tuberculosis control in the era of HIV. *Nat. Rev. Immunology,* 5(10): 819 – 826.

[13] Robinson, T.S., (1952). Optical Constants by Reflection. Proceedings of the Physical Society London 65(11): B910

[14] Visser, J., (1981). Advances in Interface Science, *Elsevier Scientific Publishing Company, Amsterdam,* 15: 157–169.

[15] World Health Organization (WHO), (2005). Tuberculosis, WHO Information: Fact Sheets. http://www.who.int/mediacentre/factsheets/fs104/en/index. html, Retrieved 24-11-13.

[16] World Health Organization (WHO), (2012). Global tuberculosis report 2012. Geneva, Switzerland. http://www.who.int/tb/publications/global_report/, Retrieved 24-11-13.

[17] World Health Organization (WHO), (2009). Global tuberculosis Control: Epidemiology, strategy, financing, WHO report 2009, Geneva, Switzerland, WHO/HTM/TB/2009.411.

SOCIETY FOR SCIENCE AND EDUCATION
UNITED KINGDOM

JBEMi JOURNAL OF BIOMEDICAL
ENGINEERING AND MEDICAL IMAGING

ISSN: 2055-1266
VOLUME 2 ISSUE 6

Correlation between Different Erythrocytes Sedimentation Rates and Bio Impedances Surface Acoustic Wave

Mohamed A. A. Eldosoky
Dept of Biomedical Engineering- Helwan university, Egypt
hm1_eldosoky@hotmail.com, mohamed_eldesouky@h-eng.helwan.edu.eg

ABSTRACT

RBCs with their shapes, volumes and concentrations are very important indicators for the normal and abnormal healthy body. Plasma had electrical characteristics different from the red blood cells. Consequently, the impedance of the plasma- RBCs is proportional to the number or the volume of the RBCs with the plasma. This paper had presented new proposed method for classification of the RBCs by using surface acoustic wave and the bioimpedance so it can be called bioimpedance surface acoustic wave.

Keywords: Bioimpendance, Erythrocytes Sedimentation Rate, RBCs, Surface acoustic wave.

1 Introduction

Blood is the vital liquid in the human body. The major part of it with more 99% is called RBCs. Any variation in the shape or the volume or the number of them in the blood is inherent with not only the blood diseases but also the human organs. Due to the difference in the electrical characteristics between the RBCs and the plasma (the RBCs have conductivity with lower values than the plasma), the impedance of RBCs-plasma is related to the blood cell concentrations and volumes [1].

Recent researchers had proposed mathematical models including the relations between the permittivity and the volume fraction regardless the number and the volume of the cells [2]. These investigations also had proved that the electrical polarization formula of the cells is the milestone parameter for estimating the electrical characteristics of the plasma-RBCs solution [3].

In [4], the researchers had tried to estimate the impedance of the solution as a tool for determining the solutions' concentration at three different frequencies for determining the parameters of the equivalent circuit of the cell.

The applications of bioimpedance for detecting the blood diseases are numerous. These applications had depended on determining the variation of the electrical blood characteristics as compared to the normal cases [5,6,7,8]. Microcytes and macrocytes are two phenomena as examples of the volume variations and so the impedances of the RBCs that are referred to certain diseases or drinking alcohol or wines [9].

DOI: 10.14738/jbemi.26.1711
Publication Date: 21th December 2015
URL: http://dx.doi.org/10.14738/jbemi. 26.1711

This paper presents a model that can be used for diagnosing the variations in the erythrocytes sedimentation rate (ESR) and classifying the shapes, the volumes and the volume fractions of the RBCs. These are the main parameters related to the RBCs beside the hemoglobin as in the CBC lab test. This process had been done by using the surface acoustic wave (SAW) as known with its sensitivity to the electrical properties of the medium solution. Depending on the phenomena of Erythrocytes sedimentation rate (ESR), during the time progressing the concentration of the RBCs within the blood samples changes along the blood sample so does the electrical impedance that can detected by using SAW. This model had proved the SAW's ability to classify the RBCs with different volumes not volume fractions only.

2 Mathematical Model

For the plasma-RBCs solution with volume fraction, Φ, number of particles, *N* as a volume of each particle, V_p, the permittivity and the conductivity of this solution was calculated by the following equations [3]:

$$\varepsilon(\omega) = \varepsilon(\infty) + \frac{\varepsilon(0)-\varepsilon(\infty)}{1+j\omega\tau} \tag{1}$$

Where $\varepsilon(\infty)$ and $\varepsilon(0)$ are the dielectric constants at infinity and zero frequencies, respectively. τ is called the relaxation time for the particle as function of its size, volume fraction, rigidity of the particle.

The volume fraction of any solution is calculated by:

$$\Phi = \frac{N * Vp}{V} \tag{2}$$

The general formulation for the effective permittivity ($\varepsilon(\infty) or \varepsilon^*$) for any cell structure as a function of the volume fraction was calculated as shown [10]:

$$\varepsilon * = \varepsilon_a * + \frac{\Phi \varepsilon_a *}{3} \sum_{k=x,y,z} \frac{(\varepsilon_p * - \varepsilon_a *)}{\varepsilon_a * + A_k(\varepsilon_p * - \varepsilon_a *)} \tag{3}$$

A_k is the axial polarization factor of the cell as function of its shape [10].

$\varepsilon^*{}_s$ and $\varepsilon^*{}_p$ are the equivalent permittivity of the plasma and the cell only, respectively.

As shown the last equations had studied the influence of the RBCs through the effect of the volume fraction of the cells without focusing on the effect of the number and their volumes individually.

In this paper new proposed model had been presented. This model had detected the ESR of various kinds of RBCs by using the bioimpenace surface acoustic wave. Surface acoustic wave (SAW) is an acoustic wave generated by using transducers called interdigital transducers (IDTs). The generated wave has two components, which are mechanical and electrical. SAW has its ability to detect the medium characteristics depending on its electrical characteristics. As comparing the transmitted signal on the medium with the received one, the variation in the transmitted signal is related to the medium characteristics. This variation is called the wave's perturbation, which is classified as frequency (velocity) perturbation and amplitude perturbation. The applications of the SAW as a bioimpedance tool were numerous [11]. The associated equations for the time-frequency perturbation was derived in [12]:

$$\frac{\Delta f}{f}(t) = \frac{\Delta v}{v}(t) = -\frac{K^2}{2} * \frac{(\frac{\sigma(t)}{\omega})^2 + \varepsilon_0(\varepsilon(t) - \varepsilon_r)(\varepsilon(t)\varepsilon_0 + \varepsilon_p)}{(\frac{\sigma(t)}{\omega})^2 + (\varepsilon(t)\varepsilon_0 + \varepsilon_p)^2} \quad (4)$$

Where $\frac{\Delta v}{v}$ and $\frac{\Delta f}{f}$ are the velocity and frequency shifts, respectively in the received signal as compared to the input or transmitted one. ε_r is the reference solution (the plasma-RBCs). ω is angular frequency, K^2 is the mechanical coupling. ε_p is the dielectric constants of the substrate and ε_0 is the dielectric constant of the free space.

From this equation we can deduce that the response of this SAW is a signal with shifted frequency with Δf but this shifted varies with time, where the during the sedimentation process, the RBCs will separate from the plasma. So two solutions will be formed in the top of the sedimentation tube, which are RBCs-plasma with subscript 1 and plasma solution with subscript 2 as shown in Fig.1. So at any time, the total conductivity $\sigma(t)$ of the solution under the IDT was calculated by:

$$\sigma(t) = \sigma_1\left(\frac{l}{L_1}\right) + \sigma_2\left(\frac{L_1 - l}{L_1}\right) \quad (5)$$

Also the equation of the total dielectric constant of the solution under the IDT, $\varepsilon(t)$ was given by:

$$\varepsilon(t) = \varepsilon_1\left(\frac{l}{L_1}\right) + \varepsilon_2\left(\frac{L_1 - l}{L_1}\right) \quad (6)$$

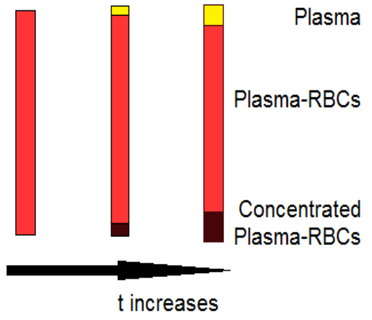

(a)

Figure.1 a) The sedimentation process and formation of three different solutions

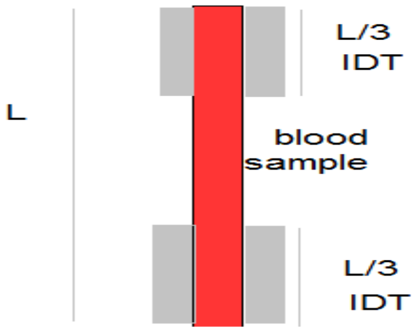

(b)

Figure.1 b) SAW with blood sample

As shown in Fig.1a, at the top of the tube during the sedimentation process the RBCs will separate from the plasma. So three liquids will be formed, which are the plasma (top) and the RBCs-plasma (medium) with normal concentration and RBCs-plasma with higher concentration (bottom), respectively. With the progress of the time, the heights of these two liquids vary from time to another. The time rates of changing for the heights are related to the sedimentation velocity, where higher velocity means high rates of these lengths or heights. The sedimentation velocity of the RBCs as function of their radii and the volume fractions was given by [13]

$$v = (\rho_{RBC} - \rho_{plas}) * g * d^2 / 18\mu(1 + 2.5\Phi) \quad (7)$$

ρ_{RBC} and ρ_{plas} are the densities of the RBCs and plasma, respectively. d is the RBC radius, and μ is the viscosity of the free plasma. g is the acceleration of gravity.

According to the mechanism of the sedimentation process, three sections will be formed (upper medium and lower). So it was assumed that the length of sample is L and assume that this length is divided to three divisions each has length, L/3. The first and the third divisions are under the IDTs of the SAW as shown in Fig1b.

Fig.2 is the flowchart that explain the mechanism of the bioimpedance by using SAW. The problem here is that all parameters in this flowchart aren't constants, where the velocity of the sedimentation is function of the volume and the volume fraction (Eqn.7). The electrical impedance of the medium under the interdigital transducers (IDTs) is related to the permittivity and the conductivity that change with the time. But these electrical parameters depend also on the volume fraction and the polarization factors of the cells beside that they are frequency dependent of the used SAW signal. This process stops when the plasma solution fills the tube under the IDT ($l=L_1=L/3$).

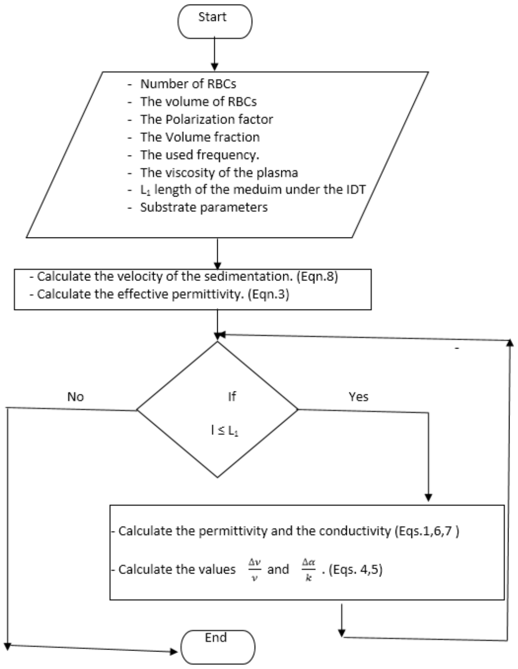

Figure 2: The flowchart of the proposed model

3 Results

As mentioned before this model deals with the mechanical and the electrical properties of the RBCs in the plasma solution. So this section had discussed the relation between the ESR of the RBCs and their bioimpedances by using the SAW at different cases. These cases are related to the diseases affect the formation either the volume or the number of the RBCs. The influence of the drugs or the alcohol was presented also.

3.1 RBCs with the same volumes but with different volume fractions

Figure 3 shows the response of the RBCs-plasma solution with different volume fractions. Four different responses for four different values of volume fractions with the same cells volume as common.

Consequently, different responses will be expected but parallel to each other as indicator that the volumes' cells are equal.

(If the response is parallel to the response of the normal curves it means equal volumes' cells but different in volume fractions)

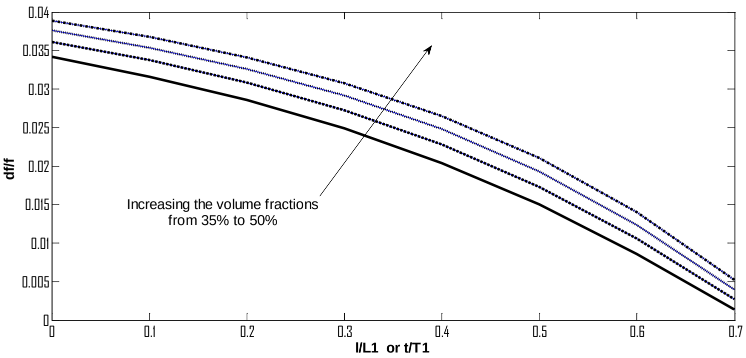

Figure 3.The responses of the RBCs for the same volumes at different volume fractions (0.35, 0.40. 0.45, 0.50)

3.2 RBCs with the same volume fractions but with different cells' volumes

Here lower and higher volumes are the main properties of the Microcytes and macrocytes cells, respectively. As shown the cell's volume is the main parameter that controls the sedimentation velocity. Since the volume fractions are the same, the starting point or the starting impedance is the same. But as changing the time the variation in the impedance depends on the sedimentation velocity that depends on the cells velocity. Higher volumes cells have faster responses than the lower as shown in Fig.4.

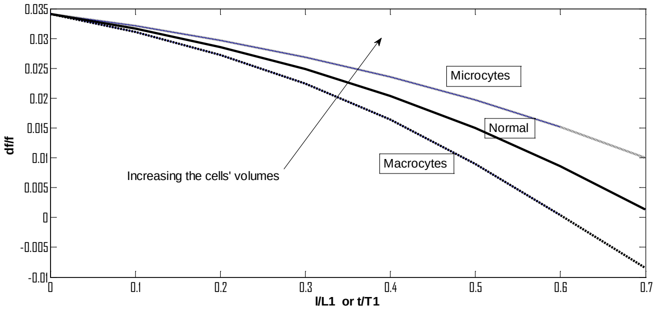

Figure 4 Responses of microcytes and macrocytes as compared to the normal volume of RBCs

3.3 Influence of alcohol on the RBCs formation

Alcohol and wines have an effect not only the RBCs but also on the body organs. The blood with its RBCs are the most effective part. Lake in the number of the RBCs is associated with drinking alcohol due to the problems inherit with the production of RBCs. So as a compensation of this problem an increment in the volume had been shown clearly [14]. Fig.5 shows the response of this model as the raw collected data had been applied. The variation here in both the volume and the number of the RBCs. The variation in both the volumes and the radius is about +0.08 and -0.07, respectively as compared to the normal values.

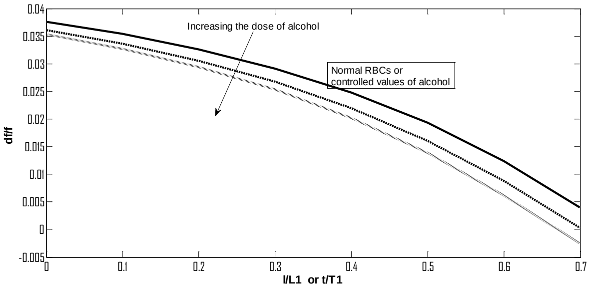

Figure 5. The third application: detection of the RBCs for the alcohol drinkers

4 Conclusion

Surface acoustic wave with its characteristics is a complete bioimpedance system depending on its sensitivity for any variation within any solution. The electrical properties of the RBCs as compared to the plasma was the main point that this model had built on. With the aiding of the mechanical characteristics of the RBCs summarized in the ESR, this model had proved its ability to classify the RBCs and will be a good tool for studying the blood characteristics. In the future, with the aiding of any classification technique as ANFIS, complete blood analysis may be proposed for studying not only the RBCs but also all blood components.

REFERENCES

[1] M. O. Grimnes S., “Bioimpedance and bioelectricity basic”, Academic Press, New York, 2000.

[2] Koji Asami and Takeshi Yonezawa., " Dielectric Behavior of Wild-Type Yeast and Vacuole-Deficient Mutant Over a Frequency Range of 10 kHz to 10 GHz" , Biophysical Journal Volume 71 October 1996.

[3] 1rjan G. Martinsen, Sverre Grimnes, and Herman P. Schwan, " Interface Phenomena And Dielectric Properties Of Biological Tissue" Encyclopedia of Surface and Colloid Science , 2002.

[4] Rangadhar Pradhan, Analava Mitra, Soumen Das "Impedimetric characterization of human blood using three-electrode based ECIS devices", J Electr Bioimp, vol. 3, 2012.

[5] Quazi D. Hossain1 and Sagar K. Dhar1,"Characterization of Physiological Glucose Concentration Using Electrical Impedance Spectroscopy", IJCSI International Journal of Computer Science Issues, Vol. 10, Issue 1, No 1, January 2013.

[6] Aleksey Ni1, Taqi Ahmad Cheema2, and Cheol Woo Park1," Numerical Study of RBC Motion and Deformation through Microcapillary in Alcohol Plasma Solution", Open Journal of Fluid Dynamics, Vol.5, 2015.

[7] Godfrey S. Bbosa1, David B. Kyegombe, William W. Anokbonggo, Aloysius Lubega, Apollo Mugisha, and Jasper Ogwal-Okeng." Effect of chronic alcohol consumption on the red blood cell count and RBC indices in the HIV infected patients on d4T/3TC/NVP drug regimen in Uganda", International Journal of Basic & Clinical Pharmacology | | Vol 2 Issue 5. September-October 2013.

[8] Jaime Punter-Villagrasa, Joan Cid, Cristina Páez-Avilés , Ivón Rodríguez-Villarreal, Esteve Juanola-Feliu, Jordi Colomer-Farrarons and Pere L. Miribel-Català," An Instantaneous Low-Cost Point-of-Care Anemia Detection Device", Sensors Vol 15, 2015.

[9] Mohamed. A. A. EL-Dosoky." Electrical characteristics of RBCs at different blood diseases", accepted for publication in clinical Engineering journal, schedule for publication in vol 40, Issue 40, October/December 2015.

[10] V. Raicu a, T. Saibara b, H. Enzan c, A. Irimajiri., "Dielectric properties of rat liver in vivo: analysis by algorithm hepatocytes in the tissue architecture", Bioelectrochemistry and Bioenergetics Vol 47,1998..

[11] Shaimaa. Tarek. El Zarie, and Mohamed. A. A. EL-Dosoky," Diagnosis of Blood Diseases Using Shear Horizontal Surface Acoustic Waves", 30th NATIONAL RADIO SCIENCE CONFERENCE (NRSC 2013), National Telecommunication Institute, Egypt, April 16-18, 2013.

[12] Mohamed. A. A. El-Dosoky, "Simulation of the Interaction between Liquids and the Shear Horizontal Surface Acoustic Wave (SH-SA W)", 26th National Radio Science Conference (NRSC), Cairo, Egypt, 2009.

[13] Rovshan M Ismailov, Nikolai A Shevchuk and Higmat Khusanov," Mathematical model describing erythrocyte sedimentation rate. Implications for blood viscosity changes in traumatic shock and crush syndrome", *BioMedical Engineering OnLine.vol* 4:24, 2005

[14] Godfrey S. Bbosa1, David B. Kyegombe, William W. Anokbonggo, Aloysius Lubega, Apollo Mugisha, and Jasper Ogwal-Okeng." Effect of chronic alcohol consumption on the red blood cell count and RBC indices in the HIV infected patients on d4T/3TC/NVP drug regimen in Uganda",International Journal of Basic & Clinical Pharmacology. Vol 2 .Issue 5, September-October 2013.

SOCIETY FOR SCIENCE AND EDUCATION
UNITED KINGDOM

JBEMi JOURNAL OF BIOMEDICAL ENGINEERING AND MEDICAL IMAGING

ISSN: 2055-1266
VOLUME 2 ISSUE 6

Temporal Based EEG Signals Classification for Talocrural and Knee Joint Movements using Emotive Head Set

Anjum Naeem Malik[1], **Javaid Iqbal**[2] **and Mohsin I. Tiwana**
National University of Sciences & Technology, Islamabad, Pakistan
[1]anjum.naeem78@mts.ceme.edu.pk ; [2]j.iqbal@ceme.nust.edu.pk

ABSTRACT

Recent developments in Brain Computer Interfacing (BCI) and neuroprosthetics have played a vital role for disable people to expect better life quality. In this contribution Electroencephalographic (EEG) signals acquired from six healthy test subjects, are used for the offline analysis of BCI through classification of four lower limb movements including talocrural (ankle) joint dorsi-planter flexion and knee joint extension-flexion. Fourteen channel Emotive EPOC head set is used to acquire EEG signals from sensorimotor cortex area of brain, using a particular data acquisition timeline protocol. Features are extracted in time domain from raw EEG data. Power spectral density, variance, mean value and kurtosis features are applied on raw EEG signals. Multiple classification algorithms are implemented for discrimination of four lower limb movements within data set. The paper uses Quadratic discriminant analysis, Naïve Bayes and Support vector machine classifiers to stratify the movement intent of lower limb. Maximum classification accuracies achieved through various classifiers are; 86.35% with average band power & QDA, 84.38% with mean value & QDA and 78.13% with power spectral density & Quadratic-SVM. The presented findings are optimistic in making the path easier towards the development of BCIs with rich EEG based control signals using noninvasive technology.

Keywords: kurtosis, Quadratic Discriminant Analysis, Naïve Bayes, Support Vector Machine.

1 Introduction

BCI technologies decode signals acquired from brain activities in order to translate the human intentions into useful readable commands to control external devices like prosthetics or computer applications. It provide an alternative opportunity to people suffering from severe diseases causing paralysis and motor disabilities. It is an emerging technique nowadays and provide a communication facility to control and actuate devices using brain signals [1]. Various techniques have been adopted to extract signals from brain which includes magneto electroencephalography (MEG), Functional magnetic resonance imaging

---

[1] The research work is supported by Department of Mechatronics Engineering (College of Electrical & Mechanical Engineering) National University of Sciences and Technology Pakistan. This contribution is borne under the supervision of Dr. Javaid Iqbal and Dr. Mohsin I. Tiwana. This publication only exhibits the author's views.

DOI: 10.14738/jbemi.26.1730
Publication Date: 27th December 2015
URL: http://dx.doi.org/10.14738/jbemi. 26.1730

(fMRI), near infrared spectroscopy (NIRS), electrocarticogram (ECoG) and electroencephalography (EEG) [1] & [2]. Among these aforementioned techniques signals acquisition using EEG is a rapid infusion in BCI since it reflects the electrical responses of human brain in actions and it is widely used because of its noninvasiveness, higher temporal resolution, Inexpensiveness, and no exposure to radiations.

In this contribution EEG data is collected from brain using EMOTIV Headset [13] with fourteen channel electrodes. The main benefit of using emotive headset is that it provides better portability along with providing a noninvasive medium for collection of EEG data. According to a survey majority of the cases of strokes or brain injuries causes disability of people and this type of disability can be addressed either by providing a prosthetic device or by restoring the motor function of such disable patients [6]. Nowadays with the advancements in the field of biomedical engineering, evoked potential recorded from brain combining with the robotic feedback is used to help people with disabilities. Some of the most recent and important research applications of BCI are human to human interface, control of a prosthetic robotic arm, exoskeleton control, mobile and guided robotics [4].

In this paper, classification of offline EEG data signals for lower limb joints movements is presented in which two knee movements (extension & flexion) and two talocrural (ankle) movements (dorsiflexion & plantarflexion) are included. According to literature review most of the work on EEG signals classification is carried out on distinguishing the movements of upper limbs which includes carpus, ante brachium, fingers and hand gestures whereas for lower limb movements higher number of electrodes are required to record the evoke potential from the scalp of the brain, as the signals are quite weak and noisy. Table 1 shows brief survey of bunch of the classification & features extraction techniques which have been implemented to classify different lower limb movements.

Table 1: Literature Review

Authors/References	No. of Electrodes	Classification Algorithm	Features Acquired	Accuracy
Josheph T. GWin, Daniel P Farris [4]	264 Channel	Naïve Bayes	Independent Components Analysis	80%
Kaiyang Li, Xiaodong Zhang, Yuhuan Du [14]	16 Channel	Support Vector Machine	Wavelet Transform	78.9%
Presacco A, Goodman R, Forrester L [9]	60 Channel	Linear Weiner Filter	Power Spectral Density	75%
Hosni S.M, Ain Shams Univ, Cairo [16]	16 Channel	Radial Basis Function Support Vector Machine	Auto Regressive, Band Power, PSD	70%
Fathy A, Elhelw M, Eldawlatly S [19]	14 Channel	Linear Discriminant Analysis	Principal Components Analysis	73%

This paper focuses on the Electroencephalographic signals (EEG) acquisition through noninvasive method in which Emotiv headset equipped with 14 active electrodes is used to collect EEG data from test subject. Data is recorded individually for four movements of lower limb for predefined period of time, according to data acquisition protocol. Once the EEG data is recorded, sixth order Butterworth filter is applied for removal of noise and undesirable artifacts from the data set. Further this paper uses multiple feature extraction techniques to figure out the prominent features and supervised learning classification algorithms to stratify lower limb movements including knee joint extension & flexion and talocrural joint dorsiflexion & plantarflexion.

2 Methodology and Data Acquisition

An experimental protocol for data acquisition is designed for offline analysis of the time series EEG data. Six volunteers (3 males & 3 females) age between 21 to 30 years participated in the data acquisition experimentation without any prior training of the experimental procedure. All test subjects are physically healthy and neurologically stable. Data acquisition is carried out in noiseless room with subjects sitting comfortably in a chair with arms rested on sides. The subjects performed the movements shown on a computer screen in the form of a video in which a person is performing lower limb movements (knee joint extension, knee joint flexion, talocrural joint dorsiflexion and talocrural joint plantarflexion). The test subjects are instructed to avoid any eye blinking, facial expressions in order to minimize unnecessary artifacts while performing the limb movements. Twenty five trials of each type of movement with 1000 data points in 9.50 seconds are acquired from each subject. Figure 1 shows the block diagram of whole process.

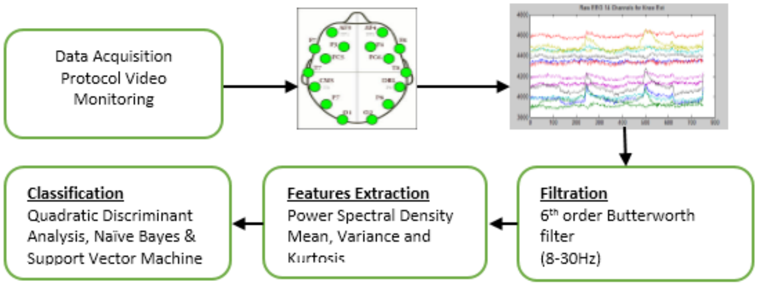

Figure 1: Block Diagram of Brain Computer Interface System

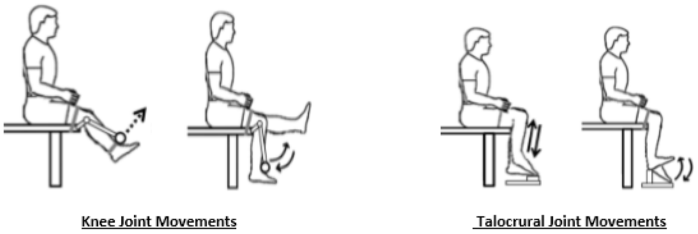

Figure 2: Lower Limb Movements

EEG signals recorded in this paper are based on the international 10-20 system [13] which are AF3, F7, F3, FC5, T7, P7, O1, O2, P8, T8, FC6, F4, F8, and AF4 respectively. Signals were recorded at 128 Hz sampling rate and they are spontaneous signals as these signals have rhythmicity. It can be divided into different frequency bands out of which alpha (8-13Hz) and beta (14-30Hz) frequency bands [14] are more dominant during the state of consciousness and limbs movements therefore these two bands are filtered by applying Butterworth filter (8-30Hz) for the classification of lower limb movements, as Butterworth filter have smooth pas bands as compared to other types of filters.

Emotiv Headset equipped with 14 active electrodes is used to record visually evoked response from the sensorimotor cortex on the scalp of the brain. Specifications of the Emotiv headset are discussed in below mentioned table 2 [13].

Table 2: EMOTIV Headset Specifications

Number of channels	14 (plus CMS/DRL references)
Channel names (Int. 10-20 locations)	AF3, AF4, F3, F4, F7, F8, FC5, FC6, P7, P8, T7, T8, O1, O2
Sampling method	Sequential sampling, Single ADC
Sampling rate	~128Hz (2048Hz internal)
Resolution	16 bits (14 bits effective) 1 LSB = 1.95μV
Bandwidth	0.2 - 45Hz, digital notch filters at 40Hz and 60Hz
Dynamic range (input referred)	256mVpp
Coupling mode	AC coupled
Connectivity	Proprietary wireless, 2.4GHz band
Battery type	Li-poly
Battery life (typical)	12 hrs
Impedence measurement	Contact quality using patented system

3 Filtration of Acquired EEG Data

Once the data is recorded, band pass filter is applied (8-30Hz) in both forward and reverse direction with sampling frequency of 500Hz. In Brain computer interfacing, the purpose of filtration is to minimize the undesirable artifacts recorded during data acquisition [9]. Most common source of artifacts are physiological artifacts like eye movement and muscles movements [7], where eye movements have frequency of 2-5 Hz which are removed by bandpass filter[10] & [17]. Frequency response of the sixth order Butterworth filter, raw and filtered EEG data is shown in figure 3.

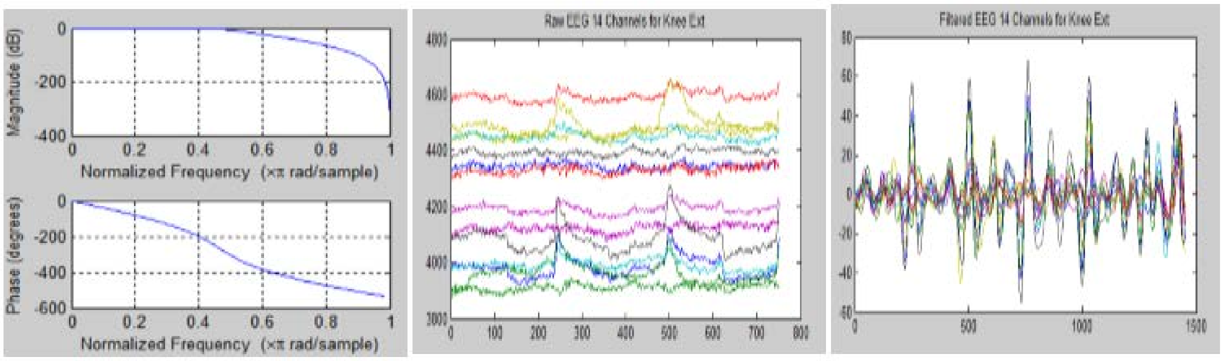

Figure 3: Frequency Response of Band Pass Filter, Raw EEG Acquired Data of 14 Channel, Filtered Data

4 Feature Extraction

Multiple feature extraction techniques are implemented to extract the features from filtered EEG data in time domain [16]. Average band power (PSD) [12] provides us information about the distribution of time series data over different frequencies. It shows the variation of data with respect to different frequencies.

$$Average\ Power_{PSD} = \frac{1}{2\pi}\int_{w1}^{w2} S_{X_w} \cdot dw$$

Where $S_{X_w}$is the power spectral density of the filtered EEG signal ($x_i(t)$) and X_w is Fourier transform of filtered signal$x_i(t)$.

The measurement of spread between the numbers in the observed data set is termed as variance and kurtosis depicts the statistical distribution of observed EEG data around the mean, as EEG data is a nonstationary data and its distribution is purely non Gaussian.

$$Variance = \frac{1}{N-1}\sum_{i=1}^{N}|X_i - \mu|^2$$

Where X_i is a 14 column vector representing the EEG data recorded from 14 electrodes and μ is the mean of individual columns and N is the number of data points.

$$\text{Kurtosis} = \frac{\sum_{i=1}^{N}\frac{(X_i-\bar{X})^4}{N}}{S^4}$$

Where X_i is the observed data, N represents number of points, $\bar{X}$ indicates mean of observed data and S^4 represents the standard deviation. There are multiple techniques available to translate the features from observed data in combine frequency-time domain like Hilbert Transform, Wavelet Transform and Auto Regressive [8] & [17] but these methods increase the complexity of parameters and enhancing the difficulties like overfitting of data during classification. Topographical distribution of feature vectors (average band power) of lower limb movement's data is shown in figure 4. The red area shows convergence of the data over the left hemisphere of frontal lobe of motor cortex.

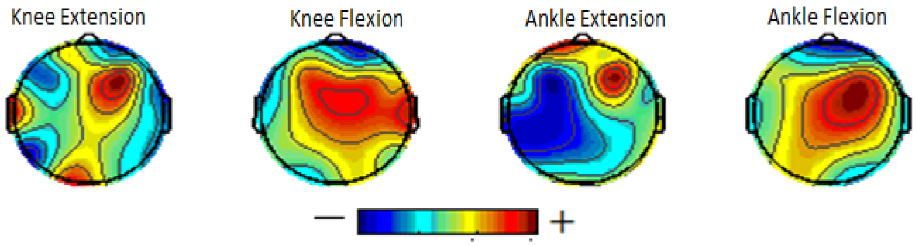

Figure 4: Topoplots of feature vector (Average band power) for knee extension movement, knee flexion movement, Talocrural Dorsiflexion movement and Talocrural Plantarflexion movement

5 Classification Techniques

Once the feature vectors are extracted from filtered EEG data, these feature vectors are classified into four classes representing four types of lower limb movements. This paper used Quadratic Discriminant Analysis (QDA), Naïve Bayes and one to one support vector machine (SVM) [12] & [14] with quadratic kernel. Mathematically QDA can be formulated as;

$$g_{j(x)} = \sum_{i=1}^{4} w_i x_i + w_o + \sum_{i=1}^{4}\sum_{j=1}^{4} w_{ij} x_i x_j$$

where w_i is the weight vector $w.x \propto \in^{-1}(x-\mu)^t(x-\mu)$, w_{io} is the bias threshold/ weight threshold and μ is the average mean. Discriminant analysis assigns objects to one of the several classes depending upon the 14 column feature vector. The classifier is said to assign feature vector x to a class w_i if.

$$g_i(x) > g_j(x) \qquad \text{for all } j \neq i$$

Architectural diagram of the QDA is shown in figure 4.

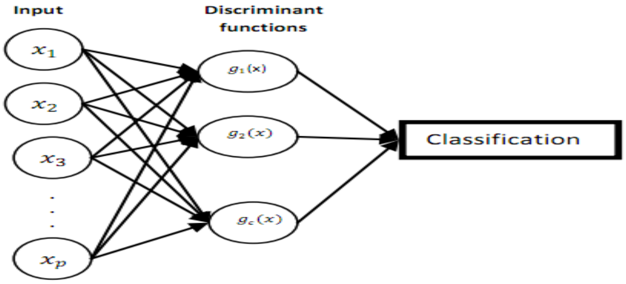

Figure 5: Quadratic Discriminant Analysis Architecture

Naïve Bayes [15] is based on Bayesian Theorem according to which it splits the posterior in terms of prior distribution and likelihood. Bayes classifier assumes that the values of a particular feature of EEG signal is unrelated to the presence or absence of any other feature translation given the class. Mathematical formulation is presented as;

$$P(W|X_1, X_2 \dots\dots\dots X_n) = \frac{P(X_1, X_2 \dots\dots\dots X_n|W)\ x\ P(W)}{P(X_1, X_2 \dots\dots\dots X_n)}$$

where $P(W|X_1, X_2 \dots\dots\dots X_n)$ represents the posterior probability of the class given feature vectors (X1,X2……X14), $P(X_1, X_2 \dots\dots\dots X_n|W)$ represents likelihood of the feature vectors given Class(W1,W2,W3 & W4). $P(W)$Indicates prior probability about the class (0.25 for each class) and $P(F_1, F_2 \dots\dots\dots F_n)$ represents evidence or normalizing factor.

Support vector machine constructs a hyperplane in feature space to classify different classes of data. Nature of hyperplane depends upon the type of kernel function used as in this paper quadratic kernel is implemented to classify EEG data among four classes by drawing a nonlinear hyperplane. Mathematically SVM is represented by following equation [14];

$$y = \sum_i a_i \beta(s_i, x) + b$$

Where S_i is support vector, a_i is weight and b is the bias which is used to classify feature vector x into four classes. Here β represents the kernel function. As stated above quadratic kernel is implemented in this paper and mathematically it can be represented as.

$$\beta(s_i.x) = (s_i.x + r)^2$$

where r is the quadratic function parameter and for the sake of better classification it is selected carefully.

6 Results and Discussion

Classification rates achieved using multiple feature extraction techniques with different classifying algorithms are presented in table 3. Based on the analysis, results obtained and the literature survey, it can be concluded that Quadratic Discriminant Analysis with average band power as feature vector give the best classification accuracy of 86.25% whereas SVM with average band power feature set give 78.13% and Naïve Bayes give 74.38% respectively. Mean, variance and kurtosis as feature set also showed classification accuracy in acceptable range.

Table 3: Percentage Accuracies of Different Classifiers verses Multiple Feature Sets

Classification Algorithm	Average Band power	Mean Value	Variance	Kurtosis
QDA	86.25%	84.38%	83.10%	60.63%
Quadratic SVM	78.30%	65.53%	71.88%	51.26%
Naïve Bayes	74.56%	71.29%	73.75%	53.45%

The research work carried out in this paper has of great importance as one can understand that how specific neural activity differs from the other motor cortex area, as primary motor cortex of brain is organized such that the left side of the primary cortex is responsible for the movements of right side of the body and right side of brain cortex is responsible for movements of left side of the body. Stratified and cross validated results along with the weighted average results of Naïve Bayes and average band power, Kurtosis & Variance as feature set, are presented in table 4.

Table 4: Naïve Bayes Classified Cross Validation, Weighted Average by Class and Relative Error

Naïve Bayes Classifier	Mean Absolute Error	Root Mean Squared Error	Relative Absolute Error	Root Relative Squared Error	Coverage of Cases (0.95 level)	Mean Rel. Region Size	True Positive Weighted Avg.	False Positive Weighted Avg.
Average Band Power	0.1259	0.3378	33.57%	78.01%	78.75%	28.59%	0.750	0.083
Kurtosis	0.2238	0.4326	59.67%	99.90%	71.25%	35.15%	0.550	0.150
Variance	0.1363	0.3552	36.24%	82.02%	\78.125%	28.12%	0.725	0.092

The deviation in results occur due to variation in the size of classes as it increases the misclassification rate and the weighted average of false positives. As shown in table 4, weighted average of false positives in case of average band power is 0.083, in case of kurtosis 0.150 and in case of variance 0.092 whereas weighted average for true positives is 0.750, 0.550 and 0.725 respectively. In this research, a novel combination of feature vectors and classification algorithms has been implemented to decode lower limb movements (knee and talocrural joint extension/flexion) with maximum classification accuracy of 86.25%.

7 Conclusion

This research work is focused on the optimization of classification techniques with multiple set of feature vectors. In this study, the performance of Quadratic discriminant analysis, Naïve Bayes and Support vector machine using average band power, mean value, variance and kurtosis feature vectors for the classification of four lower limb movements has been analyzed. The performance metric for this study was to achieve better classification accuracy by using lesser number of EEG electrodes. At the culmination of this research work, it was shown that maximum classification accuracy of 86.25% is achieved using 14 channel Emotive headset. Future work is aimed at the online EEG data acquisition and processing along with interfacing of robotic lower limb with FPGA controller and Emotiv Headset.

REFERENCES

[1]. Vaughan, T.M., "Guest editorial brain-computer interface technology: a review of the second international meeting," in Neural Systems and Rehabilitation Engineering, IEEE Transactions on , vol.11, no.2, pp.94-109, June 2003

[2]. Norani, N.A.M.; Mansor, W.; Khuan, L.Y., "A review of signal processing in brain computer interface system," in Biomedical Engineering and Sciences (IECBES), 2010 IEEE EMBS Conference on , vol., no., pp.443-449, Nov. 30 2010-Dec. 2 2010

[3]. Dolezal, J.; St'astny, J.; Sovka, P., "Recording and recognition of movement related EEG signal," in Applied Electronics, 2009. AE 2009, vol., no., pp.95-98, 9-10 Sept. 2009

[4]. Gwin JT, Ferris DP. An EEG-based study of discrete isometric and isotonic human lower limb muscle contractions. Journal of NeuroEngineering and Rehabilitation. 2012; 9:35. Doi: 10.1186/1743-0003-9-35.

[5]. Boyd LA, Vidoni ED, Daly JJ. Answering the call: The influence of neuroimaging and electrophysiological evidence on rehabilitation. Phys Ther. 2007; 87(6):684–703. Doi: 10.2522/ptj.20060164.

[6]. Daly JJ, Wolpaw JR. Brain-computer interfaces in neurological rehabilitation. Lancet Neurol. 2008; 7(11):1032–1043. doi: 10.1016/S1474-4422(08)70223-0.

[7]. Gwin JT. et al. Removal of movement artifact from high-density EEG recorded during walking and running. J Neurophysiol. 2010; 103(6):3526–3534. Doi: 10.1152/jn.00105.2010.

[8]. Allen DP, MacKinnon CD. Time-frequency analysis of movement-related spectral power in EEG during repetitive movements: a comparison of methods. J Neurosci Methods. 2010; 186(1):107–115. Doi: 10.1016/j.jneumeth.2009.10.022.

[9]. Alessandro P., Ronald G., Larry F., Jose L.," Neural decoding of treadmill walking from noninvasive electroencephalographic signals". Journal of Neurophysiology Published 1 Oct 2011 Vol. 106 no. 4, 1875-1887 DOI: 10.1152/jn.00104.2011

[10]. Ramoser H, Muller-Gerking J, Pfurtscheller G. Optimal spatial filtering of single trial EEG during imagined hand movement. IEEE Trans Rehabil Eng. 2000; 8(4):441–446. Doi: 10.1109/86.895946.

[11]. Muller-Gerking J, Pfurtscheller G, Flyvbjerg H. Designing optimal spatial filters for single-trial EEG classification in a movement task. Clin Neurophysiol. 1999; 110(5):787–798. Doi: 10.1016/S1388-2457(98)00038-8.

[12]. Khasnobish, A.; Bhattacharyya, S.; Konar, A.; Tibarewala, D.N.; Nagar, A.K., "A Two-fold classification for composite decision about localized arm movement from EEG by SVM and QDA techniques," inNeural Networks (IJCNN), The 2011 International Joint Conference on , vol., no., pp.1344-1351, July 31 2011-Aug. 5 2011

[13]. Unde, S.A.; Shriram, R., "Coherence Analysis of EEG Signal Using Power Spectral Density," in Communication Systems and Network Technologies (CSNT), 2014 Fourth International Conference on , vol., no., pp.871-874, 7-9 April 2014

[14]. Emotiv.com (2013). EPOC Features. [online] Retrieved from: http://www.emotiv.com/epoc/ [Accessed: 5 Mar 2013

[15]. Kaiyang L.; Xiadong Z.; Yuhuan Du,”A SVM based classification of EEG for predicting the movement intent of human body,” in Ubiquitous Robots and Ambient Intelligence (URAI), 2013 Tenth International Conference. Doi: 10.1109/URAI.2013.6677297

[16]. Xiaoyuan Zhu; Cuntai Guan; Jiankang Wu; Yimin Cheng; Yixiao Wang, "Bayesian Method for Continuous Cursor Control in EEG-Based Brain-Computer Interface," in Engineering in Medicine and Biology Society, 2005. IEEE-EMBS 2005. 27th Annual International Conference of the , vol., no., pp.7052-7055, 17-18 Jan. 2006

[17]. Hosni, S.M.; Gadallah, M.E.; Bahgat, S.F.; AbdelWahab, M.S., "Classification of EEG signals using different feature extraction techniques for mental-task BCI," in Computer Engineering & Systems, 2007. ICCES '07. International Conference on , vol., no., pp.220-226, 27-29 Nov. 2007 doi: 10.1109/ICCES.2007.4447052

[18]. Daud, S.S.; Sudirman, R., "Butterworth Bandpass and Stationary Wavelet Transform Filter Comparison for Electroencephalography Signal," in Intelligent Systems, Modelling and Simulation (ISMS), 2015 6th International Conference on , vol., no., pp.123-126, 9-12 Feb. 2015 doi: 10.1109/ISMS.2015.29

[19]. Fathy, A.; Fahmy, A.; ElHelw, M.; Eldawlatly, S., "EEG spectral analysis for attention state assessment: Graphical versus classical classification techniques," in *Biomedical Engineering and Sciences (IECBES), 2012 IEEE EMBS Conference on* , vol., no., pp.888-891, 17-19 Dec. 2012 doi: 10.1109/IECBES.2012.6498088

SOCIETY FOR SCIENCE AND EDUCATION
UNITED KINGDOM

JBEMi JOURNAL OF BIOMEDICAL
ENGINEERING AND MEDICAL IMAGING

ISSN: 2055-1266
VOLUME 2 ISSUE 6

Comparison of Edge Detection Algorithms for Automated Radiographic Measurement of the Carrying Angle

Mason AlNouri[1], Jasim Al Saei[1], Manaf Younis[1], Fadi Bouri[1], Mohamed Ali Al Habash[1], Mohammed Hamza Shah[2]and Mohammed Al Dosari[3]
[1] *Hamad Medical Corporation, Department of Orthopedic Surgery, Doha, Qatar*
[2] *Hamad Medical Corporation, Department of Radiology, Doha, Qatar*
[3]*Hamad Medical Corporation, Bone and Joint Center, Doha, Qatar*
mya2002@qatar-med.cornell.edu; jalsaei@hamad.qa; myounis1@hamad.qa; fbouri@hamad.qa;
malhabash@hamad.qa; mshah1@hamad.qa; maldosari1@hamad.qa

ABSTRACT

Many geometrical angles are measured directly on bone radiographs and are difficult to recall, we wanted to explore an automatic method of measurement. Edge detection was needed to determine bone edges and use them for calculation. There is no consensus on which is the best one for use in skeletal radiographs. We decided to compare commonly used edge detection methods qualitatively and quantitatively for measuring the carrying angle of the elbow using a framework we developed in PHP: Hypertext Preprocessor. Five-Hundred patients' elbow radiographs were collected. They were run through the measurement algorithm using the following edge detection methods: Sobel, Scharr, Prewitt, Frei-Chen, Kirsch, Robinson, Difference of Gaussians (DoG), Laplacian of Gaussian (LoG), Canny, Hough. Five observers manually measured the carrying angle. Results were compared using Intraclass Correlation Coefficient (ICC), Regression Analysis and Validity calculation. The Robinson algorithm was best in the qualitative analysis. Observer ICC was 0.643 which showed a strong agreement. Quantitative analysis revealed that, developing bone caused a significant bias compared to mature bone and DoG algorithm was the best due to low bias, high validity and low processing time. Automated radiographic measurement of the carrying angle of the elbow is a feasible and reliable process.

Keywords: edge detection; carrying angle; elbow; automation; radiographic

1 Introduction

Musculoskeletal imaging encompasses many geometrical angle measurements made directly on bone radiographs, these are usually measured by orthopedic surgeons or diagnostic radiologists as part of their assessment. Unfortunately, there are many angles in common use which vary in their clinical significance as well as their observational reliability [1, 2], and it is sometimes difficult and time consuming to recall and ascertain them all. For that reason, an automated approach may be useful to aid in measurements and assist clinicians in their diagnostic evaluations. In order to achieve automation, a framework has to be explored and set, along which a computer may work upon, for that purpose.

DOI: 10.14738/jbemi.26.1753
Publication Date: 28th December 2015
URL: http://dx.doi.org/10.14738/jbemi. 26.1753

There are multiple methods available for computers that enable them to read and understand images. One notable example of such methods is edge detection, which works by identifying and isolating edges inside an image. Edges are characterized by a substantial difference in intensity across a local area. Edge detection is considered an important and primary step in many analyses and for that reason, it is under continuous research. [3] Its operators and algorithms have been extensively employed in the digital analysis of images from various kinds of medical imaging techniques such as: radiography [4-8], mammography [9], ultrasonography [10, 11], echocardiography [12], computed tomography [13], magnetic resonance [14-17], radioisotope scanning [18], positron emission tomography [19], optical coherence tomography [20, 21], near-infrared [22], fundography [23-27], angiography [28], microscopy [29], confocal microscopy [30-32] and prosthetic vision [33].

Many methods and variations exist in the processes used to achieve the detection and some were found to be more effective than others for analyzing different types of images. For instance in orthopantograms, the Canny algorithm was found to be superior to other tested common methods for qualitative landmark detection [4]. In chest radiographs the Sobel operator was found to be superior to the Roberts operator in detecting edges; however, the Canny algorithm, amongst other common methods, was not studied [34]. In retinal images, one study found the Kirsch operator to be superior to other methods, including the Canny algorithm, in blood vessel edge segmentation [23]. Whereas another study, which did not test the Kirsch operator, found the Canny algorithm to be superior among common methods but inferior to a newly proposed fusion algorithm in accurately delineating blood vessels [24]. Nevertheless, the literature lacks a large scale study that specifically tests edge detection techniques, both quantitatively and qualitatively, for use in analyzing medical images. Additionally, the vast majority of studies carried out on edge detection employed high-level mathematical packages, such as the MATLAB environment [4, 5, 7, 10, 15, 19, 25-27, 30], to perform their analyses; however, although these programs are powerful, they are not readily available for wide use and are not always needed for simpler functions.

In order to address the aforementioned issues, we decided to compare edge detection methods after incorporating them into an algorithm that automatically measures the carrying angle of the elbow, which is defined as the angle made between the axis of the upper arm and that of the forearm [35]. This angle was chosen mainly because of the high precision obtained through radiographic versus goniometric measurements [36] in addition to its good inter-observer reliability [37]. Furthermore, the algorithm was coded in PHP: Hypertext Preprocessor (PHP), a widely used web scripting language, to allow for ease of access and simpler usage.

The aim of this study was to:

1. Compare the reliability of various edge detection operators and algorithms qualitatively and quantitatively in the context of automatic measurements of the carrying angle
2. Check for some patient-specific variables that may affect the reliability of edge detection at the elbow.
3. Develop a framework by which automated measuring of the carrying angle could be made through an easy digital environment

2 Methods

2.1 Image Collection

Five-hundred digitized elbow radiographic images were obtained by searching the hospital's PACS v3.7.3.9 (Picture Archiving and Communication System) database for all stored elbow studies. Since the images were obtained retrospectively with no risk to patients, no ethical approval was required to carry out the study and informed consent was waived after the study was reviewed by the local research committee at the Medical Research Center in accordance with the hospital's rules and regulations policy for research in section III titled "Consent Procedure", subsection 8.3 titled "Types of Consent". Furthermore, approval to access the stored images was given by the same committee after completing their review.

The search results were then sorted by age and manually selected in order to meet the required quota of one-hundred images, divided into fifty males and fifty females, of patients' elbows taken at each of the following ages: one, five, nine, eleven and twenty to forty. These ages were selected to approximately represent the different stages of ossification [38]. *Table 1* shows the patient distribution.

Table 1 Overall distribution of patient and variables for elbow radiographs

	Number of Patient Radiographs			
	Sex		**Side**	
Age	**Males**	**Females**	**Left**	**Right**
1	50	50	42	58
5	50	50	55	45
9	50	50	57	43
11	50	50	51	49
20-40	50	50	49	51
Totals	250	250	254	246
Total Patient Radiographs: 500				

After a patient's radiograph was selected, it was viewed on a monitor set at a screen resolution of 1024 × 768 using the PACS Viewer Component v3.7.3.9078. Any image containing the following criteria was excluded:-

- Major deformities of the humerus, radius or ulna
- Displaced fractures
- Bone lesions
- Anterior-posterior view taken in forearm pronation or any other inappropriate position
- Visible bone implants
- External interference such as slabs, casts or an examiner's hand

The brightness and contrast settings of the radiograph were altered within the viewer in order to minimize soft-tissue and skin interference and maximize visibility of the bone. Subsequently, the screen was captured using the 'Print Screen' function, pasted into Microsoft Windows Paint v6.1 and further cropping of the corners was carried out. Finally, all remaining labels were removed from the image and a scale was applied in order to approximately obtain a width of 400 and a height of 500. The end result, as shown in *Figure 1*, was then stored as a png image in a folder and recorded in a spreadsheet with a study specific identifier along with the patient's age, sex and the limb side.

Figure 1 A sample Anterior-Posterior elbow radiograph to be used as an input image for automated measurement

2.2 Measurement Algorithm

The algorithm used to measure the carrying angle from the input images was programmed in PHP and run on the PHP Engine v5.5.8 using an Intel i7 Core 3.46GHz 8.0GB RAM 64-bit Windows 7 Professional system in order to centralize the processing of images on a single server while allowing various users to utilize the service.

Steps involved in the algorithm:-

Step-1 Create an array of all images in the specified system folder

Step-2 Enter a loop that stops after all the images have been processed

Step-3 Apply the edge detection algorithm to the image

Step-4 Loop through all the image's pixels and eliminate pixels according to a set threshold

Step-5 Create different groups for all remaining pixels adjacent to each other

Step-6 Collect the first six groups which span the highest value for vertical range

Step-7 Define the bone borders based on each group's location within the image space

Step-8 Estimate the central axis of the humerus and ulna based on the defined borders

Step-9 Calculate the carrying angle of the elbow based on the bone axes and store the result

Step-10 Go to Step 2 or end the loop and output all results

All five-hundred images were placed in a folder and run through the algorithm a total of eight times to test all the edge detection methods included in this study.

2.3 Edge Detection Algorithms

All the following algorithms were chosen due to their common use and were tested in this study by being incorporated into the measurement algorithm in *2.2* at Step 3. The threshold values in *2.2* at Step 4 were different for each algorithm and they were determined by testing the algorithm on ten random elbow radiographs and selecting the output with the most accurate values obtained for the carrying angle.

2.3.1 Sobel Operator

The Sobel Operator was applied by carrying out a two dimensional image convolution in both the vertical and the horizontal direction. The following matrices were used:-

$$F_x = \begin{vmatrix} -1 & 0 & +1 \\ -2 & 0 & +2 \\ -1 & 0 & +1 \end{vmatrix} \qquad F_y = \begin{vmatrix} +1 & +2 & +1 \\ 0 & 0 & 0 \\ -1 & -2 & -1 \end{vmatrix} \tag{1}$$

F_x is the horizontal derivative and F_y is the vertical derivative at a specific point in the image

2.3.2 Scharr Operator

The Scharr Operator was applied in similar way to the Sobel in *2.3.1* using the following matrices:-

$$F_x = \begin{vmatrix} -3 & 0 & +3 \\ -10 & 0 & +10 \\ -3 & 0 & +3 \end{vmatrix} \qquad F_y = \begin{vmatrix} +3 & +10 & +3 \\ 0 & 0 & 0 \\ -3 & -10 & -3 \end{vmatrix} \tag{2}$$

2.3.3 Prewitt Operator

The Prewitt Operator was applied in similar way to the Sobel in *2.3.1* using the following matrices:-

$$F_x = \begin{vmatrix} -1 & 0 & +1 \\ -1 & 0 & +1 \\ -1 & 0 & +1 \end{vmatrix} \qquad F_y = \begin{vmatrix} +1 & +1 & +1 \\ 0 & 0 & 0 \\ -1 & -1 & -1 \end{vmatrix} \tag{3}$$

2.3.4 Frei-Chen Filter

The Frei-Chen Filter was applied by performing nine separate image convolutions using the nine matrices below:-

$$\begin{gathered} W_1 = \frac{1}{2\sqrt{2}}\begin{vmatrix} +1 & +\sqrt{2} & +1 \\ 0 & 0 & 0 \\ -1 & -\sqrt{2} & -1 \end{vmatrix} \quad W_2 = \frac{1}{2\sqrt{2}}\begin{vmatrix} +1 & 0 & -1 \\ +\sqrt{2} & 0 & -\sqrt{2} \\ +1 & 0 & -1 \end{vmatrix} \quad W_3 = \frac{1}{2\sqrt{2}}\begin{vmatrix} 0 & -1 & +\sqrt{2} \\ +1 & 0 & -1 \\ -\sqrt{2} & +1 & 0 \end{vmatrix} \\ W_4 = \frac{1}{2\sqrt{2}}\begin{vmatrix} +\sqrt{2} & -1 & 0 \\ -1 & 0 & +1 \\ 0 & +1 & -\sqrt{2} \end{vmatrix} \quad W_5 = \frac{1}{2}\begin{vmatrix} 0 & +1 & 0 \\ -1 & 0 & -1 \\ 0 & +1 & 0 \end{vmatrix} \quad W_6 = \frac{1}{2}\begin{vmatrix} -1 & 0 & +1 \\ 0 & 0 & 0 \\ +1 & 0 & -1 \end{vmatrix} \\ W_7 = \frac{1}{6}\begin{vmatrix} +1 & -2 & +1 \\ -2 & +4 & -2 \\ +1 & -2 & +1 \end{vmatrix} \quad W_8 = \frac{1}{6}\begin{vmatrix} -2 & +1 & -2 \\ +1 & +4 & +1 \\ -2 & +1 & -2 \end{vmatrix} \quad W_8 = \frac{1}{3}\begin{vmatrix} +1 & +1 & +1 \\ +1 & +1 & +1 \\ +1 & +1 & +1 \end{vmatrix} \end{gathered} \tag{4}$$

This was then followed by the calculation of the weighted average from the results of the image convolutions.

2.3.5 Kirsch Operator

The Kirsch Operator was applied by rotating a single kernel matrix through eight different compass directions and calculating the final sum resulting from the addition of all the image convolutions in all directions. The kernel matrix is given below:-

$$K_1 = \begin{vmatrix} +5 & +5 & +5 \\ -3 & 0 & -3 \\ -3 & -3 & -3 \end{vmatrix} \tag{5}$$

2.3.6 Robinson Operator

The Robinson Operator was applied in similar way to the Kirsch Operator in *2.3.5* using the following kernel matrix:-

$$R_1 = \begin{vmatrix} +1 & +1 & +1 \\ +1 & -2 & +1 \\ -1 & -1 & -1 \end{vmatrix} \tag{6}$$

2.3.7 Difference of Gaussians

The Difference of Gaussians (DoG) was applied by using two Gaussian blur masks at different intensities, followed by subtracting their results. The Gaussian function and the matrix used for convolution is given below:-

$$G(x, y) = \frac{1}{\sqrt{2\pi\sigma^2}} e^{-\frac{x^2+y^2}{2\sigma^2}} \qquad G = \begin{vmatrix} +1 & +2 & +1 \\ +2 & +4 & +2 \\ +1 & +2 & +1 \end{vmatrix} \tag{7}$$

Where *x* is the horizontal and *y* is the vertical coordinate inside an image. σ is the standard deviation of the Gaussian function.

2.3.8 Laplacian of Gaussian

The Laplacian of Gaussian (LoG) was applied by using a Gaussian blur mask on the image along with a Laplacian kernel. The Gaussian, Laplacian and combined functions as well as the matrix used for convolution are given below:-

$$G(x, y) = \frac{1}{\sqrt{2\pi\sigma^2}} e^{-\frac{x^2+y^2}{2\sigma^2}} \tag{8}$$

$$L(x, y) = \frac{1}{\sqrt{2\pi\sigma^2}} e^{-\frac{x^2+y^2}{2\sigma^2}} \tag{9}$$

$$LoG(x,y) = -\frac{1}{\pi\sigma^4}\left[1 - \frac{x^2+y^2}{2\sigma^2}\right]e^{-\frac{x^2+y^2}{2\sigma^2}}$$

$$LoG = \begin{vmatrix} 0 & 0 & -1 & 0 & 0 \\ 0 & -1 & -2 & -1 & 0 \\ -1 & -2 & +16 & -2 & -1 \\ 0 & -1 & -2 & -1 & 0 \\ 0 & 0 & -1 & 0 & 0 \end{vmatrix}$$

2.3.9 Canny Algorithm

The Canny Algorithm was applied by following the four steps:-

1. Blur the image using the following Gaussian mask

$$G = \begin{vmatrix} +2 & +4 & +5 & +4 & +2 \\ +4 & +9 & +12 & +9 & +4 \\ +5 & +12 & +15 & +12 & +5 \\ +4 & +9 & +12 & +9 & +4 \\ +2 & +4 & +5 & +4 & +2 \end{vmatrix} \qquad (10)$$

2. Apply the Sobel Operator as in *2.3.1* then calculate the gradient angle using the equation

$$\theta = atan2(y,x)$$

   Where θ is the gradient angle, y is the vertical gradient and x is the horizontal gradient

3. Suppress non-maximum pixels within the image based on the neighboring pixels

4. Apply a double threshold to the remaining pixels

2.3.10 Hough Transform

The Hough Transform was applied through the following steps:-

1. Apply the Canny edge detector as in *2.3.9*

2. Create the Hough space for remaining pixels using the following equation

$$r = x\cos(\theta) + y\sin(\theta) \qquad (11)$$

Where r is the distance of the line from the origin, θ is the slope of that line and x, y are the coordinates of an arbitrary point on that line

3. Collect votes from the image’s pixels for all the lines in the Hough space

4. Dehough the lines with the most votes by using their predetermined line equation

2.4 Observer Measurements

Five different observers were each given the 500 images obtained from the collection in *2.1* in order to manually measure the carrying angle using the radiographic method. The observers were 'blinded' by not being given any details about the automatic measurement algorithm until after the completion of all manual measurements. The angle was determined by drawing the long axis of the humerus and the long axis of the ulna followed by measuring the angle made by their bisection as shown in *Figure 2* [37]. Afterwards, the measurements were recorded in a MySQL database for later comparison to the values obtained from the algorithm.

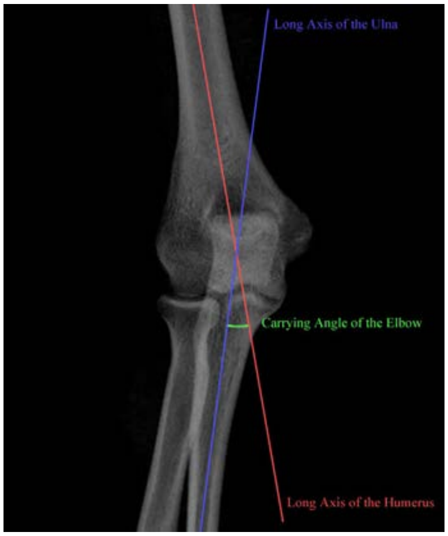

Figure 2 Radiograph showing the labelled long axes of the Humerus and Ulna with the formed Carrying Angle

2.5 Algorithm Validity

The validity of all automated measurements was calculated by comparing all of the readings to the real value of the carrying angle, which was assumed to be the mean of all observer measurements, in order to check if they fall within a $\pm 5^0$ range in which case the readings would be considered correct. This range was chosen based on the approximate error observed in different readings of the carrying angle [36, 49]. A percent validity was then obtained through dividing the total number of correct readings by the total number of readings and then multiplying by 100.

2.6 Statistical Analysis

All data were analyzed within the SPSS program (v20, SPSS Inc., Chicago, IL, USA). All p values <= 0.05 were considered statistically significant. In order to evaluate the consistency of observer measurements, the Intraclass Correlation Coefficient (ICC) was calculated for single readings. Based on the values of the ICC the following agreement ratings were selected: poor (0-0.200), fair (0.201-0.400), moderate (0.401-0.600), strong (0.601-0.800) and excellent (>0.801) [50]. The 95% confidence interval range was also quantified. Subsequently, the manual and automated readings obtained for the carrying angle were compared for any biases using linear regression analyses. This was carried out by first calculating the mean of all observer readings for a single elbow, the result was considered the real value of the carrying angle. After that, the difference as well as the average of the real value and the algorithm's measurement was calculated. The average was set to be the independent variable and the difference was set to be the dependent variable. Consequently, the measurements were then split by variables of age, sex and side and the regression analysis was carried out for each one.

3 Results

3.1 Qualitative Comparison

All the output images were checked in order to identify which edge detection method included the most accurately defined bone edge with the least noise. Samples can be seen in *Figure 3*. With regards to the output from the Sobel, Scharr and Prewitt Operators, the level of noise and edge accuracy was almost similar with only a negligible reduction in noise by the Scharr Operator. When compared to the prior three, the Frei-Chen output showed a largely reduced external noise but a greatly increased internal bone noise; moreover, the edges were generally less accurate and much thicker than all other outputs. The Kirsch and Robinson Operators were superior to all other methods in both the noise level and the edge accuracy. Compared to each other, the Robinson output exhibited slightly less noise than the Kirsch output but no significant change was noted in edge thickness or accuracy. The DoG output was largely similar to the Frei-Chen output with a notable increase in noise as well as edge thickness. The LoG output was similar to the three initially mentioned operators in terms of edge accuracy, the thickness was slightly increased; however, there was a small decrease in external noise coupled with a large increase in internal noise. The Canny output revealed a highly accurate thin edge but the image contained more noise, both internal and external, than the Kirsch and Robinson output images. Finally, the Hough output revealed a thick edge which was less accurate than all other outputs, with little internal and external noise.

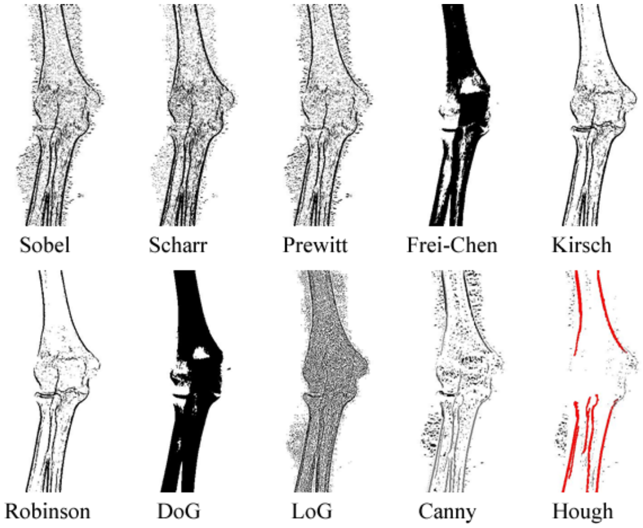

Figure 3 Sample output images from all ten edge detection methods obtained from the input image in Figure 1

In summary, the Robinson Operator was superior to other methods for edge accuracy and noise level. *Table 2* shows the relative rankings of all edge detection methods.

Table 2 Relative rankings of all ten edge detection methods with regards to various aspects of qualitative analysis. Ascending order (A) Descending order (D)

Edge Accuracy (D)	Edge Thickness (A)	Internal Noise (A)	External Noise (A)
Robinson	Canny	Robinson	Robinson
Kirsch	Robinson	Kirsch	Kirsch
Canny	Kirsch	Hough	DoG
LoG	Prewitt	Canny	Frei-Chen
Scharr	Sobel	Prewitt	Hough
Sobel	Scharr	Sobel	Canny
Prewitt	LoG	Scharr	LoG
DoG	Hough	LoG	Scharr
Frei-Chen	Frei-Chen	Frei-Chen	Prewitt
Hough	DoG	DoG	Sobel

3.2 Observer Comparison

The ICC for all observer measurements was found to be 0.643 (95% CI: 0.547 to 0.718). This indicated a strong agreement based on the predefined ratings. The ICC values were also calculated after separating the observer readings by variables of age, sex and side and, although there were some differences in the ICC values, they did not show any statistical significance based on the confidence interval ranges. ICC values are shown in *Table 3*.

Table 3 The Intraclass Correlation Coefficients (ICC) and 95% Confidence Intervals calculated based on observer carrying angle measurements for all radiographs which was divided by variables age, sex and side

Group	ICC	95% Confidence Interval	
		Lower	Upper
Age 1	0.546	0.410	0.663
Age 5	0.589	0.456	0.699
Age 9	0.607	0.437	0.731
Age 11	0.738	0.641	0.813
Age 20-40	0.755	0.632	0.837
Males	0.598	0.486	0.687
Females	0.691	0.599	0.762
Left Side	0.651	0.542	0.734
Right Side	0.635	0.527	0.719
Overall	0.643	0.547	0.718

3.3 Algorithm Comparisons

The measurements for each edge detection method, as well as their final mean, were checked for bias, validity and processing time.

3.3.1 Sobel Operator Results

The Sobel measurements obtained an overall B value of -0.729 (95% CI: -0.815 to -0.643 $p<0.001$) with an overall 67% validity and an average 3min 27s of processing time per image. Further analysis based on variables revealed no statistically significant differences in any reading. *Table 4* shows the detailed results obtained from each variable.

Table 4 Results for the Sobel Operator measurements showing B values, Standard Error, 95% Confidence Intervals, p values and validity, all divided by the variables age, sex and side

Group	B	Standard Error	95% Confidence Interval		*p* value	Validity
			Lower	Upper		
Age 1	-0.794	0.101	-0.994	-0.594	<0.001	69%
Age 5	-0.791	0.095	-0.980	-0.602	<0.001	61%
Age 9	-0.735	0.087	-0.908	-0.562	<0.001	66%
Age 11	-0.548	0.099	-0.745	-0.351	<0.001	69%
Age 20-40	-0.841	0.121	-01.08	-0.601	<0.001	69%
Males	-0.759	0.067	-0.890	-0.628	<0.001	66%
Females	-0.703	0.058	-0.818	-0.588	<0.001	67%
Left Side	-0.658	0.057	-0.771	-0.545	<0.001	66%
Right Side	-0.816	0.067	-0.949	-0.684	<0.001	68%
Overall	-0.729	0.044	-0.815	-0.643	<0.001	67%

3.3.2 Scharr Operator Results

The Scharr measurements obtained an overall B value of -0.633 (95% CI: -0.717 to -0.548 *p*<0.001) with an overall 72% validity and an average 3min 38s of processing time per image. Further analysis based on variables revealed a higher validity result in the Age 20-40 group at 88%. *Table 5* shows the detailed results obtained from each variable.

Table 5 Results for the Scharr Operator measurements showing B values, Standard Error, 95% Confidence Intervals, p values and validity all divided by the variables age, sex and side

Group	**B**	**Standard Error**	**95% Confidence Interval**		***p* value**	**Validity**
			Lower	**Upper**		
Age 1	-0.709	0.093	-0.894	-0.525	<0.001	73%
Age 5	-0.785	0.100	-0.983	-0.587	<0.001	61%
Age 9	-0.664	0.110	-0.883	-0.444	<0.001	61%
Age 11	-0.472	0.093	-0.656	-0.288	<0.001	75%
Age 20-40	-0.537	0.083	-0.702	-0.373	<0.001	88%
Males	-0.603	0.064	-0.729	-0.477	<0.001	72%
Females	-0.646	0.059	-0.762	-0.531	<0.001	72%
Left Side	-0.552	0.056	-0.663	-0.441	<0.001	73%
Right Side	-0.729	0.066	-0.858	-0.600	<0.001	70%
Overall	-0.633	0.043	-0.717	-0.548	<0.001	72%

3.3.3 Prewitt Operator Results

The Prewitt measurements obtained an overall B value of -0.730 (95% CI: -0.819 to -0.642 *p*<0.001) with an overall 65% validity and an average 3min 19s of processing time per image. Further analysis based on variables revealed a significantly lower B value when comparing the Age 1 group (B = -0.956 95% CI: -1.157 to -0.755 *p*<0.001) and the Left Side group (B = -0.631 95% CI: -0.749 to -0.512 *p*<0.001). *Table 6* shows the detailed results obtained from each variable.

Table 6 Results for the Prewitt Operator measurements showing B values, Standard Error, 95% Confidence Intervals, p values and validity all divided by the variables age, sex and side

Group	B	Standard Error	95% Confidence Interval		*p* value	Validity
			Lower	Upper		
Age 1	-0.956	0.101	-1.157	-0.755	<0.001	69%
Age 5	-0.602	0.080	-0.761	-0.444	<0.001	65%
Age 9	-0.641	0.099	-0.838	-0.445	<0.001	64%
Age 11	-0.596	0.100	-0.795	-0.397	<0.001	63%
Age 20-40	-0.927	0.127	-1.179	-0.674	<0.001	64%
Males	-0.722	0.061	-0.843	-0.602	<0.001	66%
Females	-0.739	0.066	-0.869	-0.609	<0.001	64%
Left Side	-0.631	0.060	-0.749	-0.512	<0.001	67%
Right Side	-0.846	0.067	-0.978	-0.714	<0.001	63%
Overall	-0.730	0.045	-0.819	-0.642	<0.001	65%

3.3.4 Frei-Chen Filter Results

The Frei-Chen measurements obtained an overall B value of -0.539 (95% CI: -0.615 to -0.462 *p*<0.001) with an overall 75% validity and an average 1min 16s of processing time per image. Further analysis based on variables revealed a significantly higher B value in both the Age 11 group (B = -0.251 95% CI: -0.393 to -0.109 *p*=0.001) and the Age 20-40 group (B = -0.327 95% CI: -0.438 to -0.215 *p*<0.001) with a significantly lower B value in the Age 1 group (B = -0.879 95% CI: -1.071 to -0.687 *p*<0.001). Similarly, the validity results were much higher in the Age 11 (83%) and Age 20-40 group (95%) compared to the Age 1 group (61%). *Table 7* shows the detailed results obtained from each variable.

Table 7 Results for the Frei-Chen Filter measurements showing B values, Standard Error, 95% Confidence Intervals, p values and validity all divided by the variables age, sex and side

Group	**B**	**Standard Error**	**95% Confidence Interval**		***p* value**	**Validity**
			Lower	**Upper**		
Age 1	-0.879	0.097	-1.071	-0.687	<0.001	61%
Age 5	-0.671	0.094	-0.858	-0.483	<0.001	69%
Age 9	-0.512	0.084	-0.679	-0.345	<0.001	69%
Age 11	-0.251	0.072	-0.393	-0.109	0.001	83%
Age 20-40	-0.327	0.056	-0.438	-0.215	<0.001	95%
Males	-0.543	0.056	-0.653	-0.432	<0.001	72%
Females	-0.535	0.055	-0.642	-0.427	<0.001	78%
Left Side	-0.404	0.048	-0.500	-0.309	<0.001	79%
Right Side	-0.682	0.061	-0.801	-0.562	<0.001	72%
Overall	-0.539	0.039	-0.615	-0.462	<0.001	75%

3.3.5 Kirsch Operator Results

The Kirsch measurements obtained an overall B value of -0.432 (95% CI: -0.505 to -0.358 *p*<0.001) with an overall 77% validity and an average 1min 20s of processing time per image. Further analysis based on variables revealed a significantly lower B value when comparing the Age 1 group (B = -0.621 95% CI: -

0.791 to -0.451 *p*<0.001) and the Age 11 group (B = -0.298 95% CI: -0.438 to -0.159 *p*<0.001). Moreover, the validity was higher in the Age 20-40 group (85%) compared to the Age 9 group (67%). *Table 8* shows the detailed results obtained from each variable.

Table 8 Results for the Kirsch Operator measurements showing B values, Standard Error, 95% Confidence Intervals, p values and validity all divided by the variables age, sex and side

Group	B	Standard Error	95% Confidence Interval		*p* value	Validity
			Lower	Upper		
Age 1	-0.621	0.086	-0.791	-0.451	<0.001	79%
Age 5	-0.404	0.073	-0.548	-0.260	<0.001	73%
Age 9	-0.516	0.104	-0.723	-0.310	<0.001	67%
Age 11	-0.298	0.070	-0.438	-0.159	<0.001	82%
Age 20-40	-0.303	0.079	-0.460	-0.147	<0.001	85%
Males	-0.455	0.053	-0.559	-0.351	<0.001	77%
Females	-0.408	0.053	-0.513	-0.303	<0.001	77%
Left Side	-0.405	0.052	-0.506	-0.303	<0.001	76%
Right Side	-0.465	0.055	-0.573	-0.358	<0.001	79%
Overall	-0.432	0.037	-0.505	-0.358	<0.001	77%

3.3.6 Robinson Operator Results

The Robinson measurements obtained an overall B value of -0.511 (95% CI: -0.597 to -0.425 *p*<0.001) with an overall 77% validity and an average 1min 13s of processing time per image. Further analysis based on variables revealed a significantly higher B value in both the Age 11 group (B = -0.284 95% CI: -0.434 to -0.134 *p*<0.001) and the Age 20-40 group (B = -0.389 95% CI: -0.549 to -0.230 *p*<0.001) with a significantly lower B value in the Age 1 group (B = -0.928 95% CI: -1.181 to -0.675 *p*<0.001). Additionally, the validity was higher in the Age 20-40 group (86%). *Table 9* shows the detailed results obtained from each variable.

Table 9 Results for the Robinson Operator measurements showing B values, Standard Error, 95% Confidence Intervals, p values and validity all divided by the variables age, sex and side

Group	B	Standard Error	95% Confidence Interval		*p* value	Validity
			Lower	Upper		
Age 1	-0.928	0.128	-1.181	-0.675	<0.001	75%
Age 5	-0.516	0.088	-0.690	-0.342	<0.001	71%
Age 9	-0.457	0.094	-0.645	-0.270	<0.001	70%
Age 11	-0.284	0.076	-0.434	-0.134	<0.001	81%
Age 20-40	-0.389	0.080	-0.549	-0.230	<0.001	86%
Males	-0.585	0.061	-0.706	-0.464	<0.001	74%
Females	-0.429	0.063	-0.553	-0.306	<0.001	79%
Left Side	-0.446	0.059	-0.561	-0.330	<0.001	75%
Right Side	-0.588	0.066	-0.718	-0.458	<0.001	78%
Overall	-0.511	0.044	-0.597	-0.425	<0.001	77%

3.3.7 Difference of Gaussians Results

The DoG measurements obtained an overall B value of -0.487 (95% CI: -0.559 to -0.415 *p*<0.001) with an overall 80% validity and an average 1min 33s of processing time per image. Further analysis based on variables revealed a significantly higher B value in both the Age 11 group (B = -0.226 95% CI: -0.359 to -0.093 *p*=0.001) and the Age 20-40 group (B = -0.302 95% CI: -0.468 to -0.136 *p*<0.001) with a significantly lower B value in the Age 1 group (B = -0.630 95% CI: -0.808 to -0.452 *p*<0.001) and the Age 5 group (B = -0.654 95% CI: -0.810 to -0.499 *p*<0.001). Additionally, the validity was higher in the Age 20-40 group (94%). *Table 10* shows the detailed results obtained from each variable.

Table 10 Results for the Difference of Gaussians measurements showing B values, Standard Error, 95% Confidence Intervals, p values and validity all divided by the variables age, sex and side

Group	B	Standard Error	95% Confidence Interval		*p* value	Validity
			Lower	Upper		
Age 1	-0.630	0.090	-0.808	-0.452	<0.001	76%
Age 5	-0.654	0.078	-0.810	-0.499	<0.001	70%
Age 9	-0.552	0.084	-0.718	-0.386	<0.001	72%
Age 11	-0.226	0.067	-0.359	-0.093	0.001	86%
Age 20-40	-0.302	0.084	-0.468	-0.136	<0.001	94%
Males	-0.538	0.053	-0.643	-0.433	<0.001	76%
Females	-0.429	0.051	-0.529	-0.329	<0.001	83%
Left Side	-0.434	0.049	-0.529	-0.338	<0.001	80%
Right Side	-0.552	0.056	-0.662	-0.443	<0.001	79%
Overall	-0.487	0.037	-0.559	-0.415	<0.001	80%

3.3.8 Laplacian of Gaussian Results

The LoG measurements obtained an overall B value of -1.024 (95% CI: -1.122 to -0.927 *p*<0.001) with an overall 55% validity and an average 1min 37s of processing time per image. Further analysis based on variables revealed a significantly higher B value in both the Age 11 group (B = -0.495 95% CI: -0.701 to -0.290 *p*<0.001) and the Age 9 group (B = -0.799 95% CI: -0.986 to -0.611 *p*<0.001) with a significantly lower B value in the Age 1 group (B = -1.419 95% CI: -1.614 to -1.224 *p*<0.001). Moreover, the validity was higher in the Age 11 group (72%) and lower in the Age 1 group (30%). *Table 11* shows the detailed results obtained from each variable.

Table 11 Results for the Laplacian of Gaussian measurements showing B values, Standard Error, 95% Confidence Intervals, p values and validity all divided by the variables age, sex and side

Group	B	Standard Error	95% Confidence Interval		*p* value	Validity
			Lower	Upper		
Age 1	-1.419	0.098	-1.614	-1.224	<0.001	30%
Age 5	-1.091	0.112	-1.314	-0.869	<0.001	48%
Age 9	-0.799	0.094	-0.986	-0.611	<0.001	58%
Age 11	-0.495	0.103	-0.701	-0.290	<0.001	72%
Age 20-40	-0.977	0.111	-1.198	-0.756	<0.001	68%
Males	-1.089	0.072	-1.231	-0.946	<0.001	50%
Females	-0.963	0.068	-1.097	-0.828	<0.001	60%
Left Side	-0.943	0.069	-1.079	-0.806	<0.001	54%
Right Side	-1.114	0.071	-1.254	-0.975	<0.001	57%
Overall	-1.024	0.050	-1.122	-0.927	<0.001	55%

3.3.9 Canny Algorithm Results

The Canny measurements obtained an overall B value of -0.881 (95% CI: -0.978 to -0.785 $p<0.001$) with an overall 67% validity and an average 5min 3s of processing time per image. Further analysis based on variables revealed a significantly lower B value when comparing the Age 1 group (B = -1.259 95% CI: -1.494 to -1.024 $p<0.001$) and the Age 11 group (B = -0.663 95% CI: -0.883 to -0.444 $p<0.001$). Additionally, the validity was higher in the Age 20-40 group (81%). *Table 12* shows the detailed results obtained from each variable.

Table 12 Results for the Canny measurements showing B values, Standard Error, 95% Confidence Intervals, p values and validity all divided by the variables age, sex and side

Group	B	Standard Error	95% Confidence Interval		*p* value	Validity
			Lower	Upper		
Age 1	-1.259	0.118	-1.494	-1.024	<0.001	58%
Age 5	-0.869	0.087	-1.042	-0.696	<0.001	62%
Age 9	-0.788	0.111	-1.008	-0.569	<0.001	64%
Age 11	-0.663	0.111	-0.883	-0.444	<0.001	69%
Age 20-40	-0.778	0.114	-1.004	-0.553	<0.001	81%
Males	-0.895	0.066	-1.026	-0.764	<0.001	65%
Females	-0.868	0.073	-1.012	-0.724	<0.001	68%
Left Side	-0.889	0.064	-1.016	-0.763	<0.001	63%
Right Side	-0.858	0.078	-1.011	-0.704	<0.001	70%
Overall	-0.881	0.049	-0.978	-0.785	<0.001	67%

3.3.10 Hough Transform Results

The Hough measurements obtained an overall B value of -0.558 (95% CI: -0.637 to -0.479 $p<0.001$) with an overall 78% validity and an average 8min 13s of processing time per image. Further analysis based on variables revealed a significantly higher B value in the Age 11 group (B = -0.239 95% CI: -0.372 to -0.106 $p=0.001$) with a significantly lower B value in the Age 1 group (B = -1.054 95% CI: -1.249 to -0.858

p<0.001). Additionally, the validity was higher in the Age 20-40 group (93%) and lower in the Age 1 group (65%). *Table 13* shows the detailed results obtained from each variable.

Table 13 Results for the Hough measurements showing B values, Standard Error, 95% Confidence Intervals, p values and validity all divided by the variables age, sex and side

Group	B	Standard Error	95% Confidence Interval		*p* value	Validity
			Lower	Upper		
Age 1	-1.054	0.099	-1.249	-0.858	<0.001	65%
Age 5	-0.515	0.078	-0.670	-0.360	<0.001	73%
Age 9	-0.412	0.084	-0.578	-0.246	<0.001	74%
Age 11	-0.239	0.067	-0.372	-0.106	0.001	84%
Age 20-40	-0.315	0.067	-0.448	-0.182	<0.001	93%
Males	-0.586	0.054	-0.692	-0.479	<0.001	76%
Females	-0.530	0.060	-0.648	-0.412	<0.001	80%
Left Side	-0.507	0.052	-0.609	-0.404	<0.001	80%
Right Side	-0.624	0.062	-0.747	-0.501	<0.001	76%
Overall	-0.558	0.040	-0.637	-0.479	<0.001	78%

3.3.11 Combined Results

These results were obtained by running the same analyses after calculating the mean for all different algorithm measurements of a single carrying angle. This method obtained an overall B value of -0.281 (95% CI: -0.349 to -0.213 *p*<0.001) with an overall 80% validity. Further analysis based on variables revealed a higher validity result in the Age 20-40 group at 92%. *Table 14* shows the detailed results obtained from each variable.

Table 14 Results for the Combined measurements showing B values, Standard Error, 95% Confidence Intervals, p values and validity all divided by the variables age, sex and side

Group	B	Standard Error	95% Confidence Interval		*p* value	Validity
			Lower	Upper		
Age 1	-0.371	0.088	-0.546	-0.195	<0.001	73%
Age 5	-0.361	0.070	-0.500	-0.221	<0.001	76%
Age 9	-0.318	0.079	-0.475	-0.161	<0.001	75%
Age 11	-0.152	0.066	-0.284	-0.020	0.024	83%
Age 20-40	-0.207	0.075	-0.357	-0.058	0.007	92%
Males	-0.286	0.049	-0.382	-0.190	<0.001	80%
Females	-0.274	0.049	-0.371	-0.177	<0.001	80%
Left Side	-0.280	0.045	-0.370	-0.191	<0.001	80%
Right Side	-0.283	0.054	-0.388	-0.177	<0.001	79%
Overall	-0.281	0.035	-0.349	-0.213	<0.001	80%

4 Discussion

In the qualitative comparison, the Robinson operator was superior with the Kirsch operator closely behind. This revealed that the best methods for isolating bone edges in radiographic images of the extremities, especially in diaphyseal regions, are those which incorporate kernels in all eight compass directions. The Canny algorithm was also relatively more successful than other methods probably due to the incorporation of gradient angles, which is somewhat related to isolating edges in compass directions. Interestingly however, these results did not coincide with the ones obtained from the carrying angle measurement comparisons. This indicates that, for the purposes of the automated algorithm used in this study, there are different factors which affect the measurement's validity.

When comparing the observer measurements, a strong positive inter-rater correlation was noted; however, the actual value for the ICC was significantly lower in this study, 0.643 (95% CI: 0.547 to 0.718) compared with the literature, 0.80 (95% CI: 0.75 – 0.84) [37]. This may have been due to the difference in the subject ages, number of elbows and the number of observers. In Goldfarb's study, the minimum age recruited was 12 and the total number of subjects was 178 with three different observers. The inclusion of the pediatric population at all stages of ossification as well as the increase in number to 500 with five different observers making measurements may have contributed to a lower ICC in our study.

Comparison of the algorithms revealed varying degrees of negative bias, the highest obtained in the LoG algorithm and the lowest in the Kirsch. Interestingly, after analysis of the variables, it was noted that the greatest number of significant bias came from the younger age groups and gradually decreased as the age increased. This indicated that skeletally immature bones inherently cause a bias in the automated readings of the carrying angle. This may be due to several reasons related to the radiographic characteristics of these bones such as: Poor contrast between the bone and the film, vague bone borders especially in non-ossified areas, rotated radiographic view related to questionable limb positioning due to the uncooperative nature of the patient and finally, short overall limb length which may affect the availability of adequate continuous bone edges.

In comparing the algorithm validity, the highest value for overall results came from the DoG algorithm (80%), while the highest value after variable analysis came from the age 20-40 group of the Frei-Chen algorithm (95%) followed closely by the same group in the DoG algorithm (94%) and the Hough Transform (93%). The lowest value for overall results was found in the LoG algorithm (55%), while the lowest value after variable analysis came from the age 1 group of the LoG algorithm (30%). As expected, algorithms with higher values for validity also had less bias than others.

With regards to the average processing time, the Robinson Operator (1min 13s) required the least time followed closely by the Frei-Chen (1min 16s) and Kirsch (1min 20s) Operator and then the DoG (1min 33s) and LoG (1min 37s) algorithms. Therefore, the best edge detection method based on all these factors was the DoG Algorithm which had a relatively low bias, high validity and low processing time. The Frei-Chen Algorithm was comparable but had a slightly lower validity while the Hough Transform had a much longer processing time. The worst edge detection method used in this study was found to be the LoG Algorithm due to its high bias and low validity.

The combined results showed the least bias, which was an expected consequence of averaging, but did not increase validity. They also suffered from the longest processing time due to the need to run all the edge detection methods before calculating the mean. This favored the usage of a single edge detector rather than a hybrid one.

The reasons which may have contributed to the DoG Algorithm being superior may be seen in the qualitative analysis which showed the highest edge thickness and internal noise with low edge accuracy and external noise. These factors can also be seen in the Frei-Chen Algorithm and the Hough Transform, which have obtained results comparable to the DoG Algorithm. Consequently, the most important qualitative factors needed for automated angle measurements within diaphyseal areas of bone are: high edge thickness, high internal noise, low edge accuracy and low external noise. The LoG algorithm's poor results may have been due to its insensitivity towards external noise, which results in the incorrect approximation of the bone's edge.

5 Conclusion

The automated radiographic measurement of the carrying angle of the elbow is a very feasible and reliable process given the low bias and high validity of the algorithm when the DoG Algorithm is employed, especially if used strictly for mature bone. Since the lowest processing time was 1min 13s, the framework developed in this study may not be applicable for real-time processing or instant analysis results; however, it may be more practical to employ it as a batch processor. Nevertheless, if centralized on a high-end server, it could potentially provide fast results for clients, but this option has to be explored further.

ACKNOWLEDGEMENTS

This study was supported by the Medical Research Center at Hamad Medical Corporation. We thank Mr Yahya AlNouri for funding this project.

REFERENCES

[1] Pope, T.L., et al., *Imaging of the Musculoskeletal System*. 2nd Edition ed. Expert Radiology Series2008: Saunders. 2336.

[2] Hak, D.J. and T.L. Gautsch, *A review of radiographic lines and angles used in orthopedics.* Am J Orthop (Belle Mead NJ), 1995. 24(8): p. 590-601.

[3] Davies, E.R., *Chapter 5 - Edge Detection*, in *Computer and Machine Vision (Fourth Edition)*, E.R. Davies, Editor 2012, Academic Press: Boston. p. 111-148.

[4] Grafova, L., et al., *Study of edge detection task in dental panoramic radiographs.* Dentomaxillofac Radiol, 2013. 42(7): p. 20120391.

[5] Tariq, H. and S.M.A. Burney, *Contour Extraction of Femur and Tibia Condyles on Plain Anteroposterior (AP) Radiograph.* International Journal of Computer Applications, 2012. 52(15): p. 26-30.

[6] Aydin, A., T. Ibrikci, and I.D. Akcali, *A hybrid image processing system for X-ray images of an external fixator.* Comput Methods Biomech Biomed Engin, 2012. 15(7): p. 753-9.

[7] Zhang, J., et al., *Automatic Cobb measurement of scoliosis based on fuzzy Hough Transform with vertebral shape prior.* J Digit Imaging, 2009. 22(5): p. 463-72.

[8] Conrozier, T., et al., *Reproducibility and sensitivity to change of a new method of computer measurement of joint space width in hip osteoarthritis. Performance of three radiographic views obtained at a 3-year interval.* Osteoarthritis Cartilage, 2009. 17(7): p. 864-70.

[9] Qian, W., et al., *Tree-structured nonlinear filters in digital mammography.* IEEE Trans Med Imaging, 1994. 13(1): p. 25-36.

[10] Leung, C.K., et al., *Novel approach for anterior chamber angle analysis: anterior chamber angle detection with edge measurement and identification algorithm (ACADEMIA).* Arch Ophthalmol, 2006. 124(10): p. 1395-401.

[11] Zhang, L.P., B.Y. Yang, and C.H. Wang, *[The analysis and comparison of different edge detection algorithms in ultrasound B-scan images].* Zhongguo Yi Liao Qi Xie Za Zhi, 2006. 30(3): p. 170-2.

[12] 1Lloret, R.L., et al., *Classification of left ventricular thrombi by their history of systemic embolization using pattern recognition of two-dimensional echocardiograms.* Am Heart J, 1985. 110(4): p. 761-5.

[13] Pauwels, R., et al., *Automated implant segmentation in cone-beam CT using edge detection and particle counting.* Int J Comput Assist Radiol Surg, 2014. 9(4): p. 733-43.

[14] Shi, J., et al., *Treatment response assessment of breast masses on dynamic contrast-enhanced magnetic resonance scans using fuzzy c-means clustering and level set segmentation.* Med Phys, 2009. 36(11): p. 5052-63.

[15] Placidi, G., M. Alecci, and A. Sotgiu, *Post-processing noise removal algorithm for magnetic resonance imaging based on edge detection and wavelet analysis.* Phys Med Biol, 2003. 48(13): p. 1987-95.

[16] Lin, X., et al., *Spinal cord atrophy and disability in multiple sclerosis over four years: application of a reproducible automated technique in monitoring disease progression in a cohort of the interferon beta-1a (Rebif) treatment trial.* J Neurol Neurosurg Psychiatry, 2003. 74(8): p. 1090-4.

[17] Woodhead, H.J., et al., *Measurement of midfemoral shaft geometry: repeatability and accuracy using magnetic resonance imaging and dual-energy X-ray absorptiometry.* J Bone Miner Res, 2001. 16(12): p. 2251-9.

[18] Garcia, E.V., et al., *Totally automatic definition of renal regions of interest from 99mTc-MAG3 renograms: validation in patients with normal kidneys and in patients with suspected renal obstruction.* Nucl Med Commun, 2010. 31(5): p. 366-74.

[19] Drever, L.A., et al., *Comparison of three image segmentation techniques for target volume delineation in positron emission tomography.* J Appl Clin Med Phys, 2007. 8(2): p. 93-109.

[20] Wang, Z., et al., *Semiautomatic segmentation and quantification of calcified plaques in intracoronary optical coherence tomography images.* J Biomed Opt, 2010. 15(6): p. 061711.

[21] Rogowska, J. and M.E. Brezinski, *Image processing techniques for noise removal, enhancement and segmentation of cartilage OCT images.* Phys Med Biol, 2002. 47(4): p. 641-55.

[22] Wang, Z., et al., *A combining method for tumors detection from near-infrared breast imaging.* Conf Proc IEEE Eng Med Biol Soc, 2005. 6: p. 6508-11.

[23] Sivakamasundari, J., et al., *Fpga based hardware synthesis for automatic segmentation of retinal blood vessels in diabetic retinopathy images.* Biomed Sci Instrum, 2014. 50: p. 156-63.

[24] Jia, X., H. Huang, and R. Wang, *A novel edge detection in medical images by fusing of multi-model from different spatial structure clues.* Biomed Mater Eng, 2014. 24(1): p. 1289-98.

[25] Zhu, X., R.M. Rangayyan, and A.L. Ells, *Detection of the optic nerve head in fundus images of the retina using the Hough transform for circles.* J Digit Imaging, 2010. 23(3): p. 332-41.

[26] Zhu, X. and R.M. Rangayyan, *Detection of the optic disc in images of the retina using the Hough transform.* Conf Proc IEEE Eng Med Biol Soc, 2008. 2008: p. 3546-9.

[27] Chapman, N., et al., *Computer algorithms for the automated measurement of retinal arteriolar diameters.* Br J Ophthalmol, 2001. 85(1): p. 74-9.

[28] Romary, D., J.F. Lerallut, and G. Fontenier, *Application of image processing techniques to gamma-angiography.* Comput Biomed Res, 1985. 18(5): p. 488-95.

[29] Pijet, M., et al., *Fractal analysis of heart graft acute rejection microscopic images.* Transplant Proc, 2014. 46(8): p. 2864-6.

[30] Irianto, J., D.A. Lee, and M.M. Knight, *Quantification of chromatin condensation level by image processing.* Med Eng Phys, 2014. 36(3): p. 412-7.

[31] Ahammer, H. and T.T. DeVaney, *The influence of edge detection algorithms on the estimation of the fractal dimension of binary digital images.* Chaos, 2004. 14(1): p. 183-8.

[32] Konstantinidis, I., A. Santamaria-Pang, and I. Kakadiaris, *Frames-Based Denoising in 3D Confocal Microscopy Imaging.* Conf Proc IEEE Eng Med Biol Soc, 2005. 1: p. 290-3.

[33] Chang, M.H., et al., *Facial identification in very low-resolution images simulating prosthetic vision.* J Neural Eng, 2012. 9(4): p. 046012.

[34] Daponte, J.S. and M.D. Fox, *Enhancement of chest radiographs with gradient operators.* IEEE Trans Med Imaging, 1988. 7(2): p. 109-17.

[35] Potter, H.P., *The Obliquity of the Arm of the Female in Extension. The Relation of the Forearm with the Upper Arm in Flexion.* J Anat Physiol, 1895. 29(Pt 4): p. 488-91.

[36] Chapleau, J., et al., *Validity of goniometric elbow measurements: comparative study with a radiographic method.* Clin Orthop Relat Res, 2011. 469(11): p. 3134-40.

[37] Goldfarb, C.A., et al., *Elbow radiographic anatomy: measurement techniques and normative data.* J Shoulder Elbow Surg, 2012. 21(9): p. 1236-46.

[38] Morrey, B.F., *Morrey's The Elbow and Its Disorders*. 4th Edition ed2009: Saunders. 1232.

[39] Sobel, I. and G. Feldman, *A 3x3 Isotropic Gradient Operator for Image Processing*, 1968.

[40] Scharr, H., *Optimale Operatoren in der digitalen Bildverarbeitung*, 2000, Universitätsbibliothek.

[41] Prewitt, J.M.S., *Object Enhancement and Extraction*, in *Picture processing and Psychopictorics*, B.S. Lipkin and A. Rosenfeld, Editors. 1970, Academic Press: New York.

[42] Frei, W. and C. Chung-Ching, *Fast Boundary Detection: A Generalization and a New Algorithm.* Computers, IEEE Transactions on, 1977. C-26(10): p. 988-998.

[43] Kirsch, R.A., *Computer determination of the constituent structure of biological images.* Comput Biomed Res, 1971. 4(3): p. 315-28.

[44] Robinson, G.S., *Edge detection by compass gradient masks.* Computer Graphics and Image Processing, 1977. 6(5): p. 492-501.

[45] Klette, R., *Concise Computer Vision: An Introduction into Theory and Algorithms*. Undergraduate Topics in Computer Science2014: Springer.

[46] Marr, D. and E. Hildreth, *Theory of Edge Detection.* Proceedings of the Royal Society of London B: Biological Sciences, 1980. 207(1167): p. 187-217.

[47] Canny, J., *A Computational Approach to Edge Detection.* Pattern Analysis and Machine Intelligence, IEEE Transactions on, 1986. PAMI-8(6): p. 679-698.

[48] Duda, R.O. and P.E. Hart, *Use of the Hough transformation to detect lines and curves in pictures.* Commun. ACM, 1972. 15(1): p. 11-15.

[49] Paraskevas, G., et al., *Study of the carrying angle of the human elbow joint in full extension: a morphometric analysis.* Surg Radiol Anat, 2004. 26(1): p. 19-23.

[50] Koch, G.G., *Intraclass correlation coefficient*, in *Encyclopedia of Statistical Sciences*, S. Kotz and N.L. Johnson, Editors. 1982, John Wiley & Sons: New York. p. 213-217.

SOCIETY FOR SCIENCE AND EDUCATION
UNITED KINGDOM

JBEMi JOURNAL OF BIOMEDICAL
ENGINEERING AND MEDICAL IMAGING

ISSN: 2055-1266
VOLUME 2 ISSUE 6

Scaling up of Low Resolution Images using Super Resolution Techniques & Performing Intensity Correction for Medical Imaging

[1]Jithin Saji Isaac and [2]Ramesh Kulkarni
Department of Electronics & Telecommunication,
Vivekanand Education Society's Institute of Technology, Mumbai, India
[1]jithinsaji@gmail.com, [2]ramesh.kulkarni@ves.ac.in

ABSTRACT

The diagnosis of illness and certain underlying conditions can be effectively done by the use of Medical imaging. Higher resolution images are used to increase the diagnostic capabilities of the medical practitioner which leads to early and effective diagnosis of an ailment. Although a lot of advanced devices like Computerized Tomography (CT), Magnetic Resonance Imaging (MRI) etc. are currently available, the problem of Noise, Blur limits the overall ability of these devices to produce higher resolution images. A solution which can be proposed is the use of Super Resolution (SR) techniques which can be used for processing of such images. In this paper we make use of intensity correction of input medical images. The super resolution methods are done patch wise. The input images are divided into patches and dictionaries containing high and low resolution patches are obtained. Using the k-SVD algorithm for dictionary learning and OMP method for image super resolution reconstruction, the final high resolution image is obtained. The combination of intensity correction and super resolution leads to computationally and visually better results.

Keywords: Intensity inhomogeneity, Super Resolution, Dictionary learning, Sparse Representation, MRI

1 Introduction

It is desirable to have high resolution images for all our daily applications involving Image processing. With the help of a high resolution image, one can easily increase the accuracy with respect to finding a localized tumor or increase the visual excellence of watching a high definition video. The quality of the sensor generally decides the resolution of the image. But as the quality of the sensor increases, so does the cost of the acquisition device. Therefore a solution needs to be reached to overcome this hardware problem and replace it with a software system which will help to increase the resolution by keeping the hardware same. Such a software system is discussed in this paper and the name of the image processing technique used is called as Super Resolution Reconstruction.

In Image processing, the manipulation of digital images are undertaken. Image enhancing algorithms and software are incorporated to achieve this image enhancement. This high resolution image is used in various different engineering fields to zoom in on a particular region of interest. The raw data from the

DOI: 10.14738/jbemi.26.1732
Publication Date: 29th December 2015
URL: http://dx.doi.org/10.14738/jbemi. 26.1732

image acquisition sensors are processed further and are given to different image processing and enhancement algorithms to help remove the noise element blur components and increase the resolution of the image.

2 The Concept of Super Resolution

Super-resolution basically points out to the concept of combining low resolution and noisy images of a particular region and using these to obtain the higher resolution image.

The basic final aim of Super Resolution (SR) or Super Resolution Reconstruction (SRR) methods is to get the High Resolution (HR) image from one or more Low Resolution (LR) input images. Super Resolution (SR) is done either using the single image method wherein one low resolution image is used to obtain the higher resolution image using a dictionary method or is done using the multiple image method wherein multiple low resolution images are used to obtain the final high resolution image. [12]

The advantage of the single image based super resolution method is that we do not require many LR images. We use only one LR image and divide these into patches and work on one specific patch to obtain the higher resolution patch. The higher resolution patches are then used to find out the final high resolution images by combining all the higher resolution patches together.

We resample the high resolution image and produce the low resolution image. To this low resolution image we apply the Super Resolution algorithms which include the steps of Interpolation, noise and blur removal. When these steps are applied to the patch of the sampled LR image, we receive the HR patch. These HR patches later on form the HR image.

3 Super Resolution in Medical Images

Normal interpolation techniques are found for medical images consisting of intensity inhomogenity, blur and additive noise. Simple techniques like interpolation can only add extra pixels and improve the resolution but not do any task of removal of noise and intensity corrections. Such problems give rise to the new methods of Super Resolution wherein along with image resolution, the quality of the image with respect to noise and blur removal also needs to be considered.

Medical images are unique for the particular reason that they are taken in an environment which is much more challenging than the normal acquisition atmosphere. Therefore, the problems that accompany the medical images are very much of a higher magnitude when compared to normal images. General problems plaguing the medical images are given as below: [12]

- Low resolution
- Higher magnitude of Noise component
- Images with low contrast
- Imaging artefacts present in the image

4 Intensity Correction of Medical Images

Variations of illumination in the spatial domain and the imperfections of devices that capture the images can lead to many problems in Computer vision and Image processing techniques. The particular cases of Image segmentation may be difficult for images that have intensity inhomogenity due to different ranges of intensity that exist in an inhomogeneous image, thus making it difficult to identify images based on image intensity. Present day algorithms rely on the homogeneity of intensity and therefore images that are inhomogeneous are not applicable for practical purposes. Therefore, the idea of having level intensity homogeneity is very important. [10]

In this paper, a novel region-based method for image segmentation is used. This paper makes use of a local intensity clustering property and defines a local area clustering benchmark function for the intensities in a neighbourhood of each point. An accepted model of images with intensity inhomogeneities is used. This local area clustering benchmark is integrated over the intensity centre to define an energy functional. This energy function is then converted into a level set formulation. By means of bias field estimation and energy minimization, a level set evolution of intensity is achieved.

Bias correction and segmentation of MRI images can be extensively done with this method. This method is based on a model of an image which describes a combination of real world images which defines intensity inhomogenity to be a part of the image. By using the multiplicative model of intensity in homogeneity, we can observe a given as a combination of the original image as the first part, the second part that consists of intensity in homogeneity and the third part that consists of additive noise. The component that gives an observation of the pixels that have high intensity is referred to as a *bias field* (or *shading image*). This field we assume to be slowing varying. The additive noise is assumed to be zero-mean Gaussian noise. The image segmentation methods based on region selection typically relies on a specific region description of the intensities in each region to be segmented. But it becomes very difficult to give a descriptor for images which have intensity in homogeneities. As a result it gets very difficult to segment the inhomogeneous regions directly based on the different intensities of pixels involved in the image.

Here a variation level set criterion for image segmentation and image bias correction with intensity in homogeneity is used. [10] The twin tasks of Segmentation and bias field exploration is jointly done by reducing the proposed energy functional. This method is much better than piecewise smooth model used earlier. An experimental result on the MRI of a shoulder and MRI image of a brain gives superior results which can be seen in the below figure. Effective Image segmentation and bias estimation of the MRI image occurs and we observe an intensity homogenous image as under.

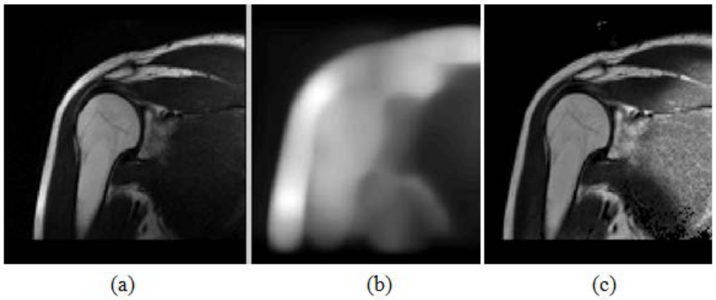

Figure. 1 Intensity Correction MRI image of shoulder: Original image of MRI of shoulder (a), bias field of the image (b) and Intensity corrected image (c)

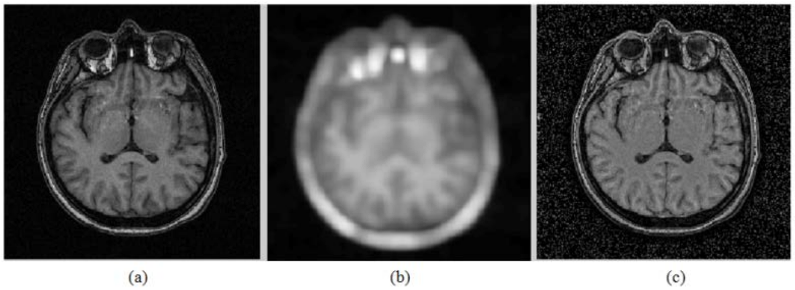

Figure. 2 Intensity Correction MRI image of shoulder: Original image of MRI of shoulder (a), bias field of the image (b) and Intensity corrected image (c)

5 Existing Technologies & Proposed Algorithm for Super Resolution of Medical Images

We can write the single image scale of problem as follows:

- Denote the original high-resolution image as y_h.
- Denote the blur and decimation operators as H and S.
- H is a low-pass filtering which we perform on the image and S is the decimation of the image which we perform by an integer factor s.
- z_l is the Noisy and low-resolution image obtained from the version of the original image y_h

Therefore, we denote the low resolution image obtained as z_l.

$$z_l = SHy_h + v,$$

Where v is an Additive i.i.d. White Gaussian noise.

Given $\mathbf{z}_l$, the problem is to find a new image y such that $y \approx y_h$. The maximum-likelihood estimation is obtained by the minimization of $||\mathbf{SHy} - \mathbf{z}_l||_2$ due to the inherent Gaussian nature of the Gaussian noise component v.

The Sparse-Land model is used for the scale-up problem in this paper as was introduced in [7], [8] & [9]. The basic assumption is that each of the patches from the images selected can be represented as a linear combination of patches from the dictionary i.e. each patch is obtained by multiplying the dictionary by a sparse vector of coefficients.

Often there is a problem in the resolutions of z_l and y_h. To avoid this issue, z_l is scaled up by Bicubic interpolation to realize into the same size as y_h. Let us now call this scaled up image as y_l instead of z_l. Let Q be the operator by which we work on z_l. Therefore,

$$y_l=Q.z_{l.=}Q(SHy_h+v)= (QSHy_h+Qv)=X.\ y_h + v$$

By using this algorithm, we can operate on patches extracted from $\mathbf{y}_l$ and therefore aiming to estimate the corresponding patch from $\mathbf{y}_h$.

The algorithm of the proposed method can be segregated into two main sub phases given below:

5.1 Construction of the Training set and Dictionary Training

The first task to construct the training set is to collect the High resolution images y_h. We then blur and down scale these images by a factor of s. Thus the low resolution images z_l are formed. These z_l are then scaled up using the Q interpolation factor to y_l. Thus, $y_l = X.\ y_h + v$

Next, pairs of matching patches are extracted which will eventually form the training database P= {p_h, pl}. All these patch-pairs individually undergo a pre-processing stage that removes the low frequencies from p_h and extracts features from p_l. [2][3]

The very important step of the dictionary learning stage is done using the K-SVD dictionary training proposed in [4]. This algorithm is applied to the patches and we get the LR dictionary D_l. The residual component of this training procedure is the sparse representation coefficients vectors $\{q^k\}$ that correspond to the training patches $\{p_l\}$. To represent the low resolution patches sparsely, the dictionary D_l is trained.

Now that the low resolution dictionary is constructed, we need to construct the high resolution dictionary D_h. Once we get D_h, then we can get the HR patch p_h by approximating it as $p_h \approx D_h q^k$.

5.2 Super Resolution Reconstruction of Low resolution image into High Resolution Image

- First the low resolution image z_l is scaled to y_l using Bicubic interpolation and bought to same size as y_h.
- The image y_l is then pre-processed using High pass filters and then patches are extracted from the result of this filtering giving us p_l.
- The OMP algorithm [11] is applied to p_l by allocating L atoms to the representation and the sparse representation vector q^k is obtained.
- q^k is then multiplied with the high resolution dictionary D_h and the approximated HR patch p_h is obtained.
- The final high resolved output y_h is constructed from p_h by combining all these high resolution patched together.

5.3 Using Single Image as Dictionary set

If during the training process of the dictionary, there are no external set of images, then the algorithm is trained to use a single image. This single image will be the same Low resolution image that we input to the system i.e. image z_l. This image z_l is then used as the supposed high resolution image and the scaled down version of this image is called as z_{ls}. The images z_l and z_{ls} are then subjected to the dictionary training phase. These trained dictionaries are then used to reconstruct the high resolution image back i.e. to get back z_l and ultimately we can scale that up and get y_h.

The following block diagram in figure no. 3 gives a basic pictorial idea of the entire flow of the proposed algorithm of the project.

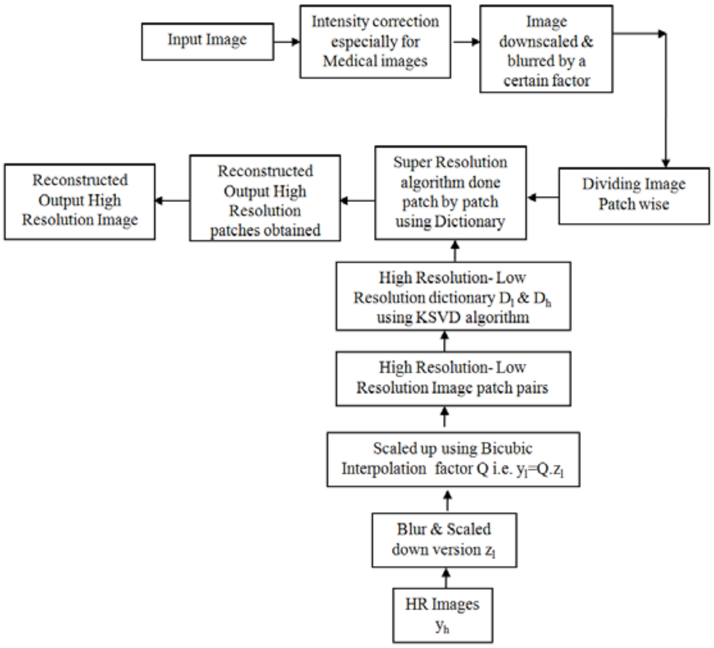

Figure. 3 Basic Block Diagram of the Proposed Method.

6 Outputs

The following outputs were achieved for the flow chart of the proposed algorithm shown above. The input to the sparse representation method and proposed method is the resized down scaled input image, in this case, it is the MRI image of the shoulder.

The fig. 4 shows the resized image of the original image. This image is given to the Bicubic, Sparse and the proposed Image upscale algorithm. The outputs obtained and the corresponding PSNR and SSIM are mentioned below in Table No I.

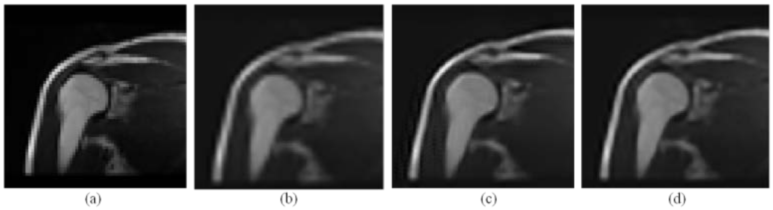
(a) (b) (c) (d)

Figure. 4 Super Resolution of MRI image of shoulder: Input Resized image (a), Output of Bicubic Interpolation (b), Output of Sparse Representation (c) and Output of Proposed Image scale up algorithm (d)

Table 1: comparing the PSNR & SSIM values for Bicubic interpolation, sparse representation and proposed image scale up algorithm

TECHNIQUE	PSNR (dB)
Bicubic Interpolation	27.9
Sparse representation (ScSR)	29.7
Proposed Image scale up algorithm	30.5

Figure No. 5 shows the output of the three methods when Intensity correction is performed on the input image prior to it being downscaled and given to the super resolution stages.

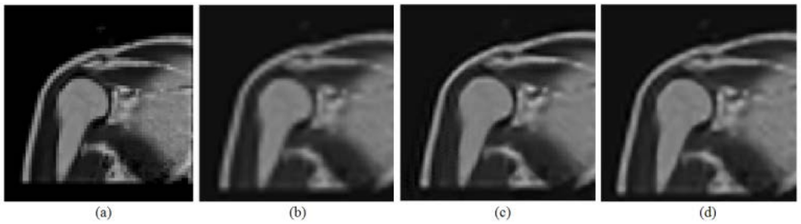

Figure. 5 Super Resolution of MRI image of shoulder: Input resized scaled down image with Intensity correction performed (a), Output of Bicubic Interpolation (b), Output of Sparse Representation (c) and Output of Proposed Image scale up algorithm (d)

Now, before the intensity correction is done, the image is subjected with Gaussian Noise to replicate the real world effect which is bound to occur while capturing medical images. The PSNR & SSIM of the images subjected to Gaussian Noise & Intensity Correction are shown Table II and the corresponding images capture in Figure No. 6.

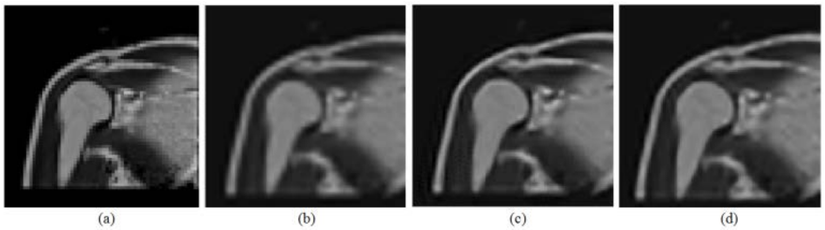

Figure 6 Effect of adding Gaussian Noise to an Image and then image correcting and super resolving it

Table2: comparing the PSNR & SSIM values for the different methods when the image is subjected to Gaussian noise

TECHNIQUE	PSNR (dB)
Bicubic Interpolation	19.9
Sparse representation (ScSR)	20.2
Image Scale up algorithm	20.3

The intensity corrected & Gaussian noise added image in now given to an averaging filter to check for certain changes in the output. Therefore, before the super resolution stage, the resized and intensity corrected image is given to an averaging filter. The basic functional block diagram of the proposed system is shown in Figure No. 7. The corresponding outputs are shown in Figure no. 8 and PSNR and SSIM values are mentioned in Table No. III.

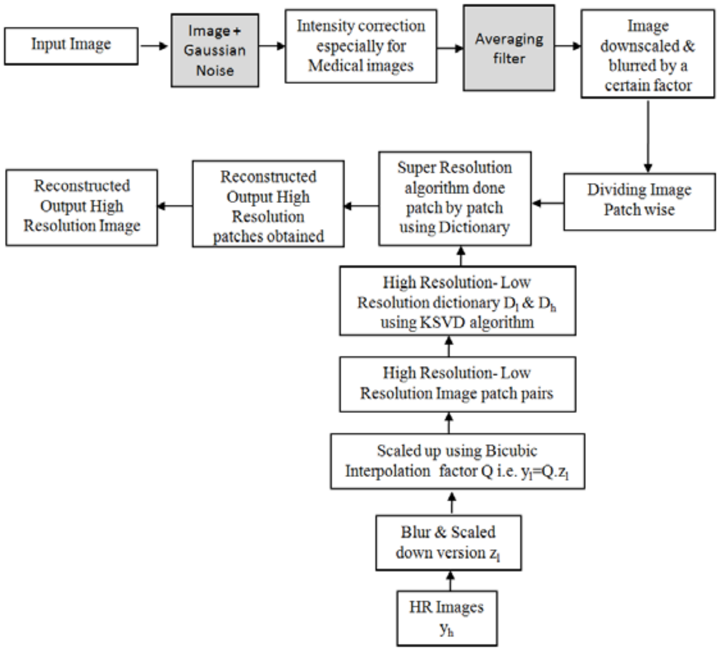

Figure. 7 Basic Block Diagram of the Proposed Method for an image added with Gaussian noise and then passed through an Averaging filter just before the super resolution stage

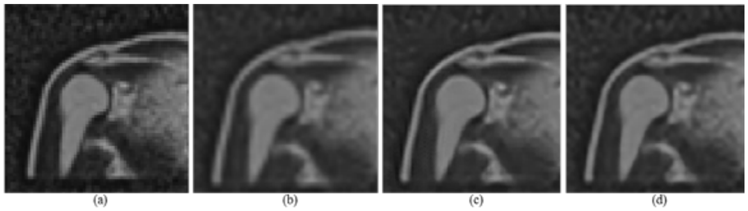
(a) (b) (c) (d)

Figure. 8 Effect of using Averaging filter just before the super resolution stage for partially removing the effects of the Gaussian Noise Added to the image

Table 3: Comparing the PSNR & SSIM values when the image subjected to Gaussian Noise is passed through an averaging filter before giving it to the Super Resolution Methods

TECHNIQUE	PSNR (dB)
Bicubic Interpolation	22.9
Sparse representation (ScSR)	24.4
Image Scale up algorithm	26.2

7 Conclusion

In this paper, the basic work of super resolution is carried out with the help of image patches. Low resolution image patches are converted into high resolution image patches. The detailed work of Yang et. al. in [2] & [3] forms the cornerstone of all research into the subject of sparse representation. The input image is first intensity corrected before applying to the super resolution phase. This intensity correction forms the special part of this paper. Intensity correction leads to better medical images which are visually and mathematically far better than other images which have intensity inhomogenity. Once the image intensity is performed, the image is given to the super resolution process wherein the image is divided into number of patches. Prior to this, a dictionary consisting of low resolution and high resolution patches is separately trained. Based on this dictionary and the k-SVD algorithm, the dictionary is properly trained. By using the OMP algorithm, the super resolution reconstruction occurs. The high resolution patches are formed which then combine to give us the final high resolution image.

Obtaining a High resolution image is of paramount importance for medical images. A high resolution medical image is necessary for better diagnosis of the ailment. Therefore the concept of Super Resolution is of great value for overcoming the problem of low resolution.

The future scope in the development of SR techniques is tremendous. One can develop newer and better algorithms for the continuous enhancement of the image parameters like PSNR and SSIM, thereby making this field challenging and evolving.

REFERENCES

[1] S. Chaudhari, Department of Electrical Engineering, Indian Institute of Technology – Bombay, Mumbai, India 400 076, *“Super Resolution Imaging”. New York, Boston, Dordrecht, London, Moscow, Kluwer Academic Publishers.*

[2] J. Yang, J. Wright, T. Huang, Y Ma, “*Image super-resolution as sparse representation of raw image patches”, IEEE Computer Vision and Pattern Recognition (CVPR) (June 2008)*

[3] J. Yang, J. Wright, T. Huang, Y Ma, “*Image Super-Resolution via Sparse Representation IEEE Transactions on Image Processing”, IEEE Transactions On Image Processing, Vol. 19, No. 11, November 2010*

[4] T. Peleg, M. Elad, “*A Statistical Prediction Model Based on Sparse Representations for Single Image Super-Resolution”, IEEE Transactions on Image Processing, Vol. 23, No. 6, June 2014*

[5] M. Aharon, M. Elad, A.M. Bruckstein, *“The K-SVD: An algorithm for designing of over complete dictionaries for sparse representation”, IEEE Transactions on Signal Processing 54(11), 4311–4322 (2006)*

[6] Li, R. Huang, Z. Ding, J. C. Gatenby, D. N. Metaxas, J. C. Gore, “*A Level Set Method for Image Segmentation in the Presence of Intensity Inhomogeneities With Application to MRI*”, *IEEE Transactions On Image Processing, Vol. 20, No. 7, July 2011*

[7] Trinh, M. Luong, F. Dibos, J.M. Rocchisani, C.D. Pham and T.Q. Nguyen, *“Novel Example-Based Method for Super-Resolution and Denoising of Medical Images”, IEEE Transactions on Image processing, Vol. 23, No. 4, April 2014*

[8] M. Elad, M. Aharon,*“Image denoising via learned dictionaries and sparse representation”, International Conference on Computer Vision and Pattern Recognition, New York, June 17-22 (2006)*

[9] M. Elad, M. Aharon,*“Image denoising via sparse and redundant representations over learned dictionaries”, IEEE Transactions on Image Processing 15(12), 3736–3745(2006).*

[10] M. Bruckstein, D.L. Donoho, M. Elad, "*From Sparse Solutions of Systems of Equations to Sparse Modelling of Signals and Images", SIAM Review 51(1), 34–81(2009)*

[11] H. Okuhata, R. Imai, M. Ise, R. Y. Omaki1, H. Nakamura, S. Hara and I. Shirakawa, *"Implementation of Dynamic-Range Enhancement and Super-Resolution Algorithms for Medical Image Processing" in 2014 IEEE International Conference on Consumer Electronics (ICCE)*

[12] J. S. Isaac, R. Kulkarni, "Super Resolution Techniques for Medical Image Processing", International Conference on Technologies for Sustainable Development (ICTSD), 4-6 February, 2015